THE INFLUENCE OF ANISOTROPY AND HETEROGENEITY ON THE MECHANICS OF MILD TRAUMATIC BRAIN INJURY

by

Fatma Abdullatif Madouh

A dissertation submitted to The Johns Hopkins University in conformity with the requirements for the degree of Doctor of Philosophy.

Baltimore, Maryland

November, 2018

Abstract

Traumatic Brain Injury (TBI) has been intensively studied for several decades. Much attention has been directed towards mild TBI (mTBI) due to the increased rates of occurrence compared to other types of TBI especially in military and sports. There are two general approaches to study mTBI: computational and experimental, and each approach complements the other. The experimental direction provides observations of injury as well as the necessary material behavior for the computational models, while the computational models can simulate injury-inducing events which cannot be performed experimentally (in humans).

In this work, we use the computational approach to examine how heterogeneities in the human brain affect the mechanical response and/or the deformation of the brain tissue in mTBI. We focus on white matter, the vasculature network and gray matter. Constitutive models for white matter have evolved from linear elastic to isotropic hyperelastic and finally to transversely isotropic hyperelastic material. Although experimental evidence points to anisotropy of white matter in both tension and shear, prior models have accounted for anisotropy in tension but not in shear.

ABSTRACT

We investigate the effects of shear anisotropy in mTBI by comparing two models: one that captures anisotropy in both tension and shear to another model that captures only tension anisotropy. With respect to vasculature, there is very limited literature that studies the effects of the vasculature on the mechanics of mTBI. In this work, we build two models (with and without vasculature) to investigate vasculature effects on the likelihood of injury. Finally, we investigate the effects of gray matter heterogeneity by building two models, one with homogeneous gray matter and another with heterogeneous gray matter. To our knowledge, the effect of gray matter heterogeneity has not been investigated in computational models although recent experiments provide evidence of heterogeneity in gray matter. Since the most commonly used injury criteria in recent literature are strain-based, we compare the strains predicted by the two models to address the main questions we raised about heterogeneity (how white matter shear anisotropy, vasculature network and gray matter heterogeneity affect the mechanics of mTBI). Our results show that two heterogeneity sources, white matter shear anisotropy and the vasculature, significantly influence the brain deformation and subsequently the predicted injury.

Thesis advisor and primary reader: Prof. K. T. Ramesh

Secondary Readers: Prof. Philip Bayly and Prof. Thao (Vicky) Nguyen

Acknowledgments

I would like to take this opportunity to thank everyone who stood by me and supported me throughout my graduate studies in Johns Hopkins University. This work would not be possible without the help and support of many people.

I would like to start with my advisor, Prof. K.T. Ramesh who helped me build and expand my research skills. He encouraged me throughout the PhD journey and pressed me to think in new ways to make me a better researcher. I was always amazed and inspired about his diverse knowledge and how he find links between all the different research fields in his lab. I would also like to thank my thesis readers, Prof. Philip Bayly and Prof. Thao (Vicky) Nguyen for taking the time to read my work and provide me feedback. I would like to thank my Master's advisor, Prof. Sean Sun who opened the doors for me to join the Johns Hopkins University and start my graduate studies. His kindness and directions helped through my Master's studies, so thank you so much.

To all the collaborators: Prof. Jerry Prince, Jeffrey Glaister, Prof. Dzung Pham and Dr. Andrew Knutsen, thank you for our fruitful technical discussions. I am

so grateful for Jeffrey Glaister and Dr. Andrew Knutsen for working so hard to provide me data that enhanced my work and increased the impact of this study on the research field of mTBI. Much of this work would not have been possible without this collaboration.

I am also grateful to meet and work with all the students and post-doctoral fellows in the Ramesh lab group and other mechanical and civil engineering departments (current and past). A big thanks to the biomechanics post-doctoral fellows that helped me learn the secrets to better computational skills, Dr. Shailesh Ganpule and Dr. Yuan-Chiao Lu. Thank you to Dr. Charles El-Mir who was very supportive and helped me to learn a lot about parallel computing and data processing. To my current lab-mates Vignesh Kannan, Amy Dagro, Debjoy Mallick, Meng Zhao, Alex Sun, Kimberly Andes, Jason Parker, Connor Bradfield, Sakshi Braroo and Gary Simpson, thank you for the encouragement and support and I am looking forward to see your success.

To my sponsors, Kuwait University, thank you for making this journey happen and for encouraging me and my fellow scholars to pursue the PhD degree. Special thanks to Prof. Najem Al-Najem, Prof. Waleed Chakroun, Dr. Abdulazim Falah, Dr. Majed Majeed, Dr. Nawwaf Al-Juwaihel and Mr. Alhassan Abdulmonem Mansour. Their input to support me as a scholar and their continuous support and encouragement throughout my graduate studies made this journey a lot more easier than it would have been otherwise.

ACKNOWLEDGMENTS

Lastly, but most importantly, my lovely family. A BIG thank you to: my father Abdullatif, my mum Eqbal, my brothers Khaled, Saleh and Yousef and my gorgeous sister Dr. Maryam. You all supported me before I started and during my graduate studies. I am pretty sure your support will continue, so thank you again and thank you in advance. You keep me motivated and you lifted me up when I needed support. To my husband Mishary, who joined me in the last two years of this journey, thank you for standing by me and understanding the difficulties of the long-distance relationship we had to live with. To my uncles, my aunt, my cousins and my friends back home thank you so much for believing in me and supporting me. Your input definitely made a big difference.

Thank you all from the bottom of my heart.

Dedication

To my amazing, loving and supporting family

Contents

Abstract ii

Acknowledgments iv

List of Tables xiv

List of Figures xvi

1 Introduction 1

1.1 Traumatic Brain Injury: Motivation 1

1.2 Anatomy of the Head 3

1.3 Diagnosis of mTBI 4

1.4 Computational Modeling of mTBI 7

1.4.1 Brain Tissue Characterization 7

1.4.1.1 Variations Between Species 8

1.4.1.2 Influence of Age 11

1.4.1.3 Influence of Post-Mortem Time 11

1.4.1.4 Strain Rate Effects 12
1.4.1.5 Temperature Effect 15
1.4.2 Constitutive Modeling 15
1.4.2.1 Brain Tissue Constitutive Modeling 15
1.4.3 Injury Criteria 18
1.4.3.1 Macroscale (Head) Based Injury Criteria 18
1.4.3.2 Microscale (Tissue) Based Injury Criteria 21
1.4.4 Cellular Level Injury Criteria 23
1.5 Overview of the Thesis 25

2 Shear anisotropy in mTBI: A white matter constitutive model 26

2.1 Introduction 26
2.2 Materials and Methods 27
2.2.1 Constitutive Model 28
2.2.2 Material Properties 33
2.2.3 Finite Element Head Model 37
2.2.4 Validation of the Head Model for Non-Injurious Loading . . . 40
2.2.5 Injury Criteria 45
2.2.6 An injurious Event 46
2.3 Results 46
2.4 Discussion 49
2.5 Summary of This Chapter 53

3 The Influence of the Arterial network on brain biomechanics under inertial loading **55**

3.1 Introduction . . . 55

3.2 Problem Statement . . . 58

3.3 Inertial Loading Test Case . . . 59

3.4 Building the 3D head models . . . 60

3.4.1 MRI segmentation . . . 61

3.4.2 TOF segmentation . . . 62

3.4.3 MPM implementation . . . 63

3.4.4 Material Models & Properties . . . 68

3.5 Validation . . . 74

3.6 Impact of the Arterial Network . . . 78

3.6.1 Isotropic Limit . . . 78

3.6.2 Results . . . 80

3.6.2.1 Average Strain . . . 81

3.6.2.2 Maximum Strain . . . 82

3.6.2.3 Strain Distribution . . . 84

3.6.2.4 Strain w.r.t. Nearest Blood Vessel . . . 86

3.7 Discussion . . . 89

3.8 Summary of This Chapter . . . 94

4 The Effects of Vasculature on Mild TBI **96**

4.1 Introduction . . . 96
4.2 Methods . . . 97
4.2.1 The Three Dimensional Head Model . . . 97
4.2.2 Material Point Method Implementation . . . 98
4.2.3 Injurious Loading and Injury Criterion . . . 98
4.3 Results . . . 102
4.3.1 Vasculature effects in mTBI . . . 103
4.3.1.1 Injury Predictions: Extent of Injury . . . 103
4.3.1.2 Injury Predictions: Locations of Injury . . . 104
4.3.2 Effect of loading direction on injury predictions . . . 105
4.3.2.1 Maximum Strains . . . 105
4.3.2.2 Injury Predictions . . . 111
4.4 Discussion . . . 113
4.5 Summary of This Chapter . . . 120

5 Gray Matter Heterogeneity in mTBI **122**

5.1 Introduction . . . 122
5.2 Methods . . . 123
5.2.1 Gray Matter Substructures . . . 123
5.2.1.1 Material Models & Properties . . . 125
5.2.2 MPM Implementation . . . 128
5.2.3 Loading conditions . . . 128

5.3 Results 128
5.4 Discussion 132
5.5 Summary & Conclusions 134

6 Summary & Future Directions **135**

6.1 Concluding Remarks 135
6.1.1 Summary of brain heterogeneity effects in mTBI 137
6.2 Future Directions 140

A MPM Implementation Using The Uintah Computational Framework **144**

A.1 Building Uintah 145
A.2 Uintah Simulations: Basics 146
A.3 Post-processing Uintah Output Using VisIt and MATLAB 148
A.3.1 How to Plot the Structure 149
A.3.2 How to Write Expressions 150
A.3.3 How to Export Database 152
A.3.4 MATLAB Post-processing 154

B A Biphasic Theoretical Framework to Couple Brain Deformation with Cerebral Blood Flow in mTBI **159**

B.1 Derivation of the Constitutive Equations: The Biphasic Theory . . . 160
B.2 Application Challenges 164

C Data Archives **166**

Bibliography **168**

Vita **211**

List of Tables

1.1 Classification of closed-head injury. 2
1.2 A summary of strain-rate studies in the literature. 13
1.3 A summary of the constitutive models used for the brain tissue in mTBI literature. 17
1.4 Injury thresholds developed from either accident reconstrcution or animal studies published in the literature. 22
1.5 Cellular level injury thresholds derived experimentally in-vivo and in-vitro. 24

2.1 Values for the material parameters in the shear anisotropic model (equation 2.6) determined by fitting the results of Velrdi et al.Velardi et al. [1] and Jin et al.Jin et al. [2], and in the HGO model (equation 2.9) used by Wright et al.Wright et al. [3] 36
2.2 Material models used for the head structures other than white matter. 39
2.3 Values for the material parameters used for the head structures other than white matter. 40
2.4 Agreement measures used in the validation of our model. 44
2.5 The degree of agreement between the shear anisotropic model and the HJF experiment at four specific times, using the measures described in Table 2.4. 45

3.1 A comparison in problem setup and solution procedures between Finite Element Method (FEM) and Material Point Method (MPM). 65
3.2 Statistical agreement results between maximum principal strains of the 3D head model with vasculature and the experimental strains of Knutsen et al. [4] 79
3.3 Material Models used for the white and gray matters. 80
3.4 Chi-squared test results of the comparison between the two models under non-injurious inertial loading. 86

LIST OF TABLES

4.1 Injury predictions using two different injury measures for the simulations with and without blood vessels. 104
4.2 Extracted White matter tracts using the TRACULA method. 107
4.3 Maximum Strains experienced by white matter substructures. 110
4.4 Injured volume fractions for each white matter structure. 112

5.1 Prony series shear modulus properties assigned to gray matter substructures which are adapted from published experimetnal studies. . . 127

List of Figures

1.1 A bottom view of the brain showing major arteries and the circle of Willis (inside the rectangle) (Huettel et al. [5]). 5
1.2 A wide range of the brain's complex shear modulus from experimental studies, summarized by Meaney et al. [6]. 8
1.3 A comparative plot showing shear modulus response of brain samples from multiple species (Chatelin et al. [7]). We conclude from this scattering that there is no defined difference between the brain properties of humans and other animals in literature. 10
1.4 Summary of average stress at 50% strain of gray and white matters at varying strain rates from the study by Jin et al. [2]. **p<0.001. (a) Tension, (b) Compression, and (c) Shear test results. 14
1.5 The Wayne State Tolerance Curve which is used as a brain injury predictor (Gurdjian et al. [8], Greenwald et al. [9]) 19

2.1 Schematic showing the deformation of the anisotropic white matter. Assuming a single family of fibers in the constitutive model, a) the fiber direction changes from $\mathbf{a_0}$ to $\mathbf{a}$ after the application of the deformation gradient $\mathbf{F}$. b) Schematic showing an example of the three experiments that are needed in order to obtain the material parameters for the shear anisotropic constitutive model. 29
2.2 Determination of the material parameters for the shear anisotropic model (equation 2.6). The first Piola-Kirchhoff (PK) stress is plotted vs. the corresponding stretch (top and middle), and vs. the shear strain (bottom). The experimental measurements are taken from the work of Velardi et al.Velardi et al. [1] and Jin et al.Jin et al. [2]The fits allow us to obtain C_1 (top), C_2 (middle) and C_3 (bottom). Note: the relationship between the 1^{st} PK stress (P) and the Cauchy stress $\boldsymbol{\sigma}$ (equation 2.8) is $J\boldsymbol{\sigma} = \mathbf{F}\mathbf{P}^T$. 35

2.3 The 2D finite element head models from the three representative planes: Axial (left), Coronal (middle) and Sagittal (right). The models include multiple brain structures that have been segmented from the MRI data. 37
2.4 Comparison of the measured (HJF) and the computed (shear anisotropic model) shear strain distributions for the axial cross-section for every 18 ms beginning 9 ms after loading. Note that the simulation resolution is higher than the experimental resolution, leading to the appearance of more detailed strain distributions in the model results. The HJF results are derived from the Knutsen et al. [4] paper. 42
2.5 Simulation results for: a) The shear anisotropy of the injury case are presented in terms of the axonal strain (damage) distributions in the three cross-sections. Note: If axonal strain reached or exceeded the threshold of 18%, the element is labeled "damaged" for the remainder of the simulation. b) The comparison of the injury predictions of the previous HGO model and the current shear anisotropic model. Damaged regions ($\varepsilon_{Axon} \geq 18\%$) in each slice shown in red for the axial (left), coronal (middle) and sagittal (right) orientations. 48
2.6 Time evolution of the total damage predicted by the HGO and shear anisotropic models. Solid lines represent the shear anisotropic model and dashed lines represent the HGO model. Note the higher amounts of damage predicted by the shear anisotropic model. 49
2.7 Comparisons of the evolution of the radial-circumferential shear strains predicted by the shear anisotropic model (top row) and the HGO model (bottom row) in the (a) Axial (b) Coronal and (c) Sagittal orientations. Note the shear strain concentrations in the brainstem predicted by the shear anisotropic model in the coronal and sagittal cases. 50
2.8 A comparison of the strains at the gray and white matter boundary for three mesh resolutions: high, mid and low (max. element size is 1, 2 and 5 mm respectively). The contours represents axonal strain, high axonal strains are represented by red (strains get higher as colors turn from orange to red). Clearly, high strains (and consequently damage) at the white and gray matter boundaries are to some degree due to mesh resolution. 51

3.1 Position (left) and angular acceleration (right) histories for a healthy subject in-vivo experiment from Chan et al. [10]. 60

3.2 Left: A cut through the model with blood vessels showing all segmented structures (Skull, CSF, ventricles, falx, tentorium, white matter, gray matter, brainstem and blood vessels). Right: The whole model making all structures transparent except the blood vessels. For MPM implementation, a fixed background grid is overlaid on the model with cubic cell size of 3.2mm and two material points in each direction (material point spacing = 1.6mm). Note: The vasculature network is mainly connected with some isolated islands of arterial vessels. 68
3.3 The stress-strain behavior of fresh human cerebral arteries and veins. A comprehensive experimental study by Monson et al. [11]. 70
3.4 The fitting result for the blood vessels in our head model to an artery sample behavior from Monson et al. [11]. The Mooney-Rivlin parameters are μ_1= 25 MPa and μ_2= 20 MPa. 71
3.5 Loading conditions used for the validation of our 3D head model from Knutsen et al. [4] experiment. An axial rotation of the head (a) is produced by a counter-weight fixed to the special MRI device which induces a non-injurious angular acceleration (b). 75
3.6 a) The co-registered model used for the validation with in-vivo brain deformation experiment of Knutsen et al. [4] (The circle highlights the cerebellum which is not fully accounted for). b) A side view (sagittal) of the model with the experimental tagged MRI slices in red. 77
3.7 a) Average LPS and b) E_{rt} strains plotted at every 5ms for the simulations with and without blood vessels. Overall average strains are higher in the simulation without blood vessels due to lower overall stiffness. . 82
3.8 a) Maximum LPS (left) and b) E_{rt} strains plotted at every 5ms for the simulations with and without blood vessels. Differences between the two simulations exist, with higher overall maxima in the simulations without blood vessels due to lower overall stiffness. 83
3.9 Maximum LPS locations are shown for the simulation with blood vessels (red squares) and the simulation without blood vessels (blue circles) by looking through two planes a) coronal and b) sagittal. It is very clear that the locations of temporal maxima differ from one simulation to another. For example, in this time instance, the simulation with blood vessel predicted maximum strains in the subject's left side (red squares to the right of the coronal view (a)). 85

3.10 a) LPS and b) E_{rt} strain distributions at time 40ms for the simulations with and without blood vessels. The frequency values indicate total number of material points with the same strain value. Although visual differences are clear, we also run chi-squared statistical test and statistically confirmed the difference (p-value$<$0.00001). Also, the wider tails of the distributions from the simulation without blood vessels are consistent with the observation of higher overall average and maximum strains in the previous subsections. 87
3.11 A schematic showing how the distance from the nearest blood vessel is calculated. The red point represents a voxel belonging to the blood vessels and the yellow points represent brain tissue voxels. First, the distance (d), based on the number of voxels between the vasculature voxel and the brain tissue, is assigned to each point in the original volume of the segmentation. The millimeter resolutions of the image volume is multiplied by the number of voxels to obtain distance in millimeters. Then the results are mapped using nearest neighbor search method to our 3D head model. 88
3.12 The relation between strain values and distance from blood nearest blood vessel at 40 ms for the simulations (a) with and (b) without blood vessels (By virtually adding the vasculature structure in the simulation without blood vessels). The distance is measured in the reference configuration so each point can only change strain magnitude with time. High strains in both simulations forms two peaks (highlighted with red curves). While the second peak (between 15 to 20 mm away from nearest blood vessel) did not change location, the first peak shifted it's center from 10 mm to 5 mm and is narrower in the simulation with blood vessels. This indicates that introducing the vasculature network in the model caused a shift in the first peak due to the high stiffness of the vasculature compared to the brain tissue. 90
3.13 A brain slice showing axonal injury in a human subject adapted from Ryu et al. [12]. The dark spots represents damaged axons, which form clusters around the arterioles. (b) and (c) are enlargements of the blocked areas in (a) and (b), respectively. The subject had blast exposure 1 year before death and a concussion from assault 2 months prior to death. 93

4.1 a) A schematic showing the coordinate system of the head used in our study and the corresponding rotations. b) The angular accelerations about the x-axis (coronal rotation), y-axis (sagittal rotation) and z-axis (axial acceleration) of an NHL accident reproduced from Wright et al. [3]. c) The angular position profile calculated by integrating the accelerations of the NHL accident twice. 100

4.2 a) The angular acceleration and b) The angular position profiles Chosen for The two studies in this chapter. In the First study (c) injury predictions will be compared between two models, one with and one without vasculature. Then, the model with vasculature will be used for the second study (d) to examine the effect of the loading direction on injury predictions. 101
4.3 Location of damaged material points for the largest principal strain criterion (showing (a) front and (b)side views) and the axonal strain criterion (showing (c) front and (d)side views) for both models with (red squares) and without (blue circles) vasculature (Black points represent the blood vessels). Significant differences exist between the two models since there are many isolated locations predicted by one of the models but not the other. We should also note that locations of damage differ from one injury criterion to another. 106
4.4 Largest principal strain map for a coronal slice of the coronal rotation simulation. Locations of high (dark blue) LPS are concentrated at the white matter "gyri", the lower surface of the cerebral cortex gyri and into the depths of the sulci. These locations agree to some degree with observations in the literature. 109
4.5 Maximum axonal strain (ϵ_{Axon}) for each tract in Table 4.2 experienced in each loading direction scenario. 111
4.6 Maximum axonal strain (ϵ_{Axon}) for each tract in Table 4.2 experienced in each loading direction scenario. 113
4.7 A frontal view of the white matter substructures cross-sections showing the axial and coronal rotations. The widest cross-section of the cerebrum is perpendicular to the axial axis of rotation while the widest cross-sections of the cerebellum and the brainstem are perpendicular to the coronal axis of rotation. By rotating the wider planes, more shear deformation (and consequnetly higher strains) is allowed in the structure which explains the higher vulnerability to injury in the cerebrum for axial loading and in the cerebellum and brainstem for coronal loadings. 116
4.8 A comparison of the loading direction compared to the geometry of the brainstem between (a) human and (b) pig brains (The dark pink color represents the brainstem). The axial rotation of the pig head is perpendicular to the long axis of the brainstem which is similar to the coronal rotation in human brain. The opposite, coronal rotation of the pig head is anatomically equivalent to axial rotations of the human head, is also true. Pig brain illustration (b) is adapted from Smith et al. [13]. 119

5.1 (a) Front and (b) top views showing the four segmented gray matter substructures: caudate (green), hippocampus (sand), putamen (purple) and thalamus (red). 124
5.2 Maximum largest principal strain history for the (a) caudate (b) hippocampus (c) putamen and (d) thalamus extracted at every 5 ms for the two simulations (homogeneous vs heterogeneous gray matter). Clearly, there are no significant differences between the two models. . 130
5.3 Maximum shear strain history for the (a) caudate (b) hippocampus (c) putamen and (d) thalamus extracted at every 5 ms for the two simulations (homogeneous vs heterogeneous gray matter). Results of the two models are identical. 131
5.4 Injury locations in the caudate (red squares) along with injury in cerebral white matter (green triangles) using largest principal strain as a predictor shown in two views: (a) front and (b) top. Notice that injury in the caudate neighbors white matter injury. The light green clouds represent the caudate material points. 132

6.1 An ellustration for the incorporated length scales in our model. The red box encloses the actual anatomy resolved in the model, while the green box enclosed the fiber bundles which are incorporated in the material model and the injury criterion. Organ schematic is adapted from Huettel et al. [5]. 138

Chapter 1

Introduction

1.1 Traumatic Brain Injury: Motivation

Sudden loading of the head can cause injury defined as Traumatic Brain Injury (TBI). Such loading can result from falls, auto accidents, blasts and contact sports like boxing, rugby, and American football. Based on the condition of the injured head, brain injury is typically categorized as either penetrating injury or closed-head injury. As the name suggests, penetrating injury requires the penetration of an object (such as a bullet) into the scalp, skull and dura (a thin layer of a soft tissue that covers the brain) causing damage along and around the penetration path. Closed-head traumatic brain injury is further broken down into three classifications: severe, moderate or mild, as shown in Table 1.1 (Adapted from DVBIC [14]). Briefly, severe TBI is usually accompanied by long loss of consciousness (LOC) and multiple lesions and

Table 1.1: Classification of closed-head injury adapted from DVBIC [14]. LOC=Loss Of Consciousness, hrs=Hours, mins=Minutes, *Confusion or Disorientation **Structural MRI

	Mild TBI	Moderate TBI	Severe TBI
LOC	≤30 mins	>30 mins & <24 hrs	≥24 hrs
Confusion*	<24 hrs	>24 hrs	>24 hrs
Memory Loss	<24 hrs	>24 hrs & <7 days	≥7 days
CT scan	normal	abnormal	abnormal
MRI**	normal	normal or abnormal	usually abnormal

hemorrhaging (physical tissue damage and internal bleeding) in the brain that can be clearly identified in standard medical imaging like Magnetic Resonance Imaging (MRI) or Computed Tomography (CT) scans. Moderate TBI is also easily identified using standard medical imaging, mostly CT scans, but it is usually accompanied by shorter LOC. However, mild TBI (mTBI) is more difficult to diagnose since it does not show any evidence of injury on standard imaging, especially at the very acute stage of injury, and LOC does not always accompany mTBI (classification information is adapted from DVBIC [14]).

High rates of mTBI combined with the difficulty of diagnosis have made it a major topic of research for the past few decades (Gerbeding and Binder [15], Namjoshi et al. [16], Krave et al. [17], Kerr et al. [18], Hollis et al. [19]). With the general public being aware of the increased rates and the devastating long-term disabilities

associated with mTBI, more pressure is being put on researchers and governments to better understand and ultimately decrease the rate of incidence. For these reasons, we choose to contribute towards the understanding of mTBI. An improved understanding of the mechanics of brain deformation during a traumatic event will also help in setting up better safety standards, in addition to helping physicians in the early diagnosis and treatment of mTBI.

1.2 Anatomy of the Head

The brain is surrounded by many other materials; making the structure of the head quite complicated. The brain "floats" in the skull due to the existence of a protective fluid called the Cerebro-Spinal Fluid (CSF). The CSF not only protects the brain, but also provides necessary nutrients and carries away metabolic wastes from the brain. Three layers of meninges surround and protect the brain: the dura, the arachnoid and the pia maters. The stiff dura extends to separate the left and right hemispheres forming the falx membrane, and separates the cerebrum from the cerebellum forming the tentorium membrane. The arachnoid space has multiple trabeculae that help cushion the brain and provide passageways for the CSF circulation (Saboori and Sadegh [20], Zoghi-Moghadam and Sadegh [21]).

In addition to the surrounding materials, the brain is a complicated structure on its own. A generalized categorization of the brain tissue divides it into two main components: white matter and gray matter. The gray matter consists mainly of

neural cell bodies and glial cells which are randomly oriented. On the other hand, the white matter mainly consists of axonal bundles surrounded by glial cells. The axonal bundles, through which the electrical signals of the brain travel, form a fiber network that is stiffer than the surrounding cells (Kruse et al. [22]).

An additional level of complexity to the brain tissue arises from the vascular network. The blood supply enters the brain from the base of the skull via major arteries (Vertebral/Basilar and Carotid) as shown in Figure 1.1 (Huettel et al. [5]). These arteries anastamose to form the Circle of Willis. Multiple branches originate before and from the Circle of Willis to provide the oxygenated blood to the whole brain. The blood flows through the brain tissue from arteries (the largest is 5 mm in diameter) to arterioles (few hundreds of μm in diameter) to the capillaries (up to a few μm in diameter). In the capillary bed, oxygen is supplied to the brain and deoxygenated blood travels from the capillaries to the venules and larger veins which drains into the sagittal and transverse sinuses and finally to the jugular vein.

1.3 Diagnosis of mTBI

To date, there is no unified or global clinical definition of mTBI. One of the first clinical classifications is the Glasgow Coma Scale (GCS) which is based on the patient's consciousness (eye opening and verbal and motor tasks) after the injury (Teasdale and Jennett [23]). A score of 13-15 on GCS indicates a mild injury. However since the GCS is built on a simple aspect (consciousness and responsiveness of the patient) other

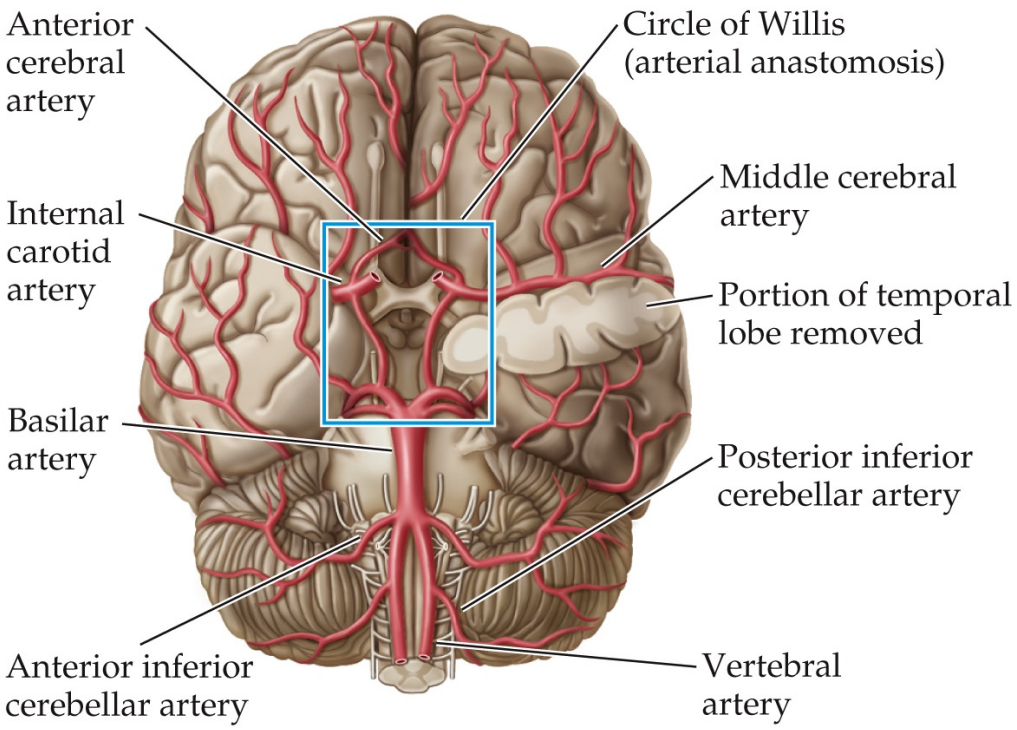

Figure 1.1: A bottom view of the brain showing major arteries and the circle of Willis (inside the rectangle) (Huettel et al. [5]).

organizations have created other scales or used GCS in addition to other conditions for mTBI classification. In 1991, the Colorado Medical Society classified mTBI based on confusion, amnesia and loss of consciousness (Kelly et al. [24]), and this was later (in 1997) amended by the American Academy of Neurology to include the patient's mental status (e.g.: orientation, concentration and memory tests) (Neurology [25]). Around the same time, the American Congress of Rehabilitation Medicine issued new criteria for mTBI based on GCS of 13-15 in addition to one or more of the following conditions: loss of consciousness, amnesia, change in mental status (like disorientation or confusion) or focal neurological deficits. In addition to these conditions, they

also added exclusion criteria which were loss of consciousness lasting more than 30 minutes, GCS <13 after 30 minutes and/or post traumatic amnesia lasting more than one day (Kay et al. [26]). A decade later the WHO Collaborating Center Task Force on Mild Traumatic Brain Injury also used similar, but more refined, diagnostic criteria. Beginning 30 minutes or more after injury the patient should score 13-15 on GCS and have one or more of the following: confusion, disorientation, loss of consciousness not exceeding 30 minutes, post traumatic amnesia lasting for a day or less, neurological abnormalities and intracranial lesion. In this criterion, if any other symptoms appeared the person should no longer be classified as an mTBI patient.

Of course there are other criteria issued by different centers (e.g.: Mayer et al. [27], Aubry et al. [28], McCrory et al. [29], Marshall et al. [30]), but the key point is the range of criteria for clinical diagnosis of mTBI. Further, the complete history of the patient can greatly affect the outcome of mTBI. For example, having previous head injuries increases symptoms and chances of long-term cognitive impairments (Mayer et al. [27], Harmon et al. [31], Dams-O'Connor et al. [32]). Moreover, repeated sub-concussive (lower loadings than what would normally cause mTBI) events might also cause neurological impairments or lead to chronic traumatic encephalopathy (Mayer et al. [27], Gardner and Yaffe [33], Stewart et al. [34]).

To help physicians in the early diagnosis of mTBI, computational models have been used to predict possible injuries in the brain given a defined loading condition. The location of predicted injuries can be connected to the possible loss of cognitive

functions through tractography maps of the brain. Efforts in computational modelling of mTBI will be discussed in the following section.

1.4 Computational Modeling of mTBI

Computational models are needed to investigate injurious events that can not be studied by performing controlled experiments on humans. There are several components in each computational model: structure, material models (characterization and constitutive modeling) and injury criteria. Section 1.2 discussed the head anatomy which provides information about possible head structures. We will discuss the other modeling components in the following subsections.

1.4.1 Brain Tissue Characterization

Extensive efforts have been made towards characterizing the brain tissue using multiple techniques. The experimental results show a wide range of mechanical behavior for the brain tissue. For example, the complex shear modulus of brain tissue quoted in the literature ranges from few hundred Pa to tens of kPa. Figure 1.2 shows a summary of these results presented by Meaney et al. [6] from multiple experimental studies: Shuck and Advani [35], Fallenstein et al. [36], Bilston et al. [37], Arbogast and Margulies [38], Peters et al. [39], Arbogast and Margulies [40], Thibault and Margulies [41], Brands [42], Bilston et al. [43], Darvish and Crandall [44], Lippert et al.

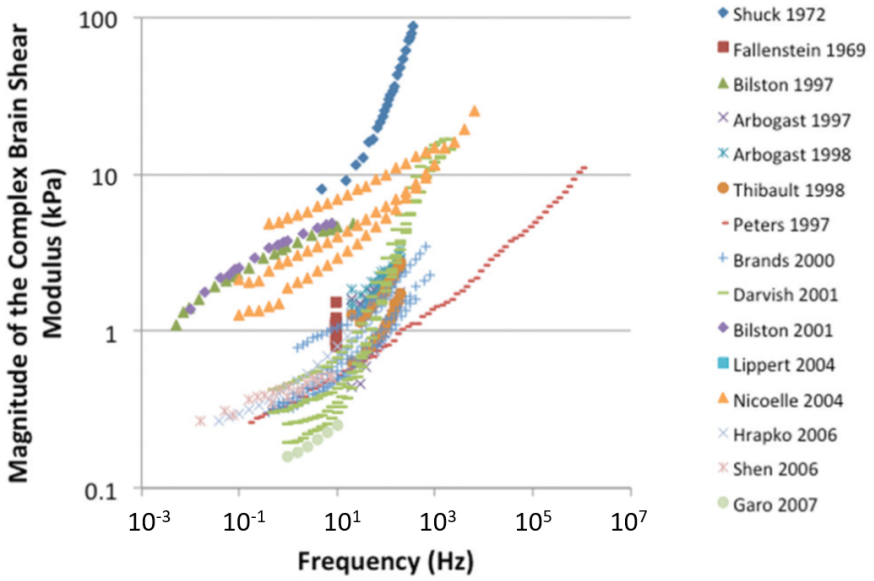

Figure 1.2: A wide range of the brain's complex shear modulus from experimental studies, summarized by Meaney et al. [6].

[45], Nicolle et al. [46], Hrapko et al. [47], Shen et al. [48] and Garo et al. [49]. Possible sources of this wide range include variations in age, post mortem time, strain rate, species and temperature of the sample. Further details of each potential source of variation are discussed in the following subsections.

1.4.1.1 Variations Between Species

Studies of brain tissue characterization in the literature have used samples from animals (like pigs (Gefen and Margulies [50]), cows (Pervin and Chen [51]), rats (Gefen et al. [52]), mice (Dodgson [53]), monkeys (Galford and McElhaney [54]) and rabbits (Koeneman [55])), in addition to human cadavers (Franceschini et al. [56]). Some data is obtained from tissues from patients undergoing brain surgery that is not be-

lieved to affect the brain properties (e.g. Prange and Margulies [57]). In recent years, Magnetic Resonance Elastography (MRE) provided the option of in-vivo mechanical characterization in humans (Kruse et al. [22], Green et al. [58]), mice (Clayton et al. [59]) and ferrets (Feng et al. [60]).

In an effort to study inter-species variability, Galford and McElhaney [54] compared shear properties of human and monkey brain samples. The shear modulus of monkey brain samples was 50% higher than human samples. Another work by Prange and Margulies [57], studied the differences between human and porcine brain properties. The study concluded that human brain is 30% stiffer than pocine brain. On the other hand, other groups did not find any differences between human and porcine tissues (Nicolle et al. [46, 61]), human and murine tissues (Atay et al. [62]) or human and rat tissues (Vappou et al. [63]). Figure 1.3 shows the scatter of the brain's shear modulus as a function of frequency obtained from multiple published studies in the literature (Chatelin et al. [7]). It is not clear that there are statistically significant differences between the moduli of humans and that of other species. However, the scatter of shear modulus data in Figure 1.3 suggests an increase in the shear modulus for all species with increasing frequency (e.g.: shear modulus G= 500 Pa at 0 Hz frequency, G= 2,000 Pa at 50 Hz and G=15,000 Pa at 1800 Hz frequency).

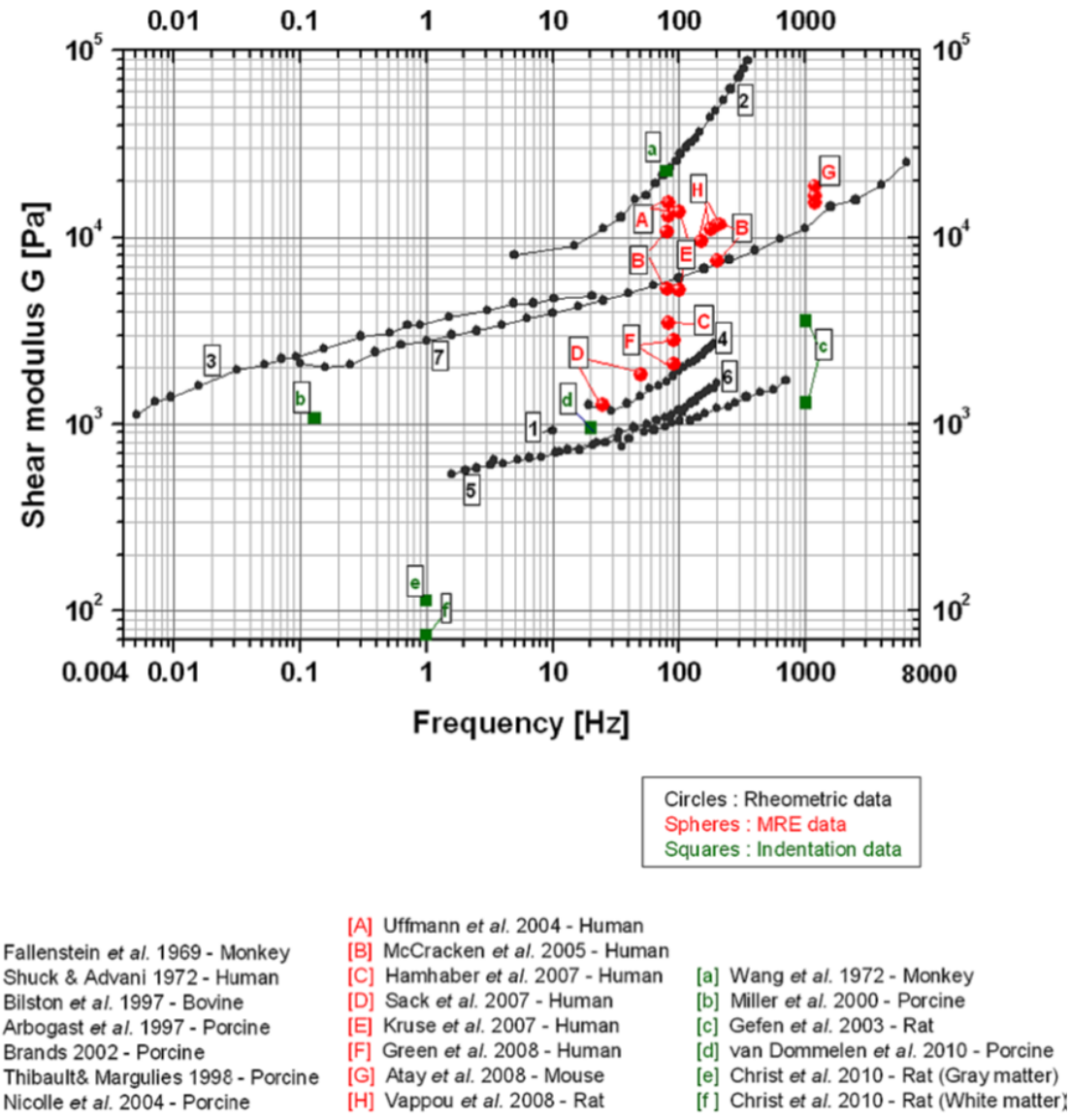

Figure 1.3: A comparative plot showing shear modulus response of brain samples from multiple species (Chatelin et al. [7]). We conclude from this scattering that there is no defined difference between the brain properties of humans and other animals in literature.

1.4.1.2 Influence of Age

In addition to the species differences, the change of brain tissue with respect to age is another factor that might affect the mechanical response. Thibault and Margulies [41] found an increase in stiffness as porcine age increased. Additionally, adult porcine tissues exhibited viscoelasticity while infant samples did not. A similar observation of increased stiffness with age was evident in the rat brain experiment of Elkin et al. [64]. In contrast, Sack et al. [65] showed a decrease in stiffness as human age increases using MRE technique (sample age range: 18-88 years). Overall, the stiffness of brain tissue is age dependent but it is not clear yet whether it decreases or increases with age.

1.4.1.3 Influence of Post-Mortem Time

In general, biological tissues including the brain are expected to degrade with post-mortem time, causing a change in their mechanical properties. To date, there is no specific protocol that controls experimental studies on the brain response in terms of post-mortem time. Hence, the different times in brain characterization experiments (ranging from a few hours to a few days post-mortem) can contribute to the wide scatter in reported brain properties.

Some experiments have shown insignificant effects of long post-mortem times on the brain's mechanical properties (Darvish and Crandall [44], Shen et al. [48], Atay

et al. [62]). However, Vappou et al. [63] performed experiments on rats to study post mortem effects which revealed a decrease of 50% in the brain's shear modulus was observed after 24 hours post-mortem. In contrast, the opposite trend was reported by Garo et al. [49] who performed experiments on porcine brains. Six hours post-mortem, they observed that the brain started to stiffen at a fixed rate of 27 Pa per hour. Hence, they recommended that brain tissue be tested within six hours post-mortem. This recommendation is not always followed in the literature.

1.4.1.4 Strain Rate Effects

There have been numerous efforts to study strain-rate effects on the mechanical properties of brain tissue (Table 1.2). Some efforts studied the related issue of change in the mechanical properties of the brain tissue with change in lodaing frequency (Shuck and Advani [35], Hrapko et al. [66]).

Most of these efforts used porcine brain tissue to study the effects of strain-rate on the mechanical properties of the brain (Miller and Chinzei [69, 70], TAMURA et al. [71, 72], Begonia et al. [73], Rashid et al. [74]). Begonia et al. [73] studied fresh porcine tissues under three compressive strain rates (0.00625, 0.025 and 0.1 s^{-1}). The study showed an increase in stiffness as the strain rate increased. A similar finding was made by Rashid et al. [74] who tested fresh porcine brain tissue in compression under strain rates of 30, 60 and 90 s^{-1}. Another supporting study to the findings above is the work of TAMURA et al. [72], who tested porcine tissue in tension with

Table 1.2: A summary of strain-rate studies in the literature. C=Compression, T=Tension, H=Human, B=Bovine, RM= Rhesus Monkey, P=Porcine, T_s=storage temperature, T_t=testing temperature, RT=Room Temperature, Rf=Refrigerated, NR=Not Reported.

Study	Test	Source	Rates/Frequencies	Temperature (^oC)
Estes and McElhaney [67]	C	H, RM	0.08, 0.8, 8, 40s^{-1}	T_t=37^o
Shuck and Advani [35]	S	H	5-350 Hz	NR
Donnelly and Medige [68]	S	H	30, 60, 90, 120, 180s^{-1}	T_s=4^o, T_t=RT
Jin et al. [2]	C,T,S	H	0.5, 5, 30s^{-1}	T_s=4^o, T_t=37^o
Miller and Chinzei [69]	C	P	0.64, 0.0064 and 0.64x10$^{-5}s^{-1}$	T_s=5^o, T_t=22^o
Miller and Chinzei [70]	T	P	0.64, 0.0064s^{-1}	T_s=5^o, T_t=22^o
TAMURA et al. [71]	C	P	1, 10, 50s^{-1}	T_s=Rf, T_t=20^o
Hrapko et al. [66]	S	P	1-10Hz	T_s=4^o, T_t=7-37^o
TAMURA et al. [72]	T	P	0.9, 4.3, 25s^{-1}	T_s=4^o, T_t=RT
Begonia et al. [73]	C	P	0.00625, 0.025, 0.1s^{-1}	T_t=25^o
Rashid et al. [74]	C	P	30, 60, 90s^{-1}	T_s=4-5^o, T_t=22^o
Pervin and Chen [51]	C	B	0.01, 0.1, 1000, 2000, 3000s^{-1}	T_s=37^o, T_t=25^o
Bilston et al. [43]	S	B	0.01-20Hz	NR

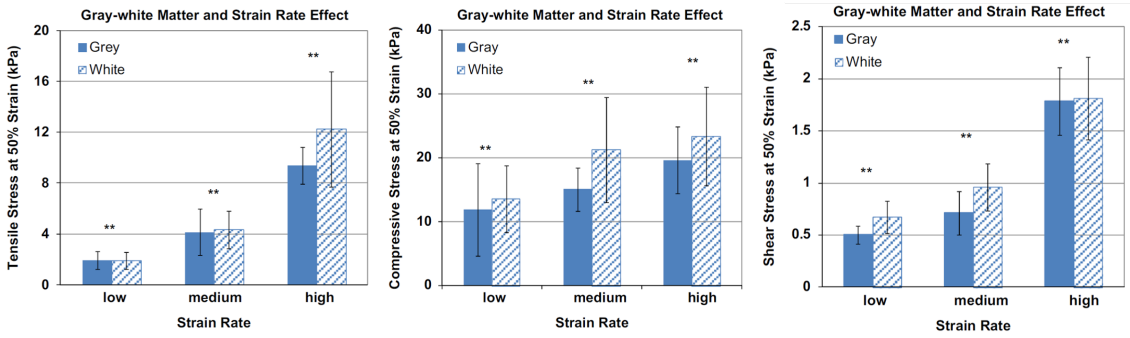

(a) **(b)** **(c)**

Figure 1.4: Summary of average stress at 50% strain of gray and white matters at varying strain rates from the study by Jin et al. [2]. **p<0.001. (a) Tension, (b) Compression, and (c) Shear test results.

strain rates of 0.9, 4.3 and 25 s^{-1}, and observed an increase in the stiffness as the strain rate increased. Overall, porcine brain tissue has been shown to be stiffer as strain-rate increases regardless of the loading mode (tension or compression).

Human brain samples also showed the same behavior in a set of experiments carried out by Jin et al. [2]. Cadaver brain tissue was tested in tension, compression and shear under three strain rates: 0.5, 5 and 30 s^{-1} (low, medium and high, shown in Figure 1.4). For all the tests performed, a clear dependency of the strain rate was evident. Altogether, the brain tissue is dependent on the strain rate regardless of the species or the testing direction (compression, tension or shear).

1.4.1.5 Temperature Effect

The temperature at which brain samples are stored and the temperature of the tissues at the time of testing also affects the mechanical response of such soft biological tissues. The work of Hrapko et al. [66] revealed an increase in the brain modulus with the decrease of temperature, using porcine brain tissue under high-rate compression tests. Another study by Peters et al. [39] reached the same conclusion using bovine (calf) brain tissue. On the other hand, an increase in tissue stiffness stored at 37^{o}C vs 0^{o}C of porcine tissue was reported by Zhang et al. [75]. Since most tissues in the literature are preserved between freezing (0^{o}C) and body (37^{o}C) temperatures, part of the variability in the brain's mechanical characteristics comes from the different storage temperatures. Note that storage and/or testing temperatures are not always recorded in the literature.

1.4.2 Constitutive Modeling

1.4.2.1 Brain Tissue Constitutive Modeling

Material models used to describe the brain tissue have evolved over the years. Linear elasticity was initially used to model the behavior of the brain tissue (e.g., Kimpara and Iwamoto [76], Zhang et al. [77], Roberts et al. [78], Chatelin et al. [79]). Hyperelasticity began to be used (Kyriacou et al. [80], Rashid et al. [81], Mihai et al. [82], Laksari et al. [83]) as the evidence of the non-linear behavior of the brain tis-

sue accumulated (Jin et al. [2], Budday et al. [84]). Table 1.3 summarizes the most commonly used constitutive models for the brain in the mTBI literature. Recently, many computational models use the Holzapfel-Gasser-Ogden (HGO) model which is an anisotropic hyperelastic constitutive law. The usage of an anisotropic model for the brain tissue comes from two main reasons: evidence of brain tissue anisotropy (Velardi et al. [1], Jin et al. [2], Arbogast and Margulies [40], Feng et al. [85], Diguet et al. [86]) and correlation of fiber orientation with damage measures (discussed in the next subsection).

Researchers have also used structural (Arbogast and Margulies [97], Meaney [98]) and biphasic models (Franceschini et al. [56], Cheng and Bilston [99], Basser [100]) to describe the brain tissue. The idea behind structural modeling is to capture the nature of axonal fibers in the brain which are not naturally fully stretched. Hence, the fibers will not be engaged at smaller strains. Once a specific strain value is reached, the fibers will be fully stretched and add extra stiffness to the brain tissue. Biphasic models, as the name suggests, treat the brain tissue as a mixture of two phases: solid and fluid. This idea is supported by the high content of water in the brain tissue (Tauber et al. [101]). The key advantage of biphasic models is the ability to capture fluid diffusion in the brain which is only captured at small strain-rates. Thus, for dynamics injurious loading conditions the biphasic models are typically not used.

Table 1.3: A summary of the constitutive models used for the brain tissue in mTBI literature. Iso=Hyperelastic Isotropic, Aniso=Hyperelastic Anisotropic.

Constitutive Model	Type	References
Linear Elastic	-	Kimpara and Iwamoto [76], Zhang et al. [77], Roberts et al. [78], Chatelin et al. [79]
Neo-Hookean	Iso	Kyriacou et al. [80], Budday et al. [87], MacManus et al. [88]
Mooney-Rivlin	Iso	Rashid et al. [81], Laksari et al. [83], Mendis et al. [89]
Fung	Iso	Rashid et al. [81], Mihai et al. [82], Rashid et al. [90]
Ogden	Iso	Prange and Margulies [57], MacManus et al. [88], Rashid et al. [90], Kaster et al. [91]
Quadratic Anisotropic	Aniso	Wright and Ramesh [92], Ning et al. [93]
Holzapfel-Gasser-Ogden	Aniso	Wright et al. [3], Giordano and Kleiven [94, 95], Colgan et al. [96]
Structural	-	Arbogast and Margulies [97], Meaney [98]
Biphasic	-	Franceschini et al. [56], Cheng and Bilston [99], Basser [100]

1.4.3 Injury Criteria

A variety of brain injury criteria have been developed over the past decades. We will divide them into three categories: Macroscale based, Microscale based and Cellular level injury criteria which are described in the next subsections.

1.4.3.1 Macroscale (Head) Based Injury Criteria

Due to the ease of measuring general head kinematics (compared to local tissue deformations), macroscale injury criteria were developed and are often used in automotive safety and contact sports. Some criteria were developed using several reconstructed injurious and non-injurious events. The ratio of injury incidents to the total incidents (injurious and non-injurious) for a specific loading can provide a probabilistic measure of injury occurrence.

The first published injury criterion was published in the 1960 by Lissner et al. [102] (which is also published in 1966 by Gurdjian et al. [8]) and is frequently referred to as The Wayne State Tolerance Curve (WSTC) (Figure 1.5, adapted from Greenwald et al. [9]). The curve defines a relationship between the maximum linear acceleration and the impact duration (extracted from animal and cadaver head experiments), and any point above the curve is considered an injurious condition.

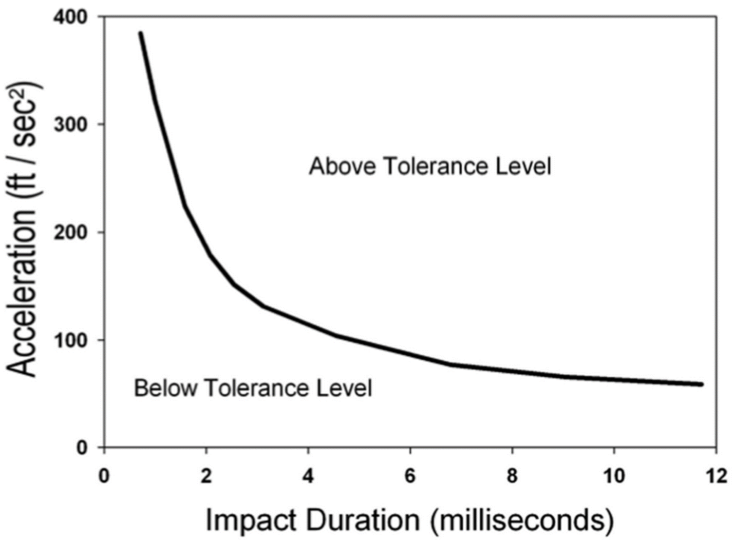

Figure 1.5: The Wayne State Tolerance Curve which is used as a brain injury predictor (Gurdjian et al. [8], Greenwald et al. [9])

Around the same time, The Gadd Severity Index (GSI) was proposed by Gadd [103] which is of the form

$$GSI = \int_0^t a^{2.5} dt \tag{1.1}$$

where a is the effective acceleration (in g's) and t is the time (in seconds). Based on the WSTC, Gadd [103] proposed a threshold value of GSI=1000 beyond which the brain will be injured.

In 1972, the National Highway Traffic Safety Administration (NHTSA) established the Head Injury Criterion (HIC) (Marjoux et al. [104], based on Versace [105]'s data), defined as

$$HIC = \left\{ (t_2 - t_1) \left\{ \frac{1}{t_2 - t_1} \int_{t_1}^{t_2} a dt \right\}^{2.5} \right\}_{max} \tag{1.2}$$

where a is the resultant head acceleration in g's and t_1 and t_2 are in seconds. Based on the NHTSA recommendation in the Federal Motor Vehicle Safety Standards And Regulations (FMVSS), the time interval $(t_2 - t_1)$ should be either 15 or 36 milliseconds (Giordano and Kleiven [94]).

The first work to introduce angular acceleration into head injury criteria was published a little less than two decades after HIC by Newman [106]. They developed the Generalized Acceleration Model for Brain Injury Tolerance (GAMBIT) which takes the following form

$$GAMBIT, G(t) = \left\{ \left(\frac{a(t)}{a_c} \right)^m + \left(\frac{\alpha(t)}{\alpha_c} \right)^n \right\}^{\frac{1}{s}} \tag{1.3}$$

where a is the linear acceleration (in g's), α is the rotational acceleration (in rad/s^2), and the values of m, n, s, a_c and α_c were fitted to field accident data of Kramer and Appel [107] ($n = m = s = 2.5, a_c = 250g$ and $\alpha_c = 25rad/s^2$). A study based on pedestrian collisions suggested $G = 1$ for 50% probability of severe head injury (Feist et al. [108]).

Newman later collaborated with other researchers to develop a new criterion called the Head Injury Power (HIP) (Newman et al. [109, 110])

$$HIP = \sum_{i=1}^{3} ma_i \int a_i dt + \sum_{i=1}^{3} I_{ii}\alpha_i \int \alpha_i dt \tag{1.4}$$

where m is the mass (in kg), I_{ii} is the moment of inertia in the i^{th} direction (in kgm^2), a is the translational acceleration (in g's), α is the rotational acceleration (in rad/s^2).

A value of HIP≈12.8 kW was set for 50% probability of concussion (Newman et al. [109]).

The most recent macroscale injury criterion is the Brain Injury Criterion (BrIC) proposed by Takhounts et al. [111]. While none of the previous criteria used angular velocity as a predictor, this work defined BrIC as

$$BrIC = \sqrt{\left(\frac{w_x}{w_{xc}}\right)^2 + \left(\frac{w_y}{w_{yc}}\right)^2 + \left(\frac{w_z}{w_{zc}}\right)^2} \tag{1.5}$$

where w_x, w_y and w_z are maximum angular velocities around each axis and w_{xc}, w_{yc} and w_{zc} are critical angular velocities calculated from a Cumulative Strain Damage Measure (CSDM) of 0.5 based on a selected strain threshold (covered in the next section). Hence, if the value of BrIC=1, a 50% probability of concussion is expected.

1.4.3.2 Microscale (Tissue) Based Injury Criteria

Multiple tissue-scale deformation measures have been used as injury criteria including multiple stresses (e.g.: von Mises stress (Anderson et al. [112]), shear stress (Yao et al. [113]) or pressure (Ward et al. [114])) and strains (e.g: shear strain (Kimpara and Iwamoto [76]), principal strain(Deck and Willinger [115]), Cumulative Strain Damage Measure (CSDM) (Takhounts et al. [116]), strain rate (King et al. [117]) or a combination of strain and strain rate (Viano and Lovsund [118])) (Table 1.4). To set a specific threshold, real-world injurious event reconstruction (e.g. Zhang et al. [119], Kleiven [120], Trosseille et al. [121]) or laboratory animal studies (e.g. Anderson et al. [112], Shreiber et al. [122], Margulies and Thibault [123]) are used.

Table 1.4: Injury thresholds developed from either accident reconstrcution or animal studies published in the literature. AR=Accident Reconstruction, AS=Animal Study, CP=Coup Pressure, CCP= Contrecoup Pressure, CSDM=Cumulative Strain Damage Measure, X%p=X% probability of injury.

Threshold	Value	Method	Reference
Von Mises Stress	30kPa	AS	Anderson et al. [112]
Shear Stress	7.9kPa	AR	Yao et al. [113]
Pressure	CP=256kPa, CCP=-125kPa	AR	Ward et al. [114]
Shear Strain	31.6%	AR	Kimpara and Iwamoto [76]
Principal Strain	31%	AR	Deck and Willinger [115]
CSDM	0.15	AS	Takhounts et al. [116]
Strain Rate	$60s^{-1}$ for 50%p	AR	King et al. [117]
Strain $\times$ Strain Rate	$36s^{-1}$	AS	Viano and Lovsund [118]

1.4.4 Cellular Level Injury Criteria

In-vivo and in-vitro experiments on animal nerves or cell cultures have been performed to obtain injury thresholds at the cellular level. Stretching is applied to cell cultures (Weber et al. [124], Geddes and Cargill [125], Elkin and Morrison III [126], Morrison III et al. [127]) or a single nerve (one family of fiber bundles) (Bain and Meaney [128], Gray and Ritchie [129], Saatman [130]) and the morphology, cell integrity or nerve function is monitored throughout the experiment. The onset of change (e.g.: cell degeneration or death, abnormal cell signals or abnormal morphology) defines the strain threshold for injury prediction. Table 1.5 shows some of the injury thresholds obtained at the cellular level.

The cellular level injury criteria can not be directly applied on the tissue level due to the difference in the length scale between the two. Tamura et al. [131] studied the difference between the global (tissue level) and local (cellular level) tissue strains by performing experiments on fresh porcine brain samples. The recorded global tensile and compressive strains in the tissue were 0.33 and -0.12, respectively, while the strains were 0.07 and -0.03, respectively, in the nerve fibers (cellular level). Hence, a relationship between the tissue level and cellular level strains must be defined before using cellular level criteria for global tissue injury predictions.

Further more we should note that cellular level injury criteria have been defined under different strain-rates. Geddes and Cargill [125] found that the response of cell

Table 1.5: Cellular level injury thresholds derived experimentally in-vivo and in-vitro.

Experiment	Strain Threshold	Reference
Cell cultures	0.2-0.3	Geddes and Cargill [125]
	0.1-0.2	Elkin and Morrison III [126]
	0.2	Morrison III et al. [127]
	0.31	Weber et al. [124]
Single Nerve	0.18	Bain and Meaney [128]
	0.33	Gray and Ritchie [129]
	0.15-0.25	Saatman [130]

cultures is strain rate dependent (for three tested strain-rates 1, 5 and 10/s) while Elkin and Morrison III [126] experimental results indicate that cell death is dependent on the combination of strain and strain-rate (five different strain-rates tested: 0.1, 1, 10, 20 and 50/s). On the other hand, Cullen and LaPlaca [132] found that cell cultures viability (in 2D and 3D setups) is not strain-rate dependent using two rates of 20 and 30/s. Thus, the selection of an injury criterion should ideally be for the appropriate strain-rate associated with the intended application to avoid strain-rate effects.

1.5 Overview of the Thesis

In the previous sections we showed multiple aspects that could introduce heterogeneity in the brain response including, but not limited to, structural variations and material characterization. In this work, multiple aspects of heterogeneity are investigated. First, the effect of white matter shear anisotropy in the injury predictions of mTBI is investigated in Chapter 2. Two models, one with shear anisotropy and one without, are simulated for an injurious loading and the predicted damage will be compared between the two. The following two chapters (Chapters 3 and 4) address the role of incorporating the vasculature network in a 3D head model for mTBI predictions. Maximum strains, strain distributions and injury predictions are compared between two models, with and without the vasculature network. The last aspect of heterogeneity in this work is the gray matter, which is discussed in Chapter 5. Two models, one with homogeneous gray matter and one with heterogeneous gray matter, are used to simulate an injurious loading. Finally, the work is summarized and future directions will be suggested in Chapter 6.

Chapter 2

Shear anisotropy in mTBI: A white matter constitutive model

2.1 Introduction

Most early TBI computations treated brain tissue as isotropic material (Zhang et al. [77], Zhou et al. [133], Kleiven and von Holst [134], El Sayed et al. [135], Taylor and Ford [136]). With the discovery of the brain's fiber network, some TBI models have used anisotropic descriptions for the white matter and isotropic descriptions to represent gray matter (Velardi et al. [1], Wright et al. [3], Wright and Ramesh [92]). The anisotropic models have been developed by using both continuum (e.g.Ning et al. [93]) and structural (e.g.Lanir [137]) approaches. However, all of the TBI models to

date have accounted for anisotropy in tension but not in shear, despite clear evidence of shear anisotropy in white matter (Jin et al. [2]).

The finite element method is often used as a computational tool to study mTBI and estimate injury in humans. These models are either two dimensional (2D)(Wright et al. [3], Wright and Ramesh [92], Shugar and Katona [138]) or three dimensional (3D)(Zhang et al. [77], Roberts et al. [78], Chatelin et al. [79], Colgan et al. [96], Ward and Thompson [139], Ruan et al. [140]) models, and differ greatly in the anatomical details that are considered, ranging from low to high fidelity.

In this chapter we will address white matter heterogeneity by developing a material model for white matter that captures anisotropy in both tension and shear. The material parameters are determined by calibration with respect to data from the literature and the calibrated model is then validated against live human data in a non-injurious content. The validated model is then used to simulate a specific National Hockey League (NHL) incident that resulted in injury. In order to demonstrate the role of shear anisotropy in mTBI modelling, the results of the new material model are compared to the results obtained with a model that includes only tension anisotropy.

2.2 Materials and Methods

The materials in brain tissue are typically separated into two types: white matter and gray matter. The gray matter primarily consists of neuronal cell bodies and is typically modeled as an isotropic material. On the other hand, the white matter is

largely composed of axons surrounded by various types of glial cells forming a network of fiber bundles. The existence of this network causes the material to have a different response if stretched parallel to the fiber direction than if stretched perpendicular to the fiber direction (Velardi et al. [1]). A similar anisotropy applies to the shear response (Jin et al. [2]). Thus, white matter is an anisotropic material in both tension and shear. In this section, a constitutive model for white matter is described which includes both modes of anisotropy.

2.2.1 Constitutive Model

We start with a simple volume of material with fibers in one direction (Figure 2.1a). The initial fiber direction $\mathbf{a_0}$ in the reference configuration and the new fiber vector $\mathbf{a}$ in the deformed configuration are related through the deformation gradient $\mathbf{F}$ and the fiber stretch λ by

$$\mathbf{F}\mathbf{a_0} = \lambda\mathbf{a}. \tag{2.1}$$

The strain energy function for a transversely isotropic material is usually represented using three invariants for the isotropic response of the material,

$$I_1 = tr\mathbf{C}, \qquad I_2 = \frac{1}{2}[(tr\mathbf{C})^2 - tr(\mathbf{C}^2)], \qquad \text{and} \qquad I_3 = \det\mathbf{C}, \tag{2.2}$$

and two pseudo-invariants for the anisotropic response (Spencer [141])

$$I_4 = \mathbf{a_0}\cdot\mathbf{C}\cdot\mathbf{a_0} = \lambda^2 \qquad \text{and} \qquad I_5 = \mathbf{a_0}\cdot\mathbf{C}^2\cdot\mathbf{a_0} \tag{2.3}$$

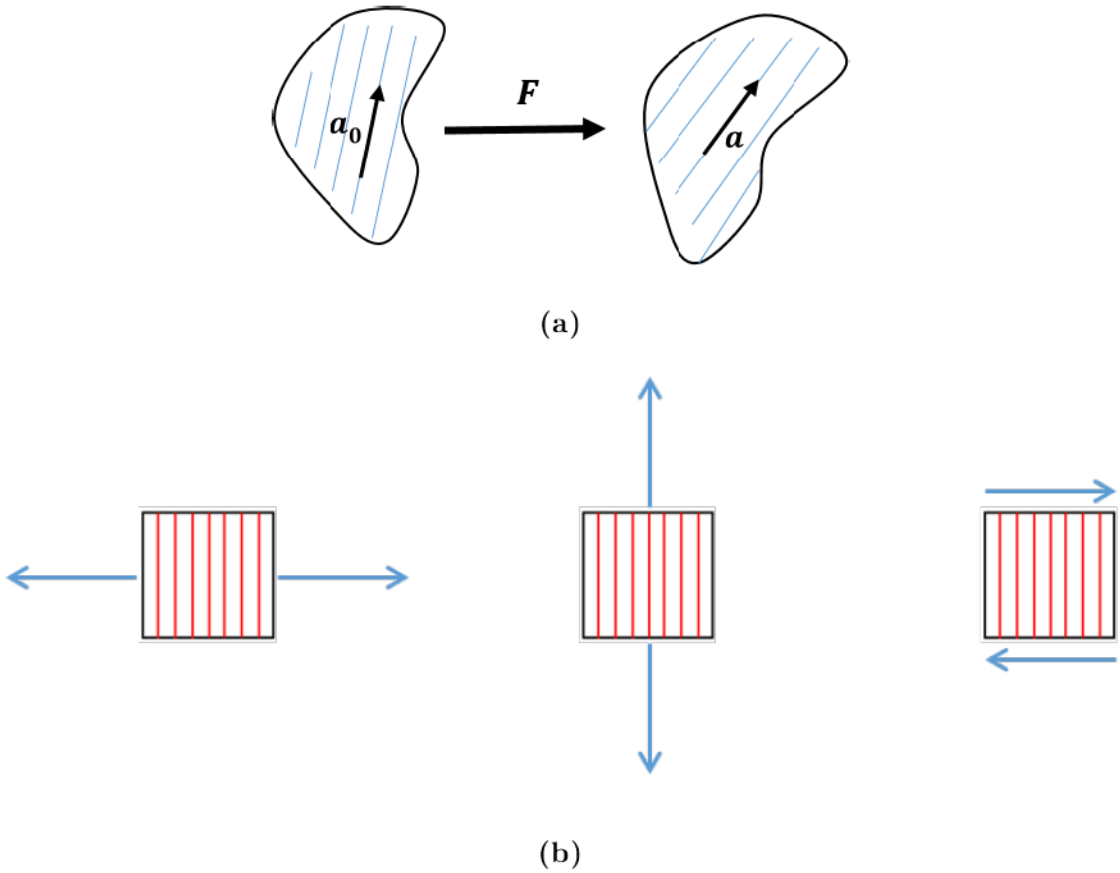

Figure 2.1: Schematic showing the deformation of the anisotropic white matter. Assuming a single family of fibers in the constitutive model, a) the fiber direction changes from $\mathbf{a_0}$ to $\mathbf{a}$ after the application of the deformation gradient $\mathbf{F}$. b) Schematic showing an example of the three experiments that are needed in order to obtain the material parameters for the shear anisotropic constitutive model.

where $\mathbf{C}$ is the Right Cauchy-Green tensor. Note that while I_4 depends only on the fiber stretch, I_5 is much more complex. The fifth invariant, I_5, carries information about the interactions between the fiber and the other component which is the matrix material in our case (Holzapfel [142]). Since white matter is a nearly incompressible material and the model will be used in a finite element computation, the strain energy function is assumed to be partitioned to avoid shear locking, so that

$$W = W_{Volumetric} + W_{Isochoric} \tag{2.4}$$

where $W_{Volumetric}$ is the strain energy part allowing volume change and $W_{Isochoric}$ captures deformation without any change in volume. The deformation gradient tensor F is modified to

$$\mathbf{F} = J^{\frac{1}{3}}\overline{\mathbf{F}} \tag{2.5}$$

where $J = \det\mathbf{F}$ is the volume ratio ($W_{Volumetric}$=$f(J)$) and $\overline{\mathbf{F}}$ is the deformation gradient with constant volume ($W_{Isochoric}$=$f(\overline{\mathbf{F}})$). Accordingly the invariants $\overline{I}_i$ are expressed in terms of the modified Cauchy-Green tensor $\overline{\mathbf{C}} = \overline{\mathbf{F}}^T\overline{\mathbf{F}}$. We now assume that the isochoric strain energy, $W_{Isochoric}$, is composed of two parts, one representing the isotropic response of white matter (assumed to be Neo-Hookean) and the other representing the fiber reinforcement:

$$W_{Isochoric} = W_{Isotropic} + W_{Anisotropic} \tag{2.6a}$$

$$W_{Isotropic} = C_1(\overline{I}_1 - 3) \tag{2.6b}$$

$$W_{Anisotropic} = C_2(\overline{I}_4 - 1)^2 + C_3(\overline{I}_5 - \overline{I}_4{}^2) \tag{2.6c}$$

where C_1, C_2 and C_3 are material parameters. The $W_{Anisotropic}$ incorporates anisotropy in both tension and shear, and $\overline{I}_1$, $\overline{I}_4$ and $\overline{I}_5$ are defined analogously to I_1, I_4 and I_5 when $\mathbf{F}$ is replaced by $\overline{\mathbf{F}}$. Note that the second term in equation 2.6c represents the fiber-matrix interaction only. The values of the material parameters C_1, C_2 and C_3 can be determined (e.g.) from three experiments:

1. Tension perpendicular to the fibers to obtain C_1 since this mode is dominated by the matrix response to deformation.

2. Tension along the fiber direction to obtain C_2 (mode dominated by the fiber stretch contribution).

3. Shear perpendicular to the fibers to obtain C_3 (mode dominated by the fiber-matrix shear interaction).

We note that, to our knowledge, previous mTBI anisotropic white matter models have not accounted for the fiber-matrix interactions and I_5 in the formulation despite the recommendation to use both invariants (I_4 and I_5) to model transversely anisotropic soft tissues (Murphy [143]) and to include at least three invariants to model non-linear transversely isotropic materials (Destrade et al. [144]).

Finally, the volumetric part of the strain energy is described in terms of the volume ratio J and the bulk modulus K, as is widely used in other studies for white matter (Colgan et al. [96], Cloots et al. [145], Ganpule et al. [146])

$$W_{Volumetric} = \frac{K}{2}\left(\frac{J^2-1}{2} - lnJ\right) \tag{2.7}$$

Note that this formulation fulfills all the requirements for a volumetric strain energy function (e.g. behavior in extreme tension or compression) as discussed in the work by Doll and Schweizerhof [147].

With these definitions of the strain energy, the constitutive equation of white matter can be derived following Holzapfel [142] with the Cauchy stress tensor $\boldsymbol{\sigma}$ related to the strain energy density by

$$\boldsymbol{\sigma} = \frac{2}{J}\left\{\overline{I}_3\frac{\partial W}{\partial \overline{I}_3}\mathbf{I} + \left(\frac{\partial W}{\partial \overline{I}_1} + \overline{I}_1\frac{\partial W}{\partial \overline{I}_2}\right)\overline{\mathbf{b}} - \frac{\partial W}{\partial \overline{I}_2}\overline{\mathbf{b}}^2 + \overline{I}_4\frac{\partial W}{\partial \overline{I}_4}\mathbf{a}\otimes\mathbf{a} + \overline{I}_4\frac{\partial W}{\partial \overline{I}_5}(\mathbf{a}\otimes\overline{\mathbf{b}}\mathbf{a} + \mathbf{a}\overline{\mathbf{b}}\otimes\mathbf{a})\right\} \tag{2.8}$$

where $\mathbf{I}$ is the identity tensor and $\overline{\mathbf{b}} = \overline{\mathbf{F}}\overline{\mathbf{F}}^T$ is the modified Left Cauchy-Green tensor.

To understand the effects of the shear anisotropy (I_5), we compare our results to those obtained using an anisotropic model without shear anisotropy: the Holzapful-Gasser-Ogden (HGO) model which was used by Wright et al. [3]. For a single family of fibers in a representative volume, the HGO model used by Wright et al. [3] was:

$$\begin{aligned} W_{Isotropic} &= C_1(\overline{I}_1 - 3), \\ W_{Anisotropic} &= \frac{k_1}{2k_2}\left\{e^{k_2\langle\overline{E}\rangle^2} - 1\right\}, \end{aligned} \tag{2.9}$$

where $\overline{E} = \kappa(\overline{I}_1 - 3) + (1 - 3\kappa)(\overline{I}_4 - 1)$, k_1 is a parameter representing tension anisotropy, k_2 is a scaling factor and κ is the fiber dispersion parameter. Note that the special case of $\kappa = 0$ and a single fiber family and for small k_2 (as in Wright et al. [3]), equation 2.9 reduces to the same form as equation 2.6 with $C_3 = 0$ (i.e., only the $\overline{I_4}$).

2.2.2 Material Properties

Now that we have defined the constitutive models, we need to determine the parameters C_1, C_2 and C_3 of equation 2.6, k_1, k_2 and κ of equation 2.9 and the bulk modulus K of equation 2.7. Parameters for equation 2.9 were taken directly from Wright et al. [3] (Table 2.1). The bulk modulus K is chosen to be $2.19GPa$, consistent with some (but by no means all) of the prior literature for TBI computations(Yao et al. [113], Takhounts et al. [116], Watanabe et al. [148]).

Since we expect the brain tissue to be strain-rate dependent (Estes and McElhaney [67], TAMURA et al. [72], Begonia et al. [73], Budday et al. [149]), we incorporate viscoelastic effects through a Prony series (described in the next subsection). For this particular implementation, C_1, C_2 and C_3 should be determined from low strain rate data of tension and shear experiments performed with respect to the dominant fiber direction, and there are few studies that have this information. Jin et al. [2] examined tissues from four regions of human adult brains: Cortex, Thalamus, Corpus Callosum and Corona Radiata. Compression, tension and shear tests with respect to fiber direction were performed for all four regions using three strain rates (0.5, 5 and $30s^{-1}$). An attempt to fit all the material parameters to the $0.5s^{-1}$ strain rate data (lowest strain rate in Jin et al. [2]'s dataset) results in a negative value for C_3, which is not allowed in this hyperelastic model. It is possible that there are variations in the experimental data because of effects such as the long post-mortem time of the samples

(averaging 4 days post mortem) or the fact that each test direction was performed on a different subject (gender and age differed, the latter ranging from 48 to 94 years). The net result is that we can not use the three tests of the low strain rate ($0.5s^{-1}$) in Jin et al. [2] experiment to determine the full set of C_1, C_2 and C_3. Instead we consider the work of Velardi et al. [1]. They performed tensile tests on fresh adult porcine brain tissue from three different regions: Cortex, Corpus Callosum (CC) and Corona Radiata (CR) at a strain rate of $0.1s^{-1}$. For both CC and CR, tension tests were performed both parallel and perpendicular to the fibers allowing us to obtain C_1 and C_2 (Figure 2.2 (top and middle, respectively)). However, Velardi et al. [1] did not perform shear testing with respect to the fiber direction. To obtain C_3, therefore, we used the work of Jin et al. [2]. The parameter C_3 is determined by fitting the Jin et al. [2] results for shear perpendicular to the fiber direction (Figure 2.2 (bottom)). A nonlinear least squares method was used for all parameters, which are shown in Table 2.1. Since both experimental studies (Velardi et al. [1], Jin et al. [2]) we used for the fitting are performed under low strain rate loading (0.1 and $0.5s^{-1}$ respectively), we consider the fitted parameters to define the long-term response of the material. The viscoelastic modulus behavior will be described in the next subsection.

Given the availability of data, we have had to mix two tissue sources (porcine and human) when obtaining our parameters. Prange and Margulies [57] compared the properties of porcine and human brain tissue, and found that human brain tissue was stiffer than the porcine tissue. On the other hand, Nicolle et al. [61] obtained shear

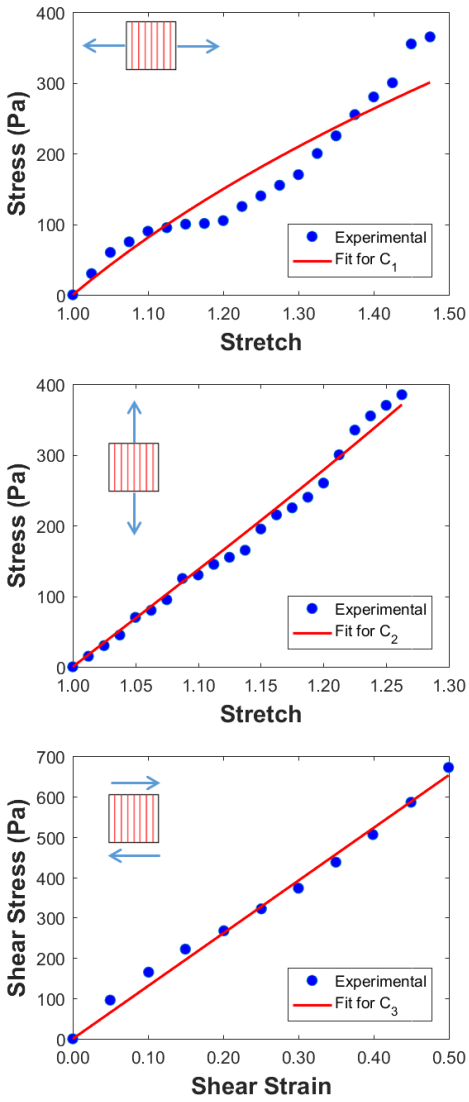

Figure 2.2: Determination of the material parameters for the shear anisotropic model (equation 2.6). The first Piola-Kirchhoff (PK) stress is plotted vs. the corresponding stretch (top and middle), and vs. the shear strain (bottom). The experimental measurements are taken from the work of Velardi et al.Velardi et al. [1] and Jin et al.Jin et al. [2]The fits allow us to obtain C_1 (top), C_2 (middle) and C_3 (bottom). Note: the relationship between the 1^{st} PK stress (P) and the Cauchy stress $\boldsymbol{\sigma}$ (equation 2.8) is $J\boldsymbol{\sigma} = \mathbf{F}\mathbf{P}^T$.

Table 2.1: Values for the material parameters in the shear anisotropic model (equation 2.6) determined by fitting the results of Velrdi et al.Velardi et al. [1] and Jin et al.Jin et al. [2], and in the HGO model (equation 2.9) used by Wright et al.Wright et al. [3]

	Shear Anisotropic Model	HGO Model
C_1(Pa)	148	3200
C_2(Pa)	61	-
C_3(Pa)	505	-
k_1(Pa)	-	2716
k_2	-	0.0001
κ	-	From DTI$(0 - 1/3)$

viscoelastic material properties for porcine tissue, compared them to human tissue properties reported in the literature, and concluded that porcine tissue stiffnesses were within the range of human tissue stiffnesses. Similarly, Nicolle et al. [46] found no difference in the material properties of the brain tissue between the two species. In this context of the data in the available literature, we believe that using two different tissue sources to calibrate our model is reasonable.

2.2.3 Finite Element Head Model*

Our Finite Element (FE) head model is based on Magnetic Resonance Image (MRI) data of a healthy human(Wright et al. [3]). For simplicity, we consider three 2D slices (extracted from the 3D MRI), one for each plane: axial, coronal and sagittal. Each slice is segmented for the following brain structures when appropriate: skull, dura (with falx and tentorium), Cerebro-Spinal Fluid (CSF), gray matter, white matter, cerebellum, bridging veins and ventricles (Figure 2.3).

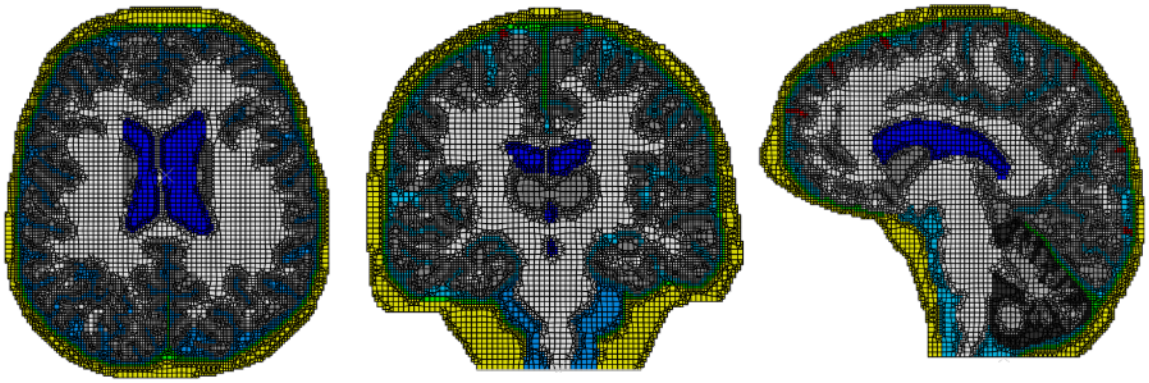

Figure 2.3: The 2D finite element head models from the three representative planes: Axial (left), Coronal (middle) and Sagittal (right). The models include multiple brain structures that have been segmented from the MRI data.

The shear anisotropic model described in the previous section is used for white matter, with the primary fiber bundle direction assigned by co-registering the MRI with Diffusion Tensor Imaging (DTI) of the same subject, with the dominant direction

*Implemented in ABAQUS commercial software version 6.13-3, Dassault Systémes Simulia Corp., Providence, RI.

of the fiber bundle for each voxel recorded. Since gray matter does not have a preferred orientation, we used equation 2.9 with the fiber dispersion κ set to 1/3 for gray matter. Since the brain tissue mechanical behavior is dependent on the strain rate (Estes and McElhaney [67], Donnelly and Medige [68], TAMURA et al. [72], Rashid et al. [74]), we adapted a one-term Prony series shear modulus to compensate for the strain rate effect from Wright et al. [3]. The calibrated shear modulus ($2C_1$) is considered as the long-term shear modulus, and using a commonly reported ratio long-term and short-term moduli (Wright et al. [3], Zhang et al. [119]) the value of the long-term modulus is extracted. Tables 2.2 and 2.3 summarize the material models and parameters, respectively, for all other structures.

All other details about the material models and properties used for each structure (other than what we derived here for the white matter) may be obtained from Wright et al. [3], which we use as a benchmark. Both our computational simulations and Wright et al. [3] are two dimensional with identical head structure and mesh. Validation of both models is performed using an in-vivo brain deformation experiment on a human subject (covered in the next subsection). In this way, we focus on the effects of shear anisotropy and eliminate all other sources that could produce differences in the results.

Since finite element calculations can be affected by the mesh size, we conducted a mesh sensitivity analysis. A constant angular acceleration is applied to three mesh sizes: 1) Fine mesh with max element size of 1 mm 2) Medium mesh with max ele-

Table 2.2: Material models used for the head structures other than white matter. The viscoelastic model is a one term Prony series defining the long-term and short-term shear moduli (μ_∞ & μ_0 respectively) and the decay constant β. The 1^{st}-Order Ogden model requires defining the shear modulus μ_1 and the dimensionless parameter α_1. The Mie-Gruneisen equation of state requires defining the reference density ρ_0, velocity constant c_0, two material constants s and Γ_0 and viscosity η.

Material	Model	Equation
Cerebellum	NeoHookean	$W = C_1(\overline{I}_1 - 3) + \frac{K}{2}(J-1)^2$
Cerebrum & Cerebellum	Viscoelastic	$\mu(t) = \mu_\infty + (\mu_0 - \mu_\infty)e^{-t\beta}$
Skull and Dura	Linear Elastic	E, ν
Bridging Veins	1^{st}-Order Ogden	$W = \frac{\mu_1}{\alpha_1}(\overline{\lambda_1}^{\alpha_1} + \overline{\lambda_2}^{\alpha_1} + \overline{\lambda_3}^{\alpha_1} - 3) + \frac{K}{2}(J-1)^2$
CSF	Mie-Gruneisen EOS	$p = \frac{\rho_0 c_0^2 \xi}{(1-s\xi)^2}\left(1 - \frac{\Gamma_0 \xi}{2}\right) + \Gamma_0 \rho_0 E_m, \xi = 1 - \frac{\rho_0}{\nu}$

ment size of 2 mm 3) Coarse mesh with max element size of 4 mm. For the medium and coarse meshes, elements were a combination of four and three node plane strain elements while the fine mesh is composed of only four node plane strain elements (by converting MRI voxels directly to elements). For each mesh, we examine the evolution of the area fraction of white matter that has been deformed to axonal strains(strain along the fiber direction) greater than some threshold. For all strain levels, we observe that the difference between the fine and medium meshes is smaller than the differ-

Table 2.3: Values for the material parameters used for the head structures other than white matter.

Material	Parameters
Cerebellum	$C_1 = 2432, K = 2.19GPa$
Cerebrum and Cerebellum	$\mu_\infty = 2C_1, \mu_0 = 10.6C_1$
Skull	$E = 8000MPa, \nu = 0.22$
Dura	$E = 31.5MPa, \nu = 0.45$
Bridging Veins	$\mu_1 = 25.63kPa, \alpha_1 = 11.12, K = 2.19GPa$
CSF	$\rho_0 = 1004kg/m^3, c_0 = 1489m/s, s = 1.79$
	$\Gamma_0 = 1.65, \eta = 0.001Pa.s$

ence between medium and coarse meshes. We have also examined convergence with respect to the locations of the largest damage. Given this convergence, we selected the medium mesh for the results presented here.

2.2.4 Validation of the Head Model for Non-Injurious Loading

Accurate modelling of the brain tissue is a key factor in determining the level of injury during traumatic events. We validate our head model by simulating the in-vivo brain rotational motion experiment of Knutsen et al. [4] Volunteers with no history of brain

injury used a device that induces a non-injurious rotation about the horizontal/axial plane of the head inside the MRI at Henry Jackson Foundation (HJF). The tagged MRI technique was then used to extract the 3D brain motions. The acceleration profile obtained from the experiment is applied to the axial slice of our model, and the resulting computed shear strains are compared to the experimental values.

Figure 2.4 shows the computed shear strains in the axial slice from our shear anisotropic model (equation 2.6) and from the HJF experiment at four times. These times are based on the experimental data, which were collected and processed every 18 milliseconds, beginning 9 milliseconds after the loading. The evolution of shear strain is captured by the model in the following senses. After 45 milliseconds, both the experiment and the model have the maximum shear strains reaching the middle of the brain, indicating consistent shear wave speed, and the locations of maximum and minimum strains are generally consistent between the simulation and the experiment.

To quantify this full field spatial validation for the model, we examine the statistical level of agreement using four different tests discussed by Ganpule et al. [146]: 1) Index of Agreement (d_r) 2) Coefficient of Efficiency (E_2) 3) Root Mean Squared Error (RMSE) to observations Standard deviation Ratio (RSR) and 4) Correlation Score (CS) (Table 2.4). For these statistical measures, we define the measured shear strains from the HJF experiment as the observed data O_i, and the results from our shear anisotropic model simulation as the predicted data P_i. Table 2.5 shows the results of all the statistical measures. For d_r (Willmott et al. [150]), E_2 (Legates and McCabe

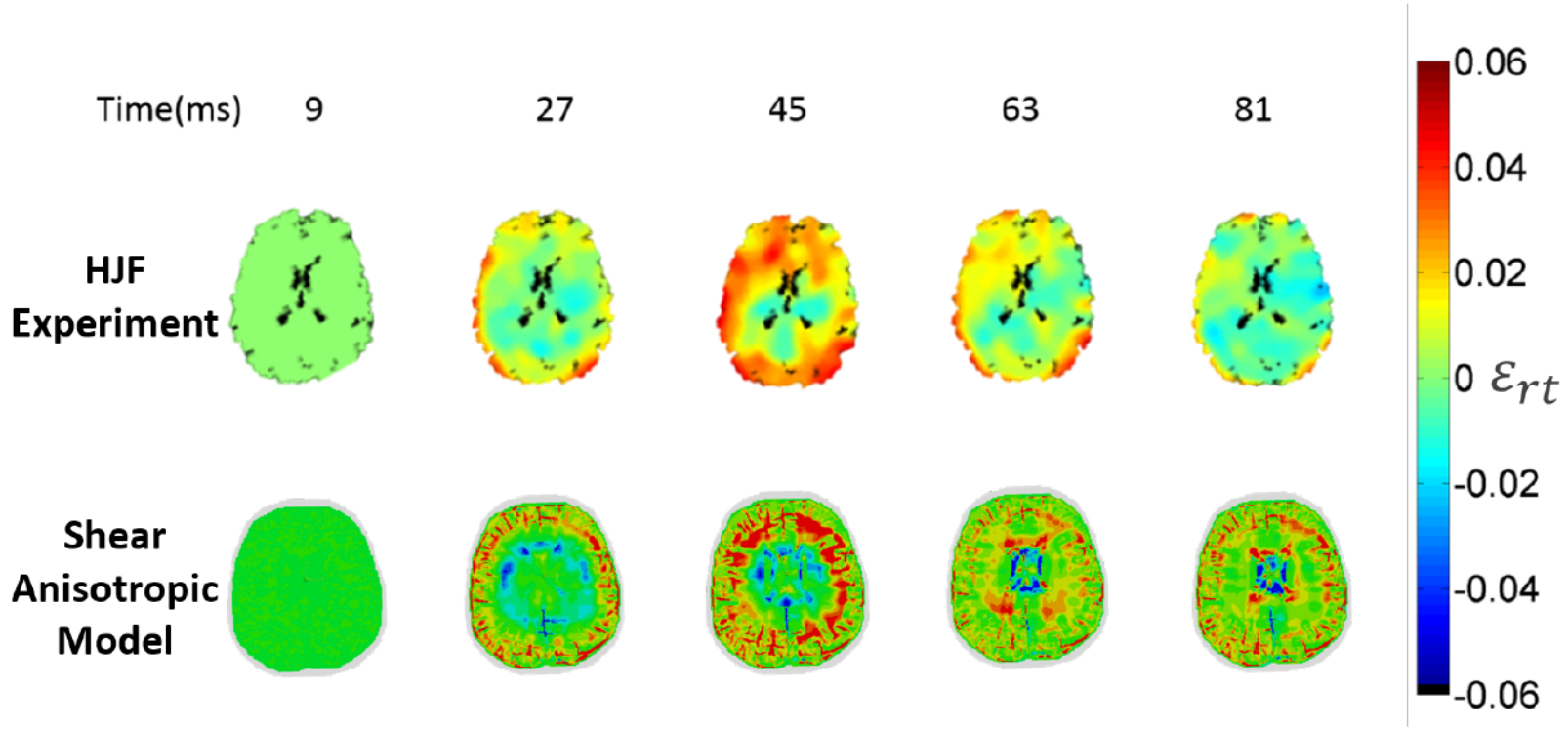

Figure 2.4: Comparison of the measured (HJF) and the computed (shear anisotropic model) shear strain distributions for the axial cross-section for every 18 ms beginning 9 ms after loading. Note that the simulation resolution is higher than the experimental resolution, leading to the appearance of more detailed strain distributions in the model results. The HJF results are derived from the Knutsen et al. [4] paper.

[151]) and RSR (Moriasi et al. [152]), the results are closer to the "better" end of the range (the upper end for d_r and E_2 and the lower end for RSR). Unfortunately, these particular metrics do not yet have a defined "level of goodness". For the CS results, the first two time frames (27 & 45 ms) are classified as fair agreement while the last two time frames (63 & 81 ms) are classified as marginal agreement (Kimpara et al. [153]). However, since our model is intended to be used for injurious loading which typically lasts between 15 and 36 ms, we find the overall statistical results to be acceptable.

The simulation, of course, has some advantages over the experiment: higher temporal and structural resolutions. While the experimental data is available only every 18 milliseconds (can be improved to 6 ms), the simulation data can be extracted with much finer resolution, e.g. every millisecond. Since injurious loading usually lasts from 15 to 30 milliseconds, the simulation produces a finer sense of the evolution of strains. Moreover, the experiment does not capture strains within the ventricles very well, which could affect the calculated strains in the surrounding tissues. We note also that Knutsen et al. [4] eliminated rigid body rotation only at the first part of the experiment (before the head stops completely by 3-4 degrees), but did not correct for rigid body motion afterwards. Other discrepancies between the experiment and the simulation could arise from structural differences between the subject heads in the experiment and the computation, or the large spacing of the experimental tag lines in comparison with simulation element size (8 mm as compared to 1-2 mm).

Table 2.4: Some measures of agreement between observations and predictions that can be used to assess TBI models. These measures are explained in Ganpule et al. [146].

Level of Agreement Test	Formula & Range	Agreement Rating
Index of Agreement (d_r)	$d_r = \begin{cases} 1 - \frac{\sum\|O_i - P_i\|}{2\sum\|O_i - \overline{O}\|} \text{ if } \sum\|O_i - P_i\| \leq 2\sum\|O_i - \overline{O}\| \\ \frac{\sum\|O_i - P_i\|}{2\sum\|O_i - \overline{O}\|} - 1 \text{ if } \sum\|O_i - P_i\| > 2\sum\|O_i - \overline{O}\| \end{cases}$ Range: -1 to 1	$\uparrow d_r \equiv$ better Agreement
Coefficient of Efficiency (E_2)	$E_2 = 1 - \frac{\sum\|O_i - P_i\|^2}{\sum\|O_i - \overline{O}\|^2}$ Range: -∞ to 1	$\uparrow E_2 \equiv$ better Agreement
RMSE to observations Standard deviation Ratio (RSR)	$\text{RSR} = \frac{\sqrt{(O_i - P_i)^2}}{\sqrt{\sum(O_i - \overline{O})^2}}$ Range 0 to ∞	$\downarrow$ RSR $\equiv$ better Agreement
Correlation Score (CS)	$CS = (1 - \|NISE\|) \times 100$ $NISE = 1 - \frac{2\sum O_i P_i}{\sum O_i^2 + \sum P_i^2}$ Range: 0 to 100	86-100 Excellent 65-86 Good 44-65 Fair 26-44 Marginal 0-26 Unacceptable

Table 2.5: The degree of agreement between the shear anisotropic model and the HJF experiment at four specific times, using the measures described in Table 2.4.

Time (ms)	27	45	63	81
d_r	0.42	0.23	0.28	0.29
E_2	-0.28	-0.98	-0.73	-0.66
RSR	1.13	1.40	1.31	1.29
CS	53.70	47.16	39.44	42.29

2.2.5 Injury Criteria

Defining an injury threshold for mTBI remains very difficult. No single injury threshold has yet been globally accepted. The difficulty arises because of the contribution of so many factors in any traumatic event, including but not limited to: location of impact (if any), direction of motion, rotational and translational accelerations, duration of the event, nature of the subject's neck, age and so forth. Accordingly multiple biomechanical thresholds have been used in the literature such as coup and contrecoup pressure (Ward et al. [114]), von Mises stress (Kleiven [120]), principal strains (Kleiven [120]), strain rate (King et al. [117]) and axonal strain (Wright et al. [3]). Since our new model is intended to better describe the white matter tissue, we selected the axonal strain injury threshold. Bain and Meaney [128] tested the optic nerves of guinea pigs and suggested an optimal threshold for axonal strain injury

of 18%. In our simulations, if the element strain along the axonal bundle (fiber) direction reaches or exceeds 18%, the element is considered damaged (and remains damaged even if the strain decreases subsequently).

2.2.6 An injurious Event

We now assign the known injury-causing loading conditions for each model/orientation (sagittal, coronal and axial). A reconstructed NHL incident previously used by Wright et al. [3] is examined, so as to directly compare model results. For each orientation, the corresponding linear and angular accelerations are applied in explicit FE simulations. Since the known loading curves (Wright et al. [3]) have a duration of only fifteen milliseconds and cutoff at non-zero values, we extend the curves so that the acceleration magnitudes are linearly decreased to zero over 5 milliseconds (and remain zero thereafter). However, the total simulation time is determined by the time needed for shear wave propagation inside the brain (Ganpule et al. [146]). The simulations are stopped when the damage of white matter ceases to evolve (change in damage of 0.25% or less for three consecutive milliseconds) in all loading cases.

2.3 Results

The shear anisotropy simulation results for the injury case are presented in Figure 2.5a in terms of the axonal strain (damage) distributions in the three cross-sections.

The degree of damage in each case is quite different from that previously obtained by Wright et al. [3] using the HGO model with only tension anisotropy.

The injury levels predicted by the two models are compared in Figure 2.5b. Red areas in the figure indicate elements of white matter in which the axonal strain reached or exceeded the injury threshold of 18% (any element that fulfills the injury criterion is considered damaged for the rest of the simulation). Overall, the damage predicted by the shear anisotropic model is clearly higher than the HGO model predictions.

Besides comparing damage location, the area of damage in each slice was also investigated. The percentage of damaged area Ω, is calculated as

$$\Omega = \frac{\int_{A_{WM}} A_{\varepsilon_{Axon} \geq 18\%} dA}{\int_{A_{WM}} A dA} \times 100 \tag{2.10}$$

where $A_{\varepsilon_{Axon} > 18\%}$ is area of white matter elements with axonal strain exceeding 18% and A_{WM} is the white matter area.

Using equation 2.10, the percent damage for each slice predicted by both models are calculated. In the axial slice, the predicted damage by the shear anisotropic model is almost three times the value predicted by the HGO model and the coronal and the sagittal slices also show more damage (compare values at end of simulations in Figure 2.6).

In addition to damage comparison, radial-circumferential shear strains are compared for the two models as shown in Figure 2.7. For all orientations, the overall shear strains are higher in the shear anisotropic model (top row of each sub-figure)

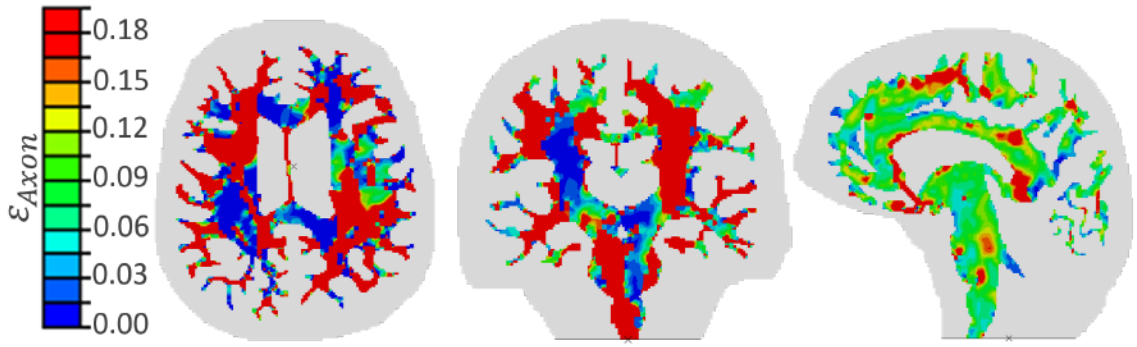

(a)

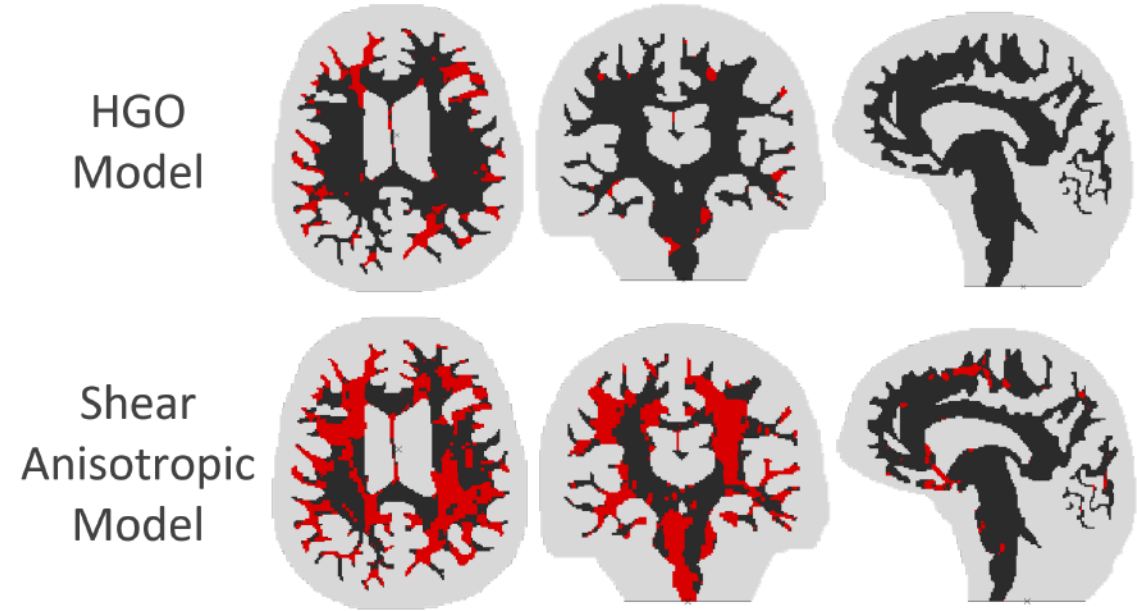

(b)

Figure 2.5: Simulation results for: a) The shear anisotropy of the injury case are presented in terms of the axonal strain (damage) distributions in the three cross-sections. Note: If axonal strain reached or exceeded the threshold of 18%, the element is labeled "damaged" for the remainder of the simulation. b) The comparison of the injury predictions of the previous HGO model and the current shear anisotropic model. Damaged regions ($\varepsilon_{Axon} \geq 18\%$) in each slice shown in red for the axial (left), coronal (middle) and sagittal (right) orientations.

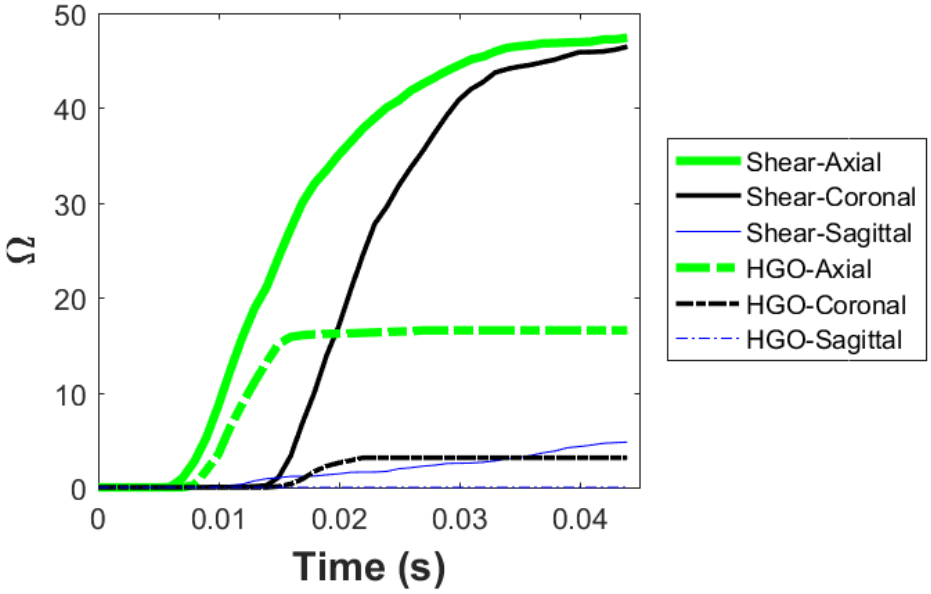

Figure 2.6: Time evolution of the total damage predicted by the HGO and shear anisotropic models. Solid lines represent the shear anisotropic model and dashed lines represent the HGO model. Note the higher amounts of damage predicted by the shear anisotropic model.

compared to the HGO shear strains (bottom row of each sub-figure). This observation is also mainly due to the difference in material properties between the shear anisotropic model and the HGO model.

2.4 Discussion

Significant differences in resultant damage between the two models are evident, as shown in Figure 2.5b. We note that most computational models show damage primarily at the boundaries between white and gray matters, due to the differences in stiffness between the two tissues. It is likely that some of the damage at these bound-

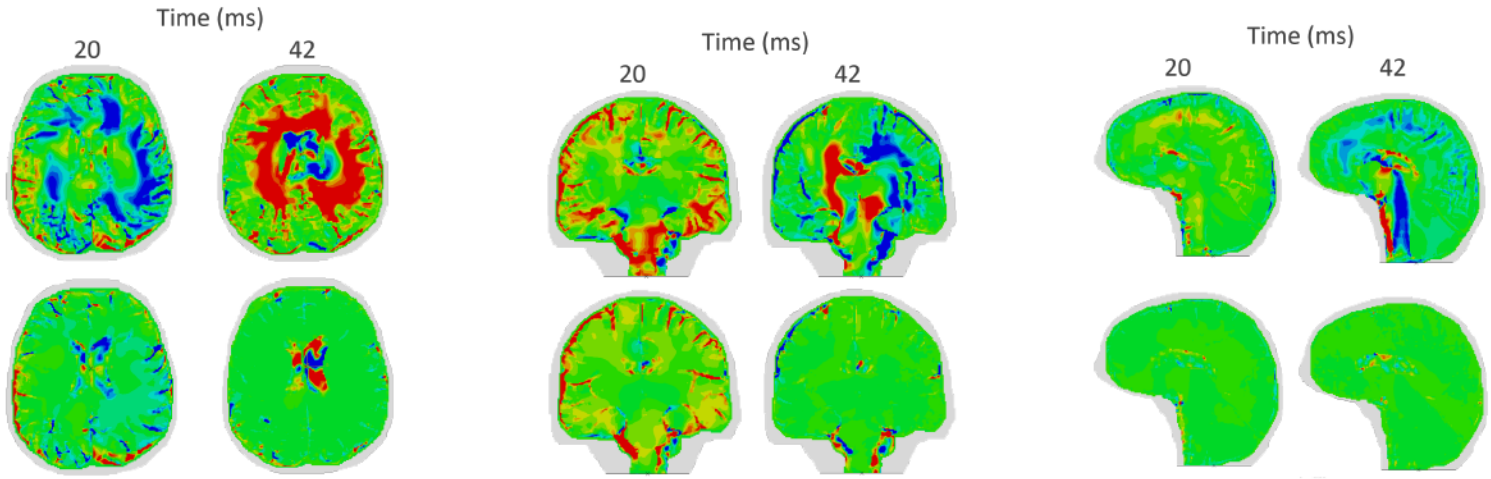

(a) **(b)** **(c)**

Figure 2.7: Comparisons of the evolution of the radial-circumferential shear strains predicted by the shear anisotropic model (top row) and the HGO model (bottom row) in the (a) Axial (b) Coronal and (c) Sagittal orientations. Note the shear strain concentrations in the brainstem predicted by the shear anisotropic model in the coronal and sagittal cases.

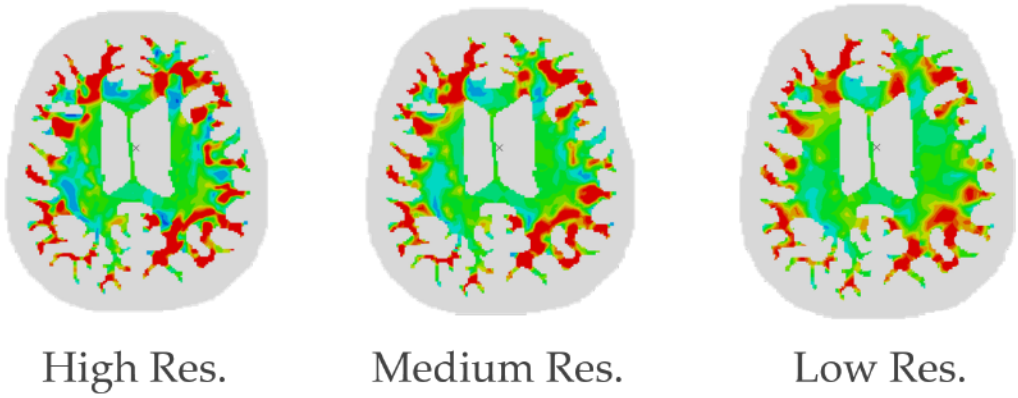

Figure 2.8: A comparison of the strains at the gray and white matter boundary for three mesh resolutions: high, mid and low (max. element size is 1, 2 and 5 mm respectively). The contours represents axonal strain, high axonal strains are represented by red (strains get higher as colors turn from orange to red). Clearly, high strains (and consequently damage) at the white and gray matter boundaries are to some degree due to mesh resolution.

aries is due to the mesh resolution as illustrated in Figure 2.8. The axonal strain map is shown for three different mesh resolutions: High, Medium and Low (Maximum element sizes are 1, 2 and 5mm, respectively). Clearly, the mesh resolution contributes to some degree to the injury found at the boundaries between white and gray matter. However, using the shear anisotropic model, some damage begins and remains in the deep white matter tissue, away from the boundaries between white and gray matters. This observation is supported by MRI studies on both animal and human injuries (Margulies and Thibault [123]) and the work of Smith and Meaney [154] in which diffuse axonal injury was characterized to be deeper in the white matter.

We find it useful to examine the damage history, i.e. the progress of damage throughout all time-frames of the simulation. Figure 2.6 shows the damage predicted by the shear anisotropic (solid lines) and the HGO (dashed lines) models as a function of time. The damage in the axial slice was not only higher than the other cases but also developed over a longer time. This is consistent with the loading conditions, and more specifically the angular acceleration in the z direction (applied to the axial slice) which has the maximum magnitude compared to the other two directions (applied to coronal & sagittal slices). Nevertheless, the damage predicted by the HGO model stops evolving as soon as the loading is stopped at 15ms while in the shear anisotropic model, the damage continued increasing until around 40ms. This may be because of the slower shear wave speed in the shear anisotropic model (0.5 m/s compared to 2.4 m/s in the HGO model).

A comparison of the radial-circumferential shear strains reveals differences between the two models in addition to the damage differences. For the coronal and the sagittal slices, the shear anisotropic model predicts higher levels of shear strains (Figures 2.7b and 2.7c) and damage in the brainstem. Such damage is not seen in the HGO simulation. Montgomery et al. [155] examined mild traumatic brain injury patients and found that the majority of the patients had abnormal brainstem function even after six weeks from the injury. Another study by Delano-Wood et al. [156] on veterans with chronic mild to moderate traumatic brain injury revealed a link between brainstem white matter integrity and the loss of consciousness after the

injury. Due to the inclusion of shear anisotropy in the shear anisotropic model, the brainstem experiences higher shear strains which translate to higher predicted damage compared to HGO predictions (Figure 2.5b). Note, however, that our simulations include only one family of fibers in each element.

Our simulations using our validated material model strongly suggest that considering shear anisotropy (e.g. through the addition of I_5) is important for computational predictions of mTBI. The injury predictions of the shear anisotropic model are significantly different than those predicted by the HGO model in terms of level of injury, location of injury and shear sensitivity. Although the injury threshold that we use is often used in the literature, we believe that more work is needed to correlate the symptoms presented by the injured subject with the predicted damage outcomes. Further, since the real fiber network of the brain has many crossing fibers, the shear anisotropic model needs to be improved to accommodate multiple families of fibers. Finally, we intend to extend this work for full 3D simulations of brain injury.

2.5 Summary of This Chapter

We have developed and validated a model for human white matter that captures both tension anisotropy and shear anisotropy using a finite element 2D head model with three representative slices. The white matter damage predicted by the shear anisotropic model is higher than that predicted by the HGO model (which does not account for shear anisotropy), and the damage history is more sensitive to the shear

wave propagation in the brain tissue. The shear anisotropic model predicts higher degrees of damage in the brainstem for at least one injurious event, perhaps correlated with the observed brainstem damage in some mTBI.

We conclude this chapter by emphasizing the importance of modelling shear anisotropy in white matter, since it changes the degree of predicted damage and the corresponding injury predictions are correlated with some mTBI observations in the literature.

The next chapter will discuss the second aspect of heterogeneity which is the vasculature network influence on the brain deformation under inertial loading.

Chapter 3

The Influence of the Arterial network effects on brain biomechanics under inertial loading*

3.1 Introduction

The second heterogeneity-causing component in the brain is the vasculature network. Since it is an anatomical/structural element, we first provide a quick review of the

*The work of this chapter was done in collaboration with the Image Analysis and Communications Lab (Jeffrey Glaister & Prof. Jerry Prince) and the Center for Neuroscience and Regenerative Medicine at the Henry M. Jackson Foundation for the Advancement of Military Medicine (Dr. Andrew Knutsen & Prof. Dzung Pham). Sections 3.4.1 and 3.4.2 were executed and written by Jeffrey Glaister in addition to the distance from nearest blood vessel calculations on the MRI segmented volume. Co-registration of the subject's structural MRI and the tagged MRI volumes for validation was performed by Dr. Andrew Knutsen .

anatomical evolution in mTBI modelling. When the first 3D studies of computational mTBI started, there were minimal anatomical details in the models. Structures included in these studies were typically the skull, the brain and the Cerebro-Spinal Fluid (CSF) (e.g. Hosey [157]). Either the falx, the tentorium or both were added to some 3D models a few years later (Dimasi et al. [158], Kang et al. [159], Takhounts et al. [160]). Although models with just these structures (Skull, brain, falx, tentorium and CSF) have low anatomical fidelity, some groups continue to use similar models when fast/low-cost computations are critical (Roberts et al. [78], Chatelin et al. [79]). Overtime, further anatomical details have been added to the models, including: meninges, dura, white matter, gray matter and bridging veins (Zhang et al. [77], Giordano and Kleiven [94], Colgan et al. [96], Zhang et al. [161]). However, very limited studies are directed towards the cerebral vasculature network (Omori et al. [162], Parnaik et al. [163], Zhang et al. [164], Ho and Kleiven [165]).

In 2000, Omori et al. [162] considered a simple half-circular model representing a sagittal plane. Applying a rotational pulse to two models, one with vasculature and one without, higher stresses were observed around the vasculature and in the subarachnoid space. Based on these results, the authors recommended the inclusion of vasculature in future models. Two years later, a related group performed a computational study considering a more anatomically correct sagittal slice model to study the effects of vasculature (Zhang et al. [164]). Linear acceleration and angular veloc-

ity pulses were applied to two models, one with and one without vasculature. Both principal and shear strains were compared, concluding again that it was important to include the vasculature network in computational models. In 2004, two physical, yet simple, head models were used by the same group to experimentally investigate the effects of vasculature (Parnaik et al. [163]). An aluminum cylinder was used to represent the skull, a silicone gel for the brain tissue and silicone tubes represented the blood vessels. The two models, which were a simple half cylinder representation of the coronal plane with and without vessels, were subjected to a number of different rotational scenarios using a two-segment pendulum setup. By tracking embedded markers in each model, displacements and principal strains were calculated and compared between the two physical models. The authors concluded that vasculature has a limited effect on the global brain deformation. The first computational 3D vasculature effects study was published a few years later in 2007 (Ho and Kleiven [165]). In that work, the vasculature network obtained from computed tomography angiography was added to an existing (Kleiven and von Holst [134], further validated in Kleiven [166]) finite element model. Two 3D head models, one with and one without vasculature, were subjected to two loading scenarios: translational and rotational accelerations. Comparing the principal strains (both average strains and strain patterns), led to a conclusion that vasculature effects are not significant. This result contradicted the earlier 2D computations. However, note that statistical measures were not used to quantify the strain distribution differences in any of the aforementioned studies. Such

measures are valuable for drawing conclusions from such complex and heterogeneous computations and experiments.

In this chapter we examine the influence of the vasculature network on brain biomechanics under non-injurious rotational acceleration loading by presenting two versions of a 3D head model, one with vasculature (specifically the arterial network) and one without. The arteries are specifically chosen due to two main reasons: they are stiffer than the veins and hence will create a higher degree of heterogeneity, and most importantly arteries can be segmented from a non-invasive Magnetic Resonance Angiography (MRA) known as the Time-Of-Flight (TOF).

3.2 Problem Statement

We begin with the following hypothesis:

Including the arterial network in computational head models of mTBI significantly alters brain deformations, and consequently injury predictions, under inertial loading.

To test this hypothesis, two computational models will be built, one with vasculature and one without. Material parameters needed to model arteries will be fitted to a published experimental study. All other material models and parameters will be acquired from previous computational models of mTBI in the literature. Hence, the two models will be identical in material models and parameters except for the

addition of the arterial network. The model with vasculature network will be validated against in-vivo human brain deformation experiment in the literature. Once the model is validated, a simplified version of the model (in terms of material models) will be used to test the hypothesis by comparing largest principal strains and shear strains between two models, one with and one without vasculature.

3.3 Inertial Loading Test Case

The inertial loading that we selected to test the hypothesis is a non-injurious angular acceleration from Chan et al. [10]. A healthy subject with no prior history of head injury is placed in a device inside the Magnetic Resonance Imaging (MRI) scanner what was developed in a previous study of the same group (Knutsen et al. [4]). The device has a counter weight that will rotate the head axially once the subject release a lock. The position of the head is recorded using an MRI-compatible optical position sensor and the acceleration is calculated by differentiating the position history twice. Both the position and the acceleration for the subject we will use in our computational study are shown in figure 3.1, and are applied directly to the skull in the computations. We provide the acceleration profile to give a sense of how the loading differs from injurious scenarios in acceleration profile and magnitude.

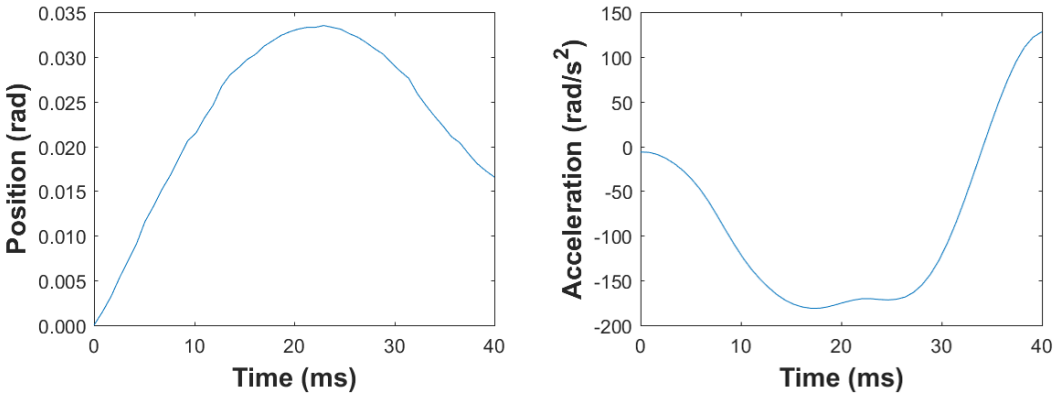

Figure 3.1: Position (left) and angular acceleration (right) histories for a healthy subject in-vivo experiment from Chan et al. [10].

3.4 Building the 3D head models

We build two computational head models based on Magnetic Resonance Image (MRI) data from a healthy subject. The MRI is first segmented to produce the 3D head model without vasculature. Then, Time-Of-Flight (TOF) imaging of the same subject is segmented to obtain the arterial network structure, which is then added to the MRI segmentation creating the second model with vasculature. The Material Point Method is used to transfer the segmented heads into two computational models (with and without vasculature). Finally, material models and properties will be assigned.

3.4.1 MRI segmentation

The MRI analysis pipeline starts with inhomogeneity correction (Tustison et al. [167]) of the subject's T1-w and T2-w MRI. The T1-w MRI is rigidly registered to the Montreal Neurological Institute-152 atlas resampled to 0.8mm isotropic voxels and the T2-w MRI is transformed to this space. The T1-w and T2-w MRI are used to estimate a brain mask (Roy et al. [168]) for skull stripping. To obtain an initial multi-atlas segmentation, 30 Neuromorphometrics atlases (http://www.neuromorphometrics.com/) are deformably registered to the subject's T1-w MRI using the ANTs software package (Avants et al. [169]). The atlases contain T1-w MRIs and label maps with 62 cortical labels per hemisphere. The initial segmentation is generated by fusing the 30 deformed label maps using joint label fusion (Wang et al. [170]). The multi-atlas segmentation is refined to be consistent with reconstructed inner and outer cortical surfaces (Huo et al. [171]).

Additional structure-specific processing pipelines are applied to segment the falx cerebri and tentorium cerebelli. The falx and tentorium are segmented using the refined multi-atlas segmentation and the subject's Susceptibility Weighted MR Image (SWI) (Glaister et al. [172]). Briefly, the cortical labels produced by the refined multi-atlas segmentation are expanded using fast marching into the longitudinal and transverse fissures (Glaister et al. [173]). The labels are expanded up to 5 mm or until they reach another label. The set of voxels where gray matter labels from

the left and right hemispheres meet in the longitudinal fissure define the initial falx. Likewise, the set of voxels where cerebellum and cerebrum gray matter labels meet in the tranverse fissure define the tentorium. To refine the initial falx, a set of five atlases with SWI and a manually-segmented falx are deformably registered to the subject's SWI (Glaister et al. [172]). The boundary of the refined falx is determined by applying the continuous-STAPLE fusion algorithm (Commowick and Warfield [174]) to corresponding boundary points.

3.4.2 TOF segmentation

Brain blood vessels are segmented from TOF Magnetic Resonance Angiography (MRA) images. The TOF MRA is corrected for inhomogeneities (Tustison et al. [167]) and rigidly registered to the T1-w MRI. The TOF MRA voxel intensities are represented by a mixture model consisting of a Rayleigh distribution and three Gaussian distributions (Hassouna et al. [175]). The lowest intensities correspond to cerebrospinal fluid, bone, and background air and are represented by a Rayleigh distribution. Gray and white matter brain tissues are represented by two Gaussian distributions and the highest intensities, which correspond to blood vessels, are represented by a single Gaussian distribution. The distribution parameters are estimated using an Expectation-Maximization algorithm (Hassouna et al. [175]). A binary map of blood vessel voxels is produced by setting voxels that belong to the blood vessel distribution according to a maximum a posteriori classification to 1 and other voxels to 0. The final blood

vessel segmentation is generated by taking the largest connected component in the binary map to remove small objects.

Note the TOF segmentation provides the arterial network only. Segmenting the venous network requires another modality of medical imaging (x-ray based angiography) which is invasive. Hence, the venous network is not resolved in our model.

3.4.3 MPM implementation

The most commonly used computational method in TBI studies is the Finite Element Method (FEM), used, e.g., in Chapter 2. However, we use the Material Point Method (MPM) so as to overcome FEM complications like mesh entanglement and difficulties in meshing complex structures since MPM is a meshless method. Hence, segmented MRI structures can be directly converted to materials points for the MPM implementation which we will introduce in the next paragraph.

The first introduction of a meshless particle method was by Harlow [176]. He established the Particle In Cell (PIC) computational technique for fluid dynamics in which fluid particles flow through a fixed grid. A few decades later, in 1994-1996, the PIC method was extended for solid mechanics and called the Material Point Method (MPM) (Sulsky et al. [177], Sulsky and Schreyer [178], Sulsky et al. [179]). The solution combines advantages of Eulerian (Fixed grid = No mesh distortion) and Lagrangian (Tracked points in space = Complete deformation history) solution methods together. First, material points are set in space with a background grid. State

variables are transformed from the material points to the grid nodes using an interpolation function (similar to the shape functions concept in FEM). The incremental solution is calculated at the grid and then interpolated back to the material points updating their current state (location, stresses, strains, ... etc). Then, the background grid is reset and the whole process is repeated again until the required loading or simulation time. Note that information is never stored on the grid and deformation history is carried by the material points only. A comparison between MPM and FEM in problem setup and solution steps is shown in Table 3.1. Computationally, FEM is more expensive in terms of preprocessing (creating the mesh) specially for complex structures while MPM is more expensive in the solution procedure due to the need for double interpolation at each time step.

A Generalized Interpolation Material Point (GIMP) scheme was introduced by Bardenhagen and Kober [180] to account for the finite spatial extent occupied by each particle (instead of the old lumped mass approach). There are several interpolation functions derived for the GIMP scheme of MPM such as: undeformed GIMP (uGIMP), convected particle GIMP (cpGIMP) and Convected Particle Domain Integration (CPDI) (Sadeghirad et al. [181]). uGIMP is very efficient for small deformations but might suffer an unphysical material fracture (i.e.: numerical fracture) if the strains are too large (changes to the initial particle domain are not allowed in uGIMP). The use of cpGIMP will solve the numerical fracture problem, but this interpolation does not capture shear deformations (allows particle stretching only). To overcome

Table 3.1: A comparison in problem setup and solution procedures between Finite Element Method (FEM) and Material Point Method (MPM).

	FEM	MPM	Remarks
Structure Setup:	1. Preprocess: Mesh (→ create nodes). 2. Gauss Points defined based on chosen element type.	1. No Meshing Required. 2. Material points assigned and background grid defined.	Setup is less expensive using MPM.
Solution Steps:	1. Solve spatial gradients at Gauss points. 2. Use shape functions to interpolate solution to mesh nodes. 3. Repeat steps till desired loading time.	1. Interpolate state variables to grid nodes. 2. Solve spatial gradients on grid nodes. 3. Interpolate solution back to material points. 4. Reset grid and repeat steps till desired loading time.	Solution is less expensive using FEM.

both obstacles (large strains and shear deformations), CPDI is used which converts the rectangular domain of particles to parallelogram allowing for shape changes.

In our model, to reduce computational cost, the segmented structure with an isotropic resolution of 0.8 mm is reduced down to an isotropic resolution of 1.6 mm (Figure 3.2). The reduction was performed by assigning an inital grid with cell-size of 1.6 mm with, typically, two particles (or material points) in each direction per cell. The points in each cell are then sorted based on their structure label. The structure with the highest number of points in that cell will be selected to represent cell with one point in the center and the original material points are deleted. However, if that cell contains vasculature points, it will be directly converted to single vasculature point in the center of the cell. The process is repeated over the whole head space until the whole structure is reduced to 1.6mm resolution. A new background grid, on which the governing equations will be solved, is then setup with a cubic cell size of 3.2 mm and two material points in each direction totaling 436,826 points for the whole head (Note in Ho and Kleiven [165] the resolution was not reported but the total number of elements based on their mesh density study in Kleiven and von Holst [134] was 7,500 elements. To have a comparative measure between our resolution and that in Ho and Kleiven [165], typically each cell in our model has 8 particles and hence our model has about 54,600 cells or elements). The spatial gradients on the grid are calculated using the assigned interpolation function. To eliminated instabilities from

large and/or shear deformations, we use the CPDI interpolation function as suggested in the literature (Sadeghirad et al. [181]).

Uintah Computational Framework[†] is used for our MPM implementation which allows for easy parallel computing and has been validated against well controlled experiment using a phantom head (Ganpule et al. [182]) and recently used for soft tissues in the literature (Ionescu et al. [183], Ganpule et al. [184]). The setup requires defining materials as points in space with the corresponding models and parameters, an interpolation scheme, a displacement loading condition and the computational global space on which the solution will be carried out. If a material point leaves this global domain during the simulation, due to large deformations for example, the point will not be tracked and the information of that point will be lost. This setup introduces challenges in simulating large head displacements especially in the translational direction.

To summarize the MPM implementation, two models one with and one without vasculature are built with material point spacing of 1.6mm and a cubic grid cell-size of 3.2mm. Resolved arteries have an average vessel size of around 2.5 mm. The effect of unresolved arteries is assumed to be incorporated in the brain tissue properties. Finally, the CPDI interpolation scheme is chosen to account for large and shear deformations which are expected in brain deformations under inertial loading (Ganpule et al. [184]). (For more information on the MPM implementation, refer to

[†] http://uintah.utah.edu/

Appendix A)

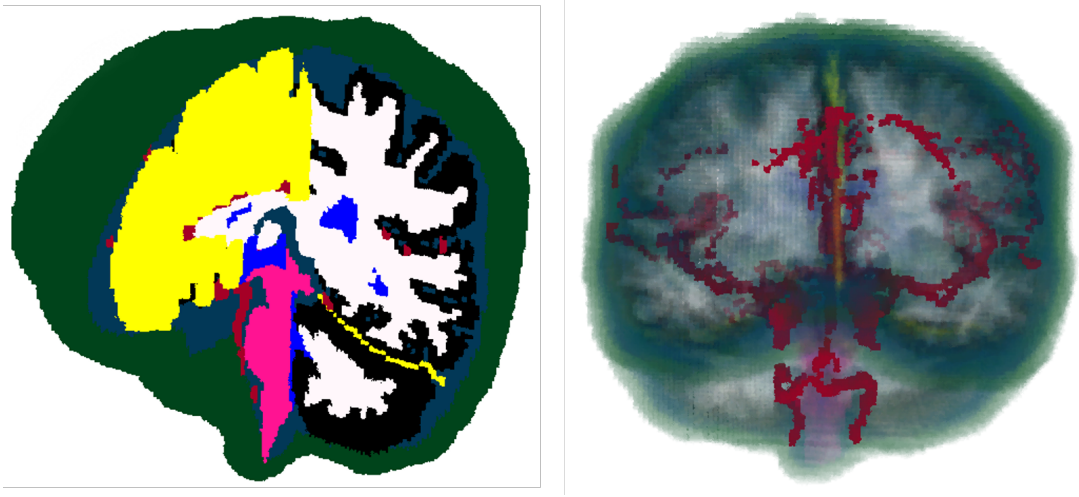

Figure 3.2: Left: A cut through the model with blood vessels showing all segmented structures (Skull, CSF, ventricles, falx, tentorium, white matter, gray matter, brainstem and blood vessels). Right: The whole model making all structures transparent except the blood vessels. For MPM implementation, a fixed background grid is overlaid on the model with cubic cell size of 3.2mm and two material points in each direction (material point spacing = 1.6mm). Note: The vasculature network is mainly connected with some isolated islands of arterial vessels.

3.4.4 Material Models & Properties

There are six distinct materials in our head models: Skull, CSF, falx, tentorium, gray matter, white matter and blood vessels. Since the purpose of this study is to evaluate the effects of adding the vasculature network on the brain response, we start by selecting a material model for the vasculature, with the parameters obtained from

published experiments on cerebral vasculature.

Although mechanical properties of the brain vessels were studied in the 1970s (e.g.: Hayashi et al. [185]), the first comprehensive experimental study was performed by Monson et al. [11] in 2003. Fresh cerebral vessels were extracted from humans undergoing brain surgery for diseases that were believed to not affect the cerebral vasculature. Both arteries and veins were preconditioned and tested within 4-6 hrs from extraction. The stress-stretch curves generated for all the samples presented in that study are shown in figure 3.3. We focus on the behavior of arteries for this study. Figure 3.3 shows a clear variability in the arterial behavior, perhaps due to the non-homogeneous structure of these biological tissues, age of the donor and size of the vessel. We also observe that the behavior is non-linear with small slope at the beginning of the curve (most commonly known as the toe-region) and a much higher slope at larger stretches. The toe-region has multiple sizes across the tested arterial samples. Additionally, note that the behavior of arteries does not show strain-rate dependency since the dynamic and quasi-static curves have similar slopes.

Given the non-linearity, we select the Mooney-Rivlin strain energy function to represent the behavior of cerebral arteries. The Mooney-Rivlin strain energy density function is

$$W_{MR} = \frac{\mu_1}{2}(I_1 - 3) - \frac{\mu_2}{2}(I_2 - 3). \tag{3.1}$$

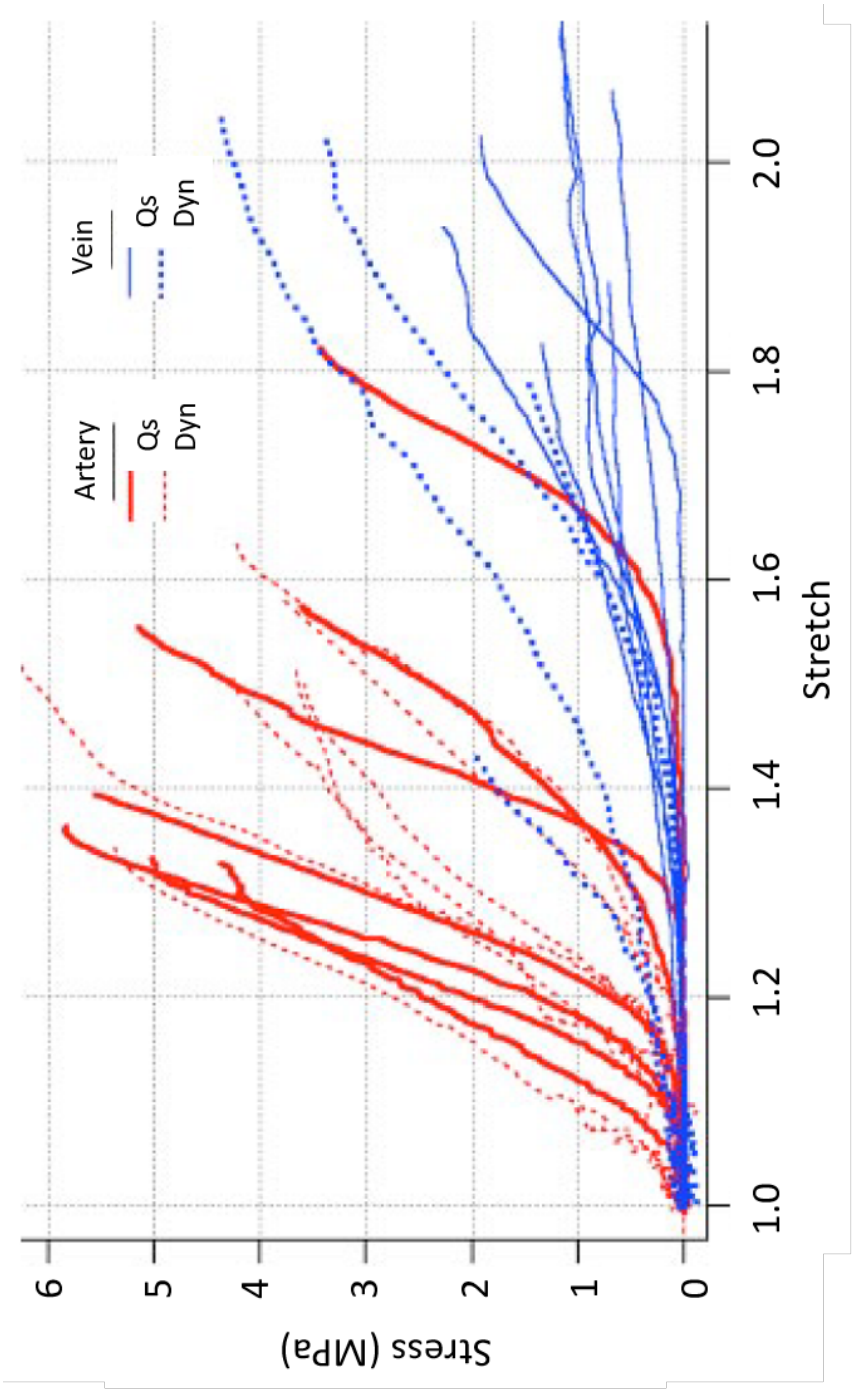

Figure 3.3: The stress-strain behavior of fresh human cerebral arteries and veins. A comprehensive experimental study by Monson et al. [11].

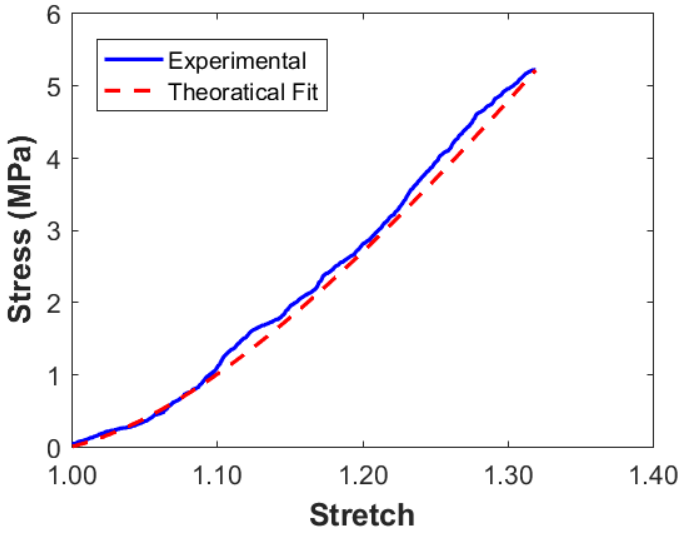

Figure 3.4: The fitting result for the blood vessels in our head model to an artery sample behavior from Monson et al. [11]. The Mooney-Rivlin parameters are μ_1= 25 MPa and μ_2= 20 MPa.

The parameters μ_1 and μ_2 are fitted to one of the artery samples in Monson et al. [11] with the fit shown in figure 3.4. With this fit, μ_1 and μ_2 are 25 and 20 MPa, respectively, and the effective shear modulus is 5 MPa calculated following Holzapfel [142] ($\mu_{Effective} = \mu_1 - \mu_2$).

The skull is assumed to be modeled as a linear elastic material with Young's modulus of 6.5 GPa and Poisson's ratio of 0.2 as is commonly used in computational models of mTBI (Zhang et al. [77], Chen and Ostoja-Starzewski [186], Willinger et al. [187]). Linear elastic behavior is also assumed for the falx and tentorium with Young's modulus of 31.5 MPa and Poisson's ratio of 0.45 (Miller et al. [188]). Finally the CSF (and similarly the ventricles since they are filled with CSF) is modeled using the Tait

equation of state with density ρ=1004 kg/m^3, bulk modulus K=2.19 GPa and γ=7.15 (Ganpule et al. [184], Cole and Weller [189]).

The gray matter is modeled as a Neo-Hookean hyperelastic material with a three-term Prony series to incorporate the strain-rate dependency of the shear modulus as follows

$$G(t) = G_\infty + G_0 \sum_{i=1}^{N} g_i e^{\frac{-t}{\tau_i}} \text{ or } G(t) = G_0 \left[1 - \sum_{i=1}^{N} g_i \left(1 - e^{\frac{-t}{\tau_i}}\right)\right] \tag{3.2}$$

where N is the number of Prony series terms, $G(t)$ is the shear modulus, G_0 is the instantaneous shear modulus, G_∞ is the long-term shear modulus, g_i is the Prony series constant and τ_i is the relaxation time. The following parameters are used for the gray matter: G_0=2750 Pa, G_∞=385 Pa, g_1=0.625, g_2=0.055, g_3=0.182, τ_1=2, τ_2=11 and τ_3=47.5 seconds (Ganpule et al. [184] and Lee et al. [190]). We also note that relaxation times are too long for the application (relaxation times in seconds vs. tens or hundred micro-second application) and further tests with much shorter relaxation times are needed for future implementation.

Since some efforts in the literature extract viscoelastic properties in the frequency domain (e.g. Magnetic Resonance Elastography (MRE) studies), the Prony series equation can be converted to the frequency (ω) domain by applying Fourier Transform

$$F(\omega) = \int_{-\infty}^{\infty} f(t) e^{-i\omega} dt \leftrightarrow f(t) = \frac{1}{2\pi} \int_{-\infty}^{\infty} F(\omega) e^{i\omega} d\omega \tag{3.3}$$

Applying Fourier transform on equation 3.2, the resulting storage and loss moduli

(G' and G'', respectively) are

$$G'(\omega) = G_0\left[1 - \sum_{i=1}^{N} g_i\right] + G_0 \sum_{i=1}^{N} g_i \frac{\tau_i^2\omega^2}{1+\tau_i^2\omega^2} \tag{3.4}$$

and

$$G''(\omega) = G_0 \sum_{i=1}^{N} g_i \frac{\tau_i\omega}{1+\tau_i^2\omega^2} \tag{3.5}$$

where the storage modulus is the real part of the transformed function and the loss modulus is the imaginary part[‡]. For example at 0 Hz, the storage modulus is 279.5 Pa which is comparable to low strain rate experiments shear modulus (e.g. Velardi et al. [1]). A direct comparison between MRE data and shear modulus obtained using standard mechanical tests is not straight forward due to the small displacements and frequencies applied in the MRE experiments and the missing direct link between strain rates and frequencies.

The white matter is modeled as an anisotropic hyperelastic material using the HGO model as described in equation 2.9 with a one term viscoelastic Prony series for the shear modulus to account for tissue viscoelasticity. The material parameters required for the HGO viscoelastic model are: instantaneous shear modulus G_0=1520 Pa, long-term shear modulus G_∞=286 Pa, stress constant k_1=121 kPa, stress factor k_2=0.0001 and time constant τ=2 seconds (adapted from Velardi et al. [1], Ganpule et al. [184] and Lee et al. [190]). Another parameter is required for the HGO model and that is the fiber dispersion κ. This parameter is dependent on the fractional anisotropy

[‡]The conversion from time domain to frequency domain is adapted from unpublished work by Dr. Yuan-Chiao Lu.

(FA) of white matter which is obtained from the Diffuse Tensor Image (DTI) (for the same subject we used to build the head structure (from Chan et al. [10])). The degree to which the axonal fiber bundles are aligned determine the value for FA which can range from 0 (no preferred alignment ⇒ isotropic) to 1 (perfectly aligned fibers ⇒ transversely anisotropic). The relationship between the fiber dispersion and FA is as follows (derived in Wright et al. [3]):

$$\kappa = \frac{1}{2}\frac{-6 + 4FA^2 + 2\sqrt{3FA^2 - 2FA^4}}{-9 + 6FA^2} \tag{3.6}$$

If we substitute the lower and upper limits for FA in equation 3.6, κ will have the range 0 to 1/3 where 0 corresponds to perfectly aligned fibers (i.e. transversely anisotropic) and 1/3 corresponds to randomly oriented fibers (i.e. isotropic). The remaining component to complete the definition of white mater is the initial fiber direction ($\mathbf{a_0}$) for each material point. This final piece of information is also obtained from the subject's DTI by extracting the first principal direction for each white matter voxel. Finally, the bulk moduli for the cerebrum and the cerebellum are assumed to be 1.46 and 1.19 GPa, respectively (Ganpule et al. [184]).

3.5 Validation

Before applying any inertial loading, we first validate the 3D model with vasculature against live human brain deformation experiment (Knutsen et al. [4]). The same

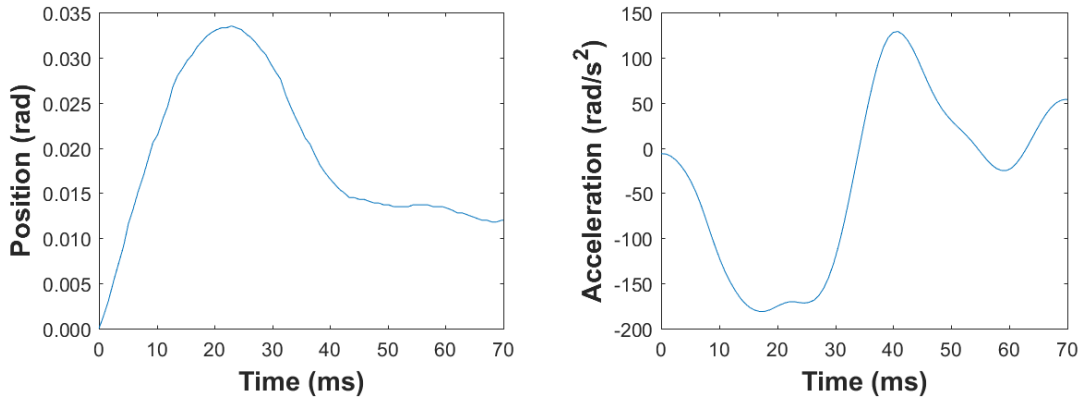

Figure 3.5: Loading conditions used for the validation of our 3D head model from Knutsen et al. [4] experiment. An axial rotation of the head (a) is produced by a counter-weight fixed to the special MRI device which induces a non-injurious angular acceleration (b).

healthy subject we used to build our 3D model is placed in a device that induces rotational acceleration around the superior-inferior axis (axial rotation). The angular position of the head is recorded (Figure 3.5a), and the angular acceleration is then calculated which has a maximum value of around 180 rad/s^2 (Figure 3.5b).

During the loading, tagged MRI technique (Axel and Dougherty [191] and Bayly et al. [192]) is used to capture the brain deformation in twelve different axial planes, spaced around 1 cm away from each other, covering the brain from the top until most of the cerebellum. The tag are lines overlaid on each axial plane with tag-line spacing of 8 mm. The images are then processed using Harmonic Phase (HARP) method (Osman et al. [193]) to calculate the 2D principal strain in each slice. Since

the loading is planar (rotation is applied only axially), there is very little motion out of the axial plane making the 2D calculations reasonable in this particular case.

Co-registering the full head segmentation with the tagged MRI volume was performed such that we can make a point-to-point comparison between the two. Figure 3.6a shows the co-registered volume, where it is clear that the cerebellum gray matter is not fully accounted for in the validation structure due to the setup of tagged MRI experiment (Knutsen et al. [4]). The loading condition from the experiment is applied to this model using Uintah framework as explained in Section 3.4.3. The maximum principal strain is extracted from the simulation results for every material point and compared to the corresponding value in the experiment.

We used the statistical agreement measures explained in section 2.2.4 (Table 2.4) to quantify the level of agreement between the model and the experiment. The maximum principal strain in the experiment is considered as the observed data (O_i) and the maximum principal strain in the simulation as the predicted data (P_i). Since the experimental strain calculations were performed on each slice in 2D, we apply the statistical agreement formulas on each slice separately (Figure 3.6b shows a sagittal cut of the model with the tagged slices labeled in red).

Note that the experimental temporal resolution (times at which strains are calculated) is 18 ms starting from time 9 ms as the initial configuration (deformation of the tag lines was not observed until 9 ms). Given this, we compare the largest maximum principal strains from our simulation to those calculated in the experiment for the

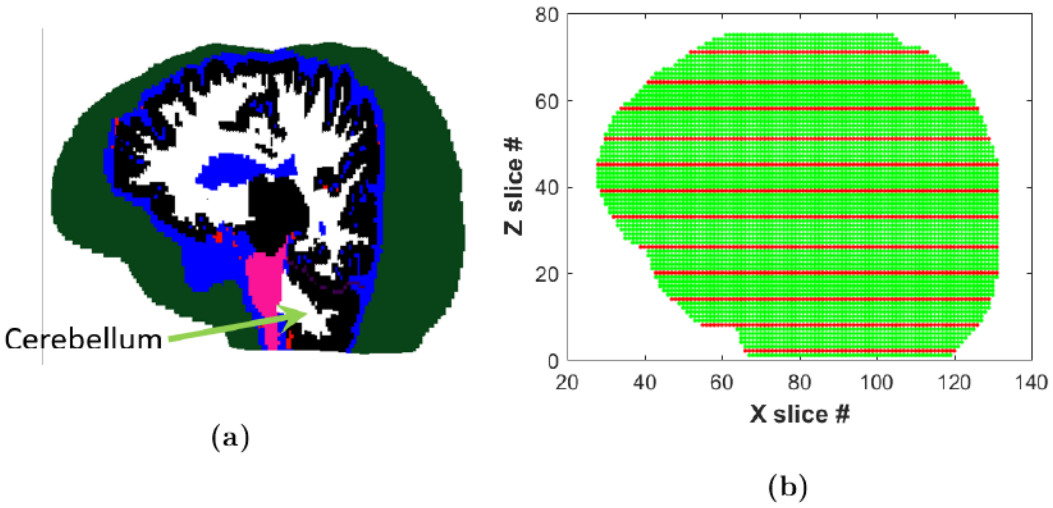

Figure 3.6: a) The co-registered model used for the validation with in-vivo brain deformation experiment of Knutsen et al. [4] (The circle highlights the cerebellum which is not fully accounted for). b) A side view (sagittal) of the model with the experimental tagged MRI slices in red.

first three time points (the times of calculated strains in the experimental work): 27, 45 and 63 ms. Table 3.2 shows average, maximum and minimum results for the four agreement measures.

It is worth mentioning that the minimum values of the Correlation Score (CS) are related to one or more of the lowest three slices in the z-direction (slices #: 2, 8 and 14). This is mainly due to the abrupt cut of the model at the base of the head. Once we steer away from the lower three slices, CS values are either fair or good. Considering the CS values and that we will use the full head model (smooth complete cerebellum and brainstem as shown in Figure 3.2), we find our validation

results acceptable. Further, the difference in the spatial (tag lines spacing of 8mm in the experiment vs grid cell size of 3.2mm in the model) and temporal (strains calculated every 18ms in the experiment vs every 1ms in the simulation) resolutions between the experiment and the simulated model could have contributed to the level of agreement between the two.

3.6 Impact of the Arterial Network

Now that the model is validated, we will use the model to investigate the hypothesis in Section 3.2. We begin with the simplest case, where the brain tissue will be modeled as an isotropic material to reduce the level of complexity in our study. Largest Principal Strain and shear strains will be extracted since both were used as an injury predictor (section 1.4.3). Using this simplified approach, the results of the two models, with and without vasculature, will now be compared to evaluate the hypothesis.

3.6.1 Isotropic Limit

The white and gray matters are modeled as Neo-Hookean hyperelastic materials with viscoelastic shear modulus represented by a one-term Prony series (Equation 3.2). The material parameters are chosen to be consistent with computational head models in the literature (Zhang et al. [77], Taylor and Ford [136]), and are shown in table 3.3. Note that with these material parameters the difference between the arteries effective

Table 3.2: Statistical agreement results between maximum principal strains of the 3D head model with vasculature and the experimental strains of Knutsen et al. [4]. Colors for the Correlation Score (CS) indicate rating: Good, Fair, Marginal and Unacceptable. Note that the minimum values for CS are occurring at the one of the lowest three slices, mainly due to the abrupt cut at the base of the model.

	Time (ms)	27	45	63
d_r	Average	0.379	0.291	0.601
	Max	1.11	0.433	2.98
	Min	0.0166	0.056	0.024
E_2	Average	-5.29	-1.66	-10.9
	Max	-0.981	-0.612	-0.747
	Min	-14.1	-6.71	-57
RSR	Average	2.37	1.58	2.96
	Max	3.89	2.78	7.62
	Min	1.41	1.27	1.32
CS	Average	58	63.4	53.1
	Max	76.2	77.3	72.2
	Min	42.8	32.4	25.8

Table 3.3: Material parameters for the white and gray matters consistent with computational head models in the literature. A hyper-elastic Neo-Hookean model is used with a single term prony series to account for viscoelasticity.

Parameter	White matter	Gray matter
G_∞ (kPa)	7.8	6.4
G_0 (kPa)	41	34
$(1/\tau = \beta)$ (s^{-1})	700	700

shear modulus and the brain tissue shear modulus is three orders of magnitude (5MPa to 7kPa, respectively). Such difference strengthen the hypothesis of section 3.2.

3.6.2 Results

Two simulations are performed with the identical loading conditions, boundary conditions, materials and material properties except for vasculature (in other words: one simulation with arteries and one simulation without arteries). The results of the two simulations are compared to each other in three ways: average strains, maximum strains and strain distributions. Two strain measures are used: the Largest Principal Strain (LPS) and the radial-circumferential shear strain (E_{rt}). Both measures were used as injury predictors (as explained in section 1.4.3.2) and have been used in one or more of the previous vasculature effects studies in the literature (Omori et al.

[162], Parnaik et al. [163], Zhang et al. [164], Ho and Kleiven [165]). Additionally, the relation between LPS and distance from the nearest blood vessels will examined.

3.6.2.1 Average Strain

Average LPS and E_{rt} over the whole white matter volume is plotted at every 5ms (in a non-injurious scenario we do not expect rapid changes in the deformation, hence we do not extract averages at every ms) as shown in figure 3.7. The average is calculated as

$$\text{Average LPS} = \frac{\sum_{i=1}^{N} \text{LPS}_i}{N} \tag{3.7}$$

where N is the number of white matter material points.

Overall, the simulation without blood vessels has higher average strains which is expected since the addition of vessels adds to the overall stiffness of the brain and hence leads to lower average strains. The onset of divergence in the average strain between the two models (with and without vasculature) starts at 20ms, perhaps because at this time, the loading condition is transitioning from acceleration to deceleration motion (Figure 3.1). To better understand this observation, further investigation using multiple loading curves that differ in the time to transition phase, for example, is needed.

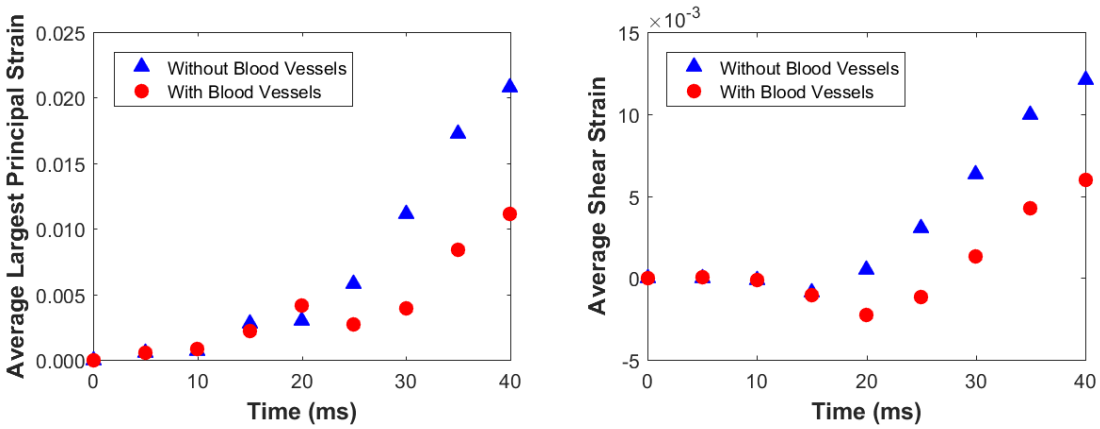

Figure 3.7: a) Average LPS and b) E_{rt} strains plotted at every 5ms for the simulations with and without blood vessels. Overall average strains are higher in the simulation without blood vessels due to lower overall stiffness.

3.6.2.2 Maximum Strain

Figure 3.8 shows the maximum values of LPS and E_{rt} at every 5ms for both simulations. In general, the simulation without blood vessels shows higher maximum LPS strains after 20 ms. Maximum strain difference between the two simulations is about 5% in LPS (ΔLPS_{max}) and 4.3% in E_{rt} ($\Delta E_{rt_{max}}$). Keeping in mind that the highest strains are about 11% for LPS and 9.5% for E_{rt} both in the simulation without blood vessels, we found that the differences (ΔLPS_{max} and $\Delta E_{rt_{max}}$) are considered significant (average strains of the simulation with blood vessels are about half of those calculated in the simulation without blood vessels). Note that maximum strains in Figure 3.8 shows the same behavior as average strains (Figure 3.7) in terms

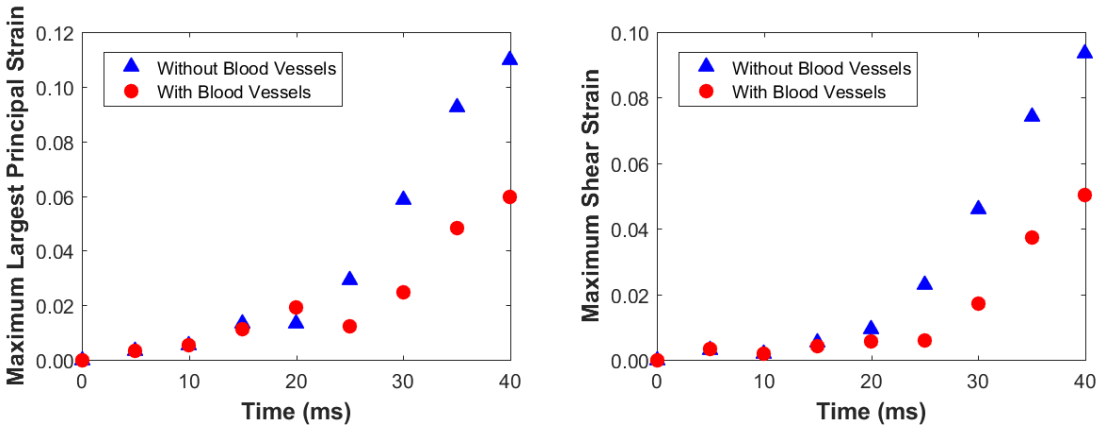

(a) **(b)**

Figure 3.8: a) Maximum LPS (left) and b) E_{rt} strains plotted at every 5ms for the simulations with and without blood vessels. Differences between the two simulations exist, with higher overall maxima in the simulations without blood vessels due to lower overall stiffness.

of divergence onset between the two models and that the strains in the model with vasculature are about half those in the model without vasculature.

We also compare the locations of maximum LPS at different times of the loading (temporal) in the two simulations. Figure 3.9 shows the locations of maximum LPS in the two simulations at time 40ms looking through two different planes, coronal and sagittal. There is a clear difference between the two simulations in terms of maximum LPS location. The simulation with blood vessels predicted maximum strains in the subject's left hemisphere (Figure 3.9a, red squares on the right), and there is no prediction of maximum strains in the same location from the simulation without blood vessels. Hence, the existence of the vasculature network greatly affected the

locations of maximum strains (nearly 50% reduction in maximum LPS and E_rt strains, and different predictions of maximum LPS locations).

3.6.2.3 Strain Distribution

A better idea of the strain field within the brain can be obtained by comparing the strain distributions (LPS and E_{rt}) of the whole volume of white matter. Figure 3.10 shows histograms of the strain distributions for both LPS and E_{rt} where strain values are on the x-axis and the frequency of occurrence (total number of material points with the same strain value) are on the y-axis. In addition to the visual difference between the two distributions, we notice that the distributions from the simulation without blood vessels have wider tails indicating higher overall strains. This is consistent with the results we obtained in sections 3.6.2.1 and 3.6.2.2 (higher overall average and maximum strains).

To make the comparison more quantitative, we run chi-squared test on the distributions using degrees of freedom from the histograms and 5% significance level (α). The chi-squared test is used to obtain a statistical measure of the hypothesis that adding the vasculature network significantly changes the strain distribution. If the calculated p-value of the chi-squared test is less than the chosen significance level of α=5%, the hypothesis is statistically confirmed. Chi-squared results at four different times 10, 20, 30 and 40ms indicate significant differences (p-value$<$0.00001, hence less than α=0.05) between the two distributions as shown in Table 3.4 and

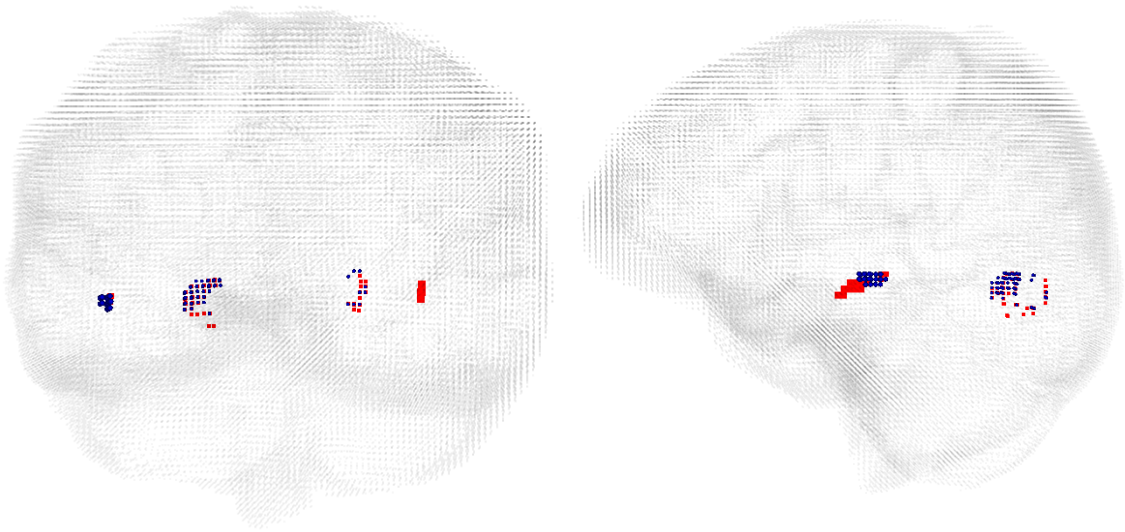

(a) (b)

Figure 3.9: Maximum LPS locations are shown for the simulation with blood vessels (red squares) and the simulation without blood vessels (blue circles) by looking through two planes a) coronal and b) sagittal. It is very clear that the locations of temporal maxima differ from one simulation to another. For example, in this time instance, the simulation with blood vessel predicted maximum strains in the subject's left side (red squares to the right of the coronal view (a)).

Table 3.4: Chi-squared test results indicating significant differences between the two simulations in terms of LPS and E_{rt} strain distributions for significance level α=0.05.

	Time (ms)	χ^2	$\chi^2_{(N,1-\alpha)}$	p-value
LPS	10	4195	132.1	<0.00001
	20	27029	224.2	<0.00001
	30	80742	149.9	<0.00001
	40	40507	145.5	<0.00001
E_{rt}	10	2276	156.5	<0.00001
	20	72168	113.1	<0.00001
	30	62998	179.6	<0.00001
	40	31298	179.6	<0.00001

hence confirm that the addition of the vasculature network significantly changes the strain fields within the brain. Moreover, note that the distributions are not normal but skewed. Given the skewness, average strains are not a good comparison measure because they do not represent the bulk behavior of the material (the average for a skewed distribution does not coincide with it's peak).

3.6.2.4 Strain w.r.t. Nearest Blood Vessel

We examine strains around the vasculature network in the simulations with and without blood vessels to explore the relationship, if any, between maximum strains and

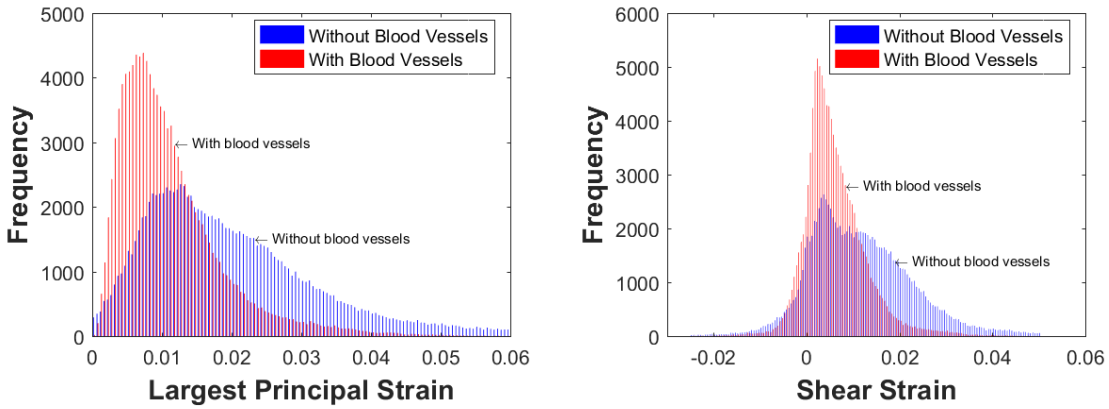

Figure 3.10: a) LPS and b) E_{rt} strain distributions at time 40ms for the simulations with and without blood vessels. The frequency values indicate total number of material points with the same strain value. Although visual differences are clear, we also run chi-squared statistical test and statistically confirmed the difference (p-value$<$0.00001). Also, the wider tails of the distributions from the simulation without blood vessels are consistent with the observation of higher overall average and maximum strains in the previous subsections.

their location with respect to the nearest blood vessel. First distance from the nearest blood vessel voxel in the original segmentation volume (MRI and TOF segmentations of secions 3.4.1 and 3.4.2) is calculated based on voxel spacing as shown in Figure 3.11. Then, the distances are mapped to our 3D head model using the nearest neighbor search method.

Figure 3.12 shows LPS on the y-axis and distance from the blood vessels on the x-axis at time 40ms for the two simulations, with and without blood vessels, using the method in the previous paragraph. Note, the distance is acquired in the reference

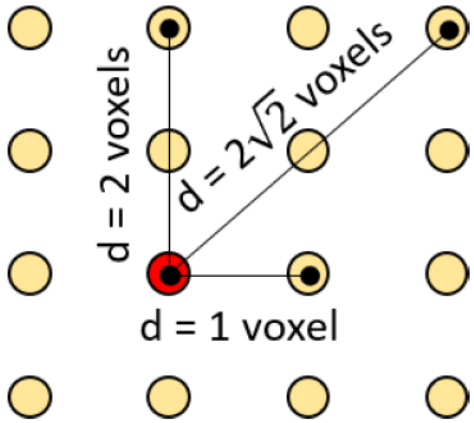

Figure 3.11: A schematic showing how the distance from the nearest blood vessel is calculated. The red point represents a voxel belonging to the blood vessels and the yellow points represent brain tissue voxels. First, the distance (d), based on the number of voxels between the vasculature voxel and the brain tissue, is assigned to each point in the original volume of the segmentation. The millimeter resolutions of the image volume is multiplied by the number of voxels to obtain distance in millimeters. Then the results are mapped using nearest neighbor search method to our 3D head model.

configuration. That means as time progresses, points can only move up and down as the strain changes for each point with time. Overall, LPS strains are smaller right next to the vessels (<3mm away from blood vessels), then strains start to increase forming two peaks. The furthest peak at around 15-20 mm away from the blood vessels exists in both simulations, possibly due to geometrical or other heterogeneity reasons (e.g.: white and gray matter interface). The first peak, however, changed its center from around 10 mm in the simulation without vasculature to 5 mm away from the blood vessels in the simulation with vasculature. Smaller strains right next to the

vessels are explained by the high stiffness of the blood vessels. Since higher stiffness means higher resistance to deformation (and hence smaller strains), the nearby brain tissue will also be affected by this resistance. Additionally, since the deformation of brain tissue next to the vessels is restricted, the soft brain tissue away from the vasculature will deform more.

3.7 Discussion

The model without vasculature predicted higher overall average and peak strains. This is likely due to lower effective stiffness of the combined brain tissues compared to the model with vasculature. Similar findings were made in the previous studies by Parnaik et al. [163], Zhang et al. [164] and Ho and Kleiven [165]. The fourth study by Omori et al. [162] only reported shear stress patters which were found to be higher in the model with vasculature.

None of the previously published studies about vasculature effects explicitly compared locations of temporal maxima (Locations of maximum strains at different times of the loading). Our simulation results indicated differences between the two models in terms of the temporal maxima. A new region (or location) of maximum LPS appeared in the simulation with blood vessels in the left cerebral hemisphere of the model. Identifying locations of higher strains is important since each position is linked to a specific cognitive function. Accordingly, we may be able to identify regions within the brain that are more susceptible to damage/injury. Although the applied loading

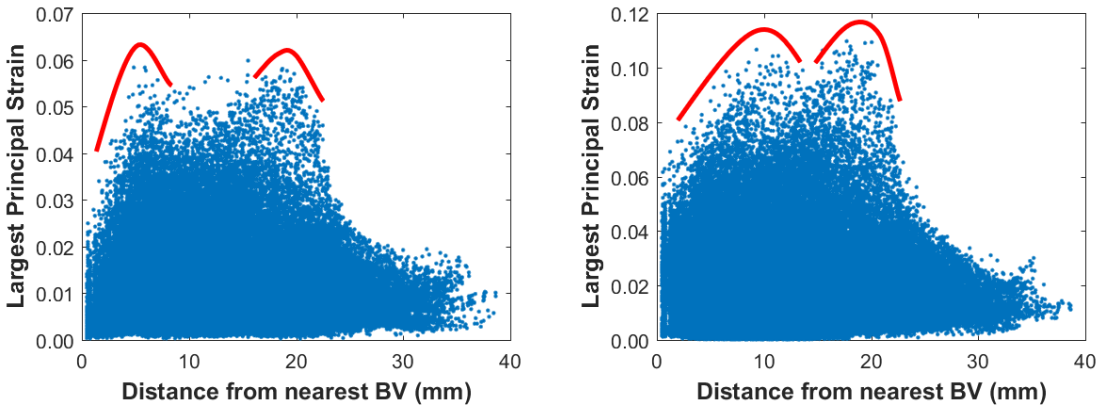

(a) **(b)**

Figure 3.12: The relation between strain values and distance from blood nearest blood vessel at 40 ms for the simulations (a) with and (b) without blood vessels (By virtually adding the vasculature structure in the simulation without blood vessels). The distance is measured in the reference configuration so each point can only change strain magnitude with time. High strains in both simulations forms two peaks (highlighted with red curves). While the second peak (between 15 to 20 mm away from nearest blood vessel) did not change location, the first peak shifted it's center from 10 mm to 5 mm and is narrower in the simulation with blood vessels. This indicates that introducing the vasculature network in the model caused a shift in the first peak due to the high stiffness of the vasculature compared to the brain tissue.

in our study is non-injurious, we expect a similar outcome when applying injurious loading (differences in maximum LPS locations).

In addition to differences in maximum LPS locations, our study shows significant differences in the strain distributions of the two simulations. This study is the first to provide quantification of strain distributions in the effort to investigate the role of the vasculature. Contradictory results (with no distribution quantification) were previously reported in the literature. Zhang et al. [164] and Parnaik et al. [163] studies revealed differences in strain patterns while the work by Ho and Kleiven [165] reported no differences in the strain patterns between the two models, with and without vasculature. In 3D simulations, like ours and Ho and Kleiven [165], it is very difficult to draw conclusions by visual inspection of the strain fields of the whole brain, and that might affect the conclusions drawn (of no difference in the strain distributions in the case of Ho and Kleiven [165]).

Our investigation about the relationship between the LPS and the distance from the nearest blood vessel revealed an interesting observation. The existence of vasculature network appears to cause high strains to concentrate or cluster around 5 mm away from the nearest blood vessel. Since the average vessel size is about 2.5 mm, the higher strains are found at a distance that is around twice the average vessel size. This result indicates that higher stiffness of the blood vessels limits the deformation of nearby brain tissue causing further deformation in the soft brain tissue once the effect of vasculature stiffness decreases at a distance of around twice the average vessel size.

A similar observation was reported by Ryu et al. [12] at very different scales (Figure 3.13). Brain slices of deceased veterans with history of mTBI were analyzed in terms of neuro-pathology. Diffuse axonal damage is observed at 50 to 200 um away from the nearest arteriole (average cerebral arterioles size is about 60 um). Although there are differences in the length scale (arteries with average size of 2.5 mm in our study vs. arterioles with average size of 60 um) and loading conditions (non-injurious in our study vs injurious in Ryu et al. [12]), but the scaling factor is common between the two studies (high strains, consequently injury, at a distance that is around twice the average vessel size). To form a better understanding of this observation, further investigation is needed for multiple length scales and possibly different types of loading conditions.

At this point, it is clear that the results supports the hypothesis of section 3.2 in that the vasculature may indeed have significant effect on the brain deformation. Further enhancements to the vasculature model can be applied like: 1) including the anisotropic behavior of the vessels 2) adding the venous network and 3) considering white matter anisotropy.

The next step is to examine the hypothesis while applying injurious loading condition. The results of the new simulations, with the injurious loading condition, will further emphasize on the significance of the vasculature network by comparing the predicted brain damage of the two models (with and without vasculature). Ultimately, the goal is to build a model that can capture realistic brain deformation and

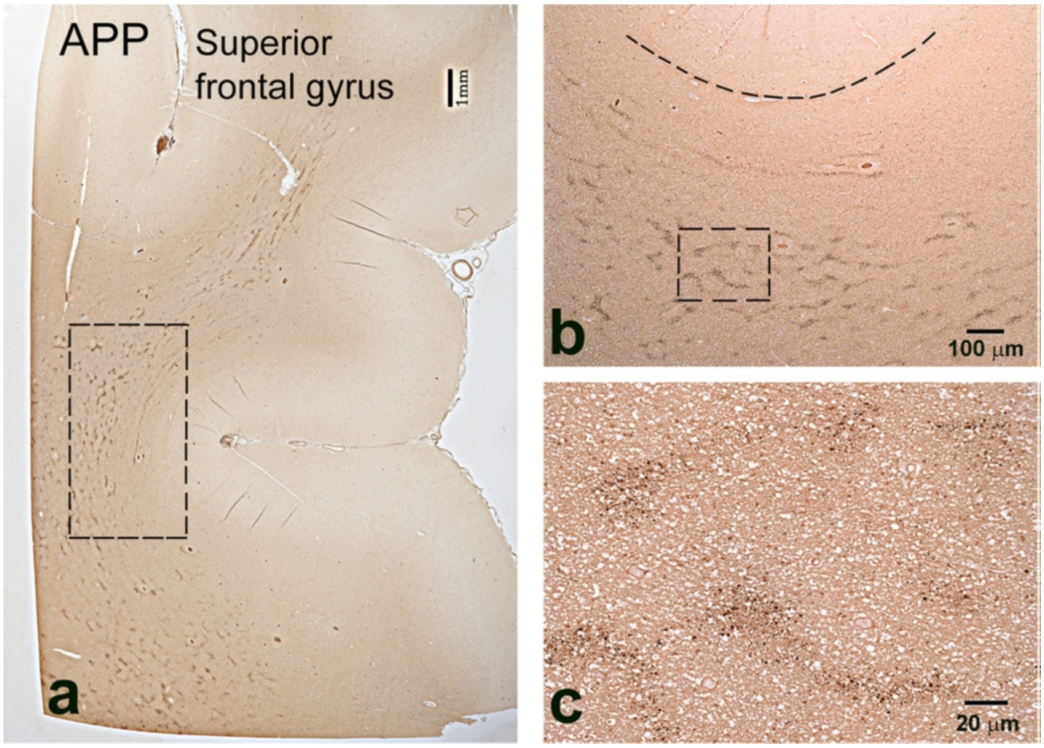

Figure 3.13: A brain slice showing axonal injury in a human subject adapted from Ryu et al. [12]. The dark spots represents damaged axons, which form clusters around the arterioles. (b) and (c) are enlargements of the blocked areas in (a) and (b), respectively. The subject had blast exposure 1 year before death and a concussion from assault 2 months prior to death.

predict damage based on applied loading conditions to help physicians in acute injury diagnosis and improve the designs of helmets and automobiles for better safety standards.

3.8 Summary of This Chapter

Investigating the effects of vasculature on the brain response required building two models one with vasculature and one without. Material parameters for the vasculature were fitted to an experiment in the literature while all parameters for the other tissues were directly taken from published computational studies. After validating the model against in-vivo brain deformation experiment, axial non-injurious loading condition was applied to both models and results are compared from several viewpoints. We find that the inclusion of the vasculature network is significant for the following reasons:

- Maximum largest principal strain and radial-circumferential strain decreased about 50% after the addition of the vasculature and locations of maximum strains differed between the two models. The strains from the two models start to diverge at around 20 ms which is the transition phase between acceleration and deceleration motions.

- Strain fields are significantly different since statistical chi-squared test with segnificance level of 0.05 resulted in p-value$<$0.00001. This statistical study was not performed in any of the previous studies.

- A shift in high LPS strains from 10 mm to 5 mm away from the blood vessels indicates how the addition of the stiff vasculature restricted deformation of brain

tissue right next to the vessels and forces soft brain tissue away from the vessels to deform more.

In the next chapter, we further investigate the role of vasculature network on the brain deformation under injurious loading. Predicted injuries in the models with and without vasculature will provide insights on the impact of adding the vasculature network to computational models of mTBI. Furthermore, the effect of the loading direction on the predicted injury is going to be explored.

Chapter 4

The Effects of Vasculature on Mild TBI*

4.1 Introduction

In Chapter 3, we demonstrated that the cerebral arteries affect the brain deformations under non-injurious inertial loading. Of the four previous studies in this area, only Ho and Kleiven [165] had a 3D computational model including vasculature. However, all of these studies (Omori et al. [162], Parnaik et al. [163], Zhang et al. [164], Ho and Kleiven [165]) applied injurious loading (acceleration pulses) and predicted possible high strains and/or stresses in the brain tissue (potential injury locations).

*The work of this chapter was done in collaboration with the Image Analysis and Communications Lab (Jeffrey Glaister and Prof. Jerry Prince). TRACULA segmentation in Section 4.3.2 was executed by Jeffrey Glaister.

In this chapter, we examine how the vasculature network affects the brain deformation under injurious loading. The investigation is divided into two parts. First, we recap briefly the 3D head model development with the MPM implementation. Then, an injurious loading condition from an NHL accident is applied to two models, one with and one without vasculature. Once the effects of vasculature are captured, we also examine how the loading direction affects the predicted injury in terms of severity and location.

4.2 Methods

In this section, we recall briefly the 3D head model built in Chapter 3 and the MPM implementation of the model. Then, the loading condition will be defined and two study cases will be established.

4.2.1 The Three Dimensional Head Model

To build the 3D head model we used the MRI and TOF images of the subject in section 3.4 and followed the same procedures in sections 3.4.1 and 3.4.2. For a quick recap, the captured anatomical structures are: skull, CSF, ventricles, white and gray matters, falx, tentorium and cerebral arteries. The segmentation order was performed such that the vasculature is added at the last step, so that we can develop a model

with vasculature and another model without vasculature. The segmented volumes have an isotropic resolution of 0.8 mm.

4.2.2 Material Point Method Implementation

As we explained in section 3.4.3, the choice of the computational method (MPM) is to overcome complications in the finite element method (such as mesh entanglement and difficulty meshing complex structures). Similar to our application in section 3.4.3, the segmented structure is reduced to 1.6mm isotropic resolution (to cut down on the computational cost) and the convected particle domain interpolation is used to capture large and shear deformations. In this Chapter, we use two versions of the head model, one with and one without vasculature, and the material properties of section 3.4.4 which have been used in the validation of our model (section 3.5).

4.2.3 Injurious Loading and Injury Criterion

To simulate injurious scenario we used the loading conditions of the NHL accident of section 2.2.6. Since the MPM application requires the displacement loading condition and not the acceleration, we integrate the NHL accelerations (Figure 4.1b) twice to produce the position profile for the three directions: axial (z-direction), coronal (x-direction) and sagittal (y-direction) as shown in Figure 4.1c. The axial rotation has the highest magnitude ($\approx$ 8000 rad/s^2), followed by the coronal rotation ($>$ 6000 rad/s^2) while the sagittal (Y) has the lowest rotational acceleration ($<$ 3000 rad/s^2).

If we look at the position profile, the axial loading rotates the head about 23 degrees, the sagittal follows with about 4.6 degrees and then the coronal rotation of 3.4 degrees.

Recall from section 3.4.3, that the Uintah framework for MPM implementation requires defining a global computational space, typically bigger than the simulated object, and any points leaving this domain during the loading/deformation will not be tracked (in other words, the deformation information for that point will be lost). Hence, to lower the computational cost associated with the global domain setup we choose the coronal (X) loading (Figure 4.2 a and b) and apply it as follows:

- Study #1, Effect of Vasculature in mTBI: Apply the acceleration profile to the axial direction for the two head models, with and without vasculature (Figure 4.2c). The choice of the axial direction loading is important to make a better connection between the injurious scenario in this chapter and the non-injurious case of Chapter 3.

- Study #2, Effect of Loading Direction on white matter injury predictions: Apply the acceleration profile on the head model with vasculature once in each direction: axial, coronal and sagittal (Figure 4.2d). This case will give us insights on the level of vulnerability of white matter with respect to the loading direction.

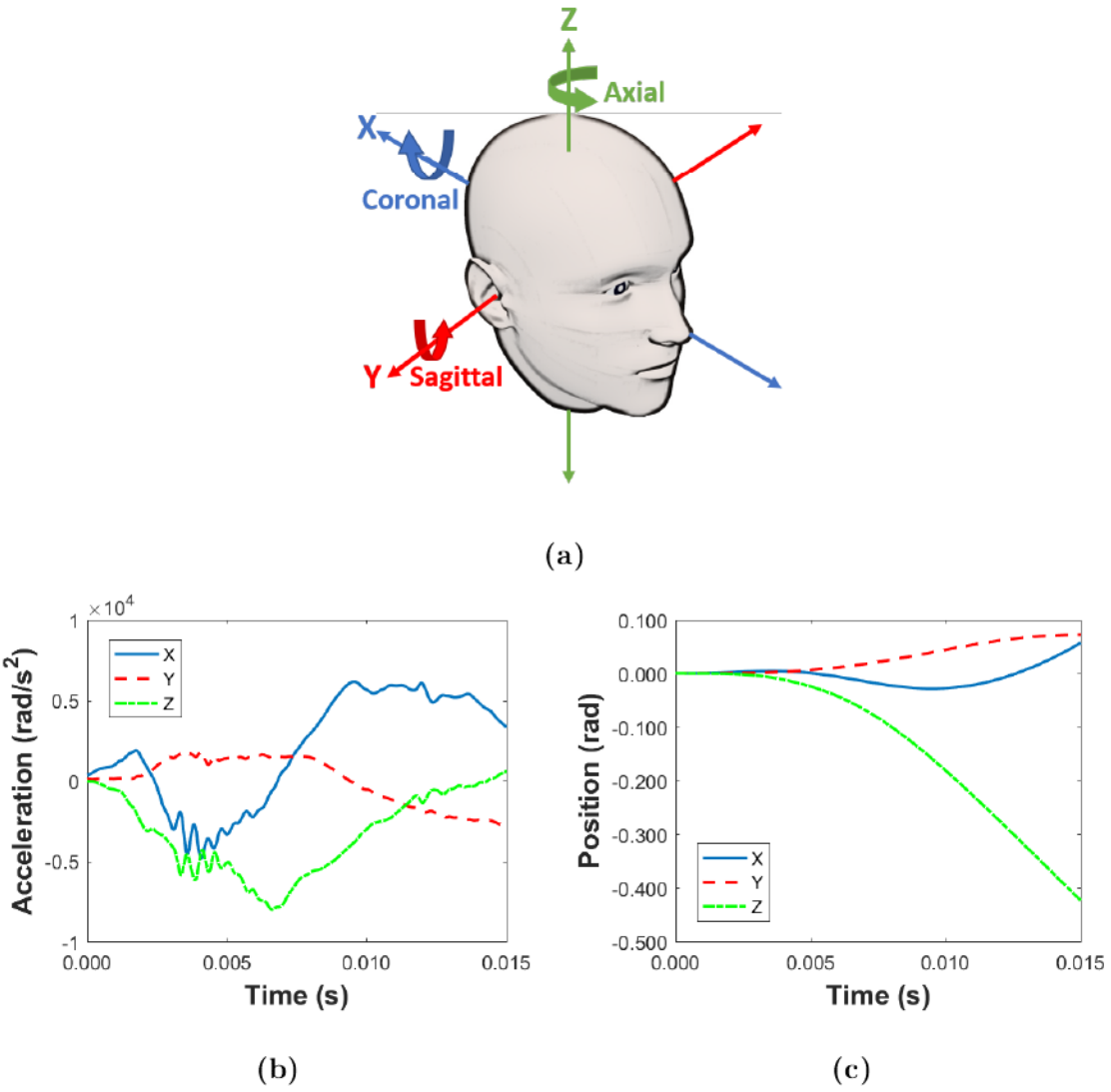

Figure 4.1: a) A schematic showing the coordinate system of the head used in our study and the corresponding rotations. b) The angular accelerations about the x-axis (coronal rotation), y-axis (sagittal rotation) and z-axis (axial acceleration) of an NHL accident reproduced from Wright et al. [3]. c) The angular position profile calculated by integrating the accelerations of the NHL accident twice.

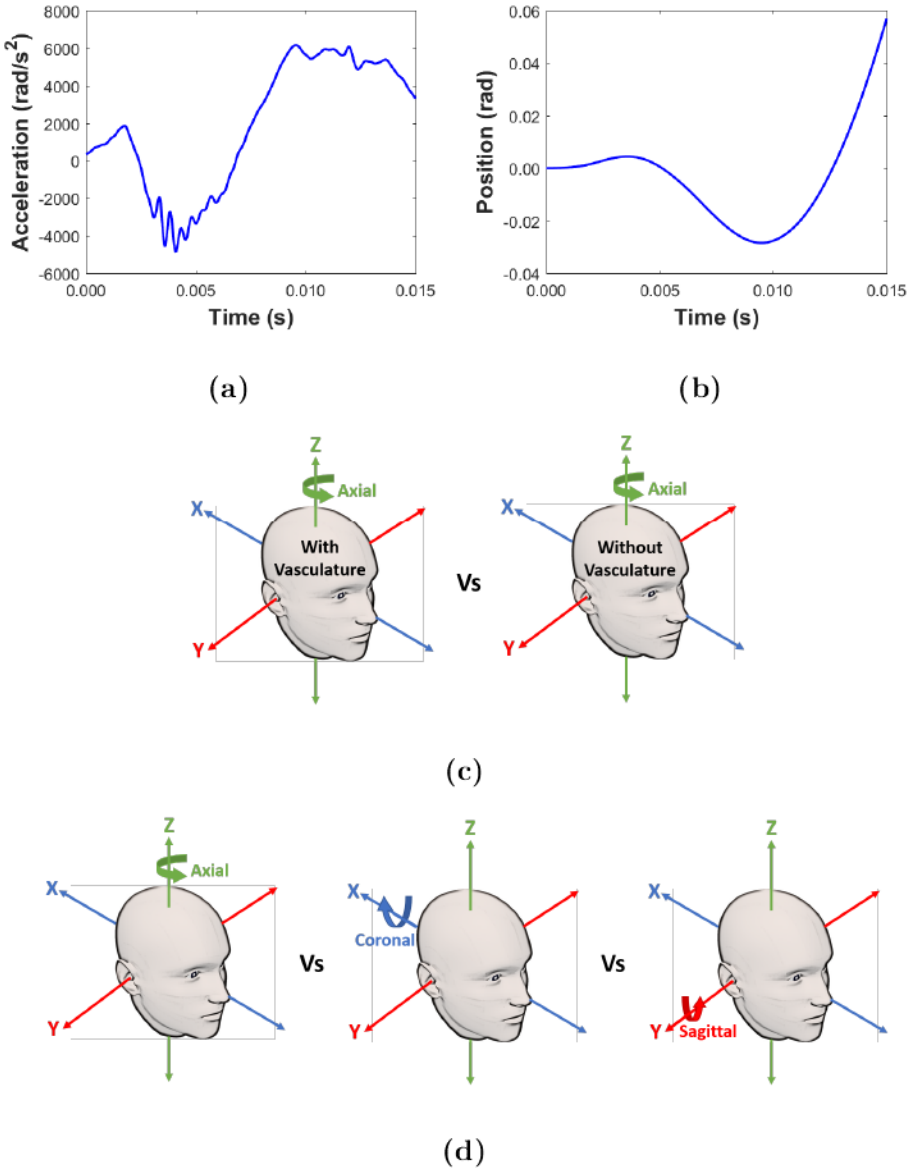

Figure 4.2: a) The angular acceleration and b) The angular position profiles Chosen for The two studies in this chapter. In the First study (c) injury predictions will be compared between two models, one with and one without vasculature. Then, the model with vasculature will be used for the second study (d) to examine the effect of the loading direction on injury predictions.

Clearly, for both case studies, the loading is expected to cause injury in the brain tissue, hence an injury threshold must be defined. Since the white matter is modeled as a transversely anisotropic material (Equation 2.9) with the dominant axonal bundle direction $\mathbf{a_0}$, axonal strain will be used as an injury predictor. Recall from section 2.2.5, an optimal axonal strain threshold of 18% is adapted from the experiment of Bain and Meaney [128]. This injury criterion has been widely used in the recent literature (Wright et al. [3], Wright and Ramesh [92], Ji et al. [194], Zhao et al. [195], Sullivan et al. [196]). For a better comparison to the results of Chapter 3, the Largest Principal Strain (LPS) will also be computed and used as a comparative measure. Two LPS thresholds were established in the literature from accident reconstructions, 31% (Deck and Willinger [115]) and 21% (Kleiven [120]). We will use the LPS threshold of 31% in our computational study.

4.3 Results

The results of the first case study will be shown first. The extent and locations of predicted injury will be compared between the two models, with and without vasculature. After investigating the role of vasculature network in terms of injury predictions, the second case study results will be examined. The model with vasculature is used in three simulations each with a different loading direction. First, white matter tracts will be segmented based on a tractography atlas. Maximum strains (LPS and axonal strain) in the white matter overall volume and in each white matter tract will be

compared between the three loading directions. Additionally the injury predictions will be explored using the thresholds of LPS≥31% and axonal strain, ϵ_{Axon} ≥18%).

4.3.1 Vasculature effects in mTBI

Two simulations, with and without vasculature, with rotational acceleration applied to the axial direction were performed. Largest principal strain (LPS) is used as a comparative measure to results of Chapter 3 and axonal strain (ϵ_{Axon}) is also used to utilize the sophistication of white matter in this chapter. To understand localized effects, strains in the white matter substructures (cerebral-WM, cerebellar-WM and brainstem) are calculated.

4.3.1.1 Injury Predictions: Extent of Injury

The injury predictions based on ϵ_{Axon} >18% and LPS>31% are located in the cerebrum only (In the second study we will show the effect of loading direction on each white matter substructure). The extent of injury is examined in terms of volume fraction (V_f) which is calculated as follows

$$V_f = \frac{\text{\# of white matter mater material points exceeding the threshold}}{\text{Total \# of white matter material points}}. \quad (4.1)$$

Table 4.1 shows the volume fractions of the cerebrum. Using both measures, the simulation without blood vessels predicted slightly higher injury levels. This observation is consistent with the results of Chapter 3, which showed higher overall

Table 4.1: Injury predictions for the simulations with and without blood vessels using both Largest Principal Strain (LPS>31%) and axonal strain (ϵ_{Axon}>18%) as injury measures. The values represent volume fractions (V_f) of the cerebrum above the strain threshold.

	V_f with blood vessels	V_f without blood vessels
LPS>31%	5×10^{-3}	5.5×10^{-3}
ϵ_{Axon}>18%	3.25×10^{-3}	3.3×10^{-3}

averages and maximum strains in the simulation without blood vessels. We should note that changing the threshold value or the strain measure will lead to a different result.

4.3.1.2 Injury Predictions: Locations of Injury

Locations of predicted injury are extracted for both measures as shown in Figure 4.3. Injury predicted using the model with vasulature is shown in red while the blue color represents injury locations predicted using the model without vasculature. Differences in predicted injury locations by each model are evident. Also, we note the differences in the injury locations in one model but using the two injury criteria of ϵ_{Axon} >18% and LPS>31% (i.e.: Compare the red locations between Figure 4.3a and 4.3c). Note that there are multiple locations of predicted injury in a single/isolated material point which require further investigation in the future using multiple resolutions to check if the reason is numerical locking or not. This could also depend on the process

of interpolating the DTI information to extract the fiber direction, which does not necessarily form a connected network due to the inclusion of a single family of fibers.

4.3.2 Effect of loading direction on injury predictions

In this section, since the focus is on injury predictions, injury will be investigated in each white matter substructure (using LPS and axonal strain) and in major white matter tracts (using axonal strain only). To identify which white matter points belongs to which tract we used the TRActs Constrained by UnderLying Anatomy (TRACULA) method (Yendiki et al. [197]). This method compares DTI volumes to tractography atlas and segment white matter tracts according to the atlas information. The extracted white matter tracts are listed in Table 4.2. Recall in our head model only the arteries are resolved, hence the results in this section will be affected if we add the venous network and more specifically the bridging veins since they impose a distinct boundary condition at the superior (top) surface of the brain.

4.3.2.1 Maximum Strains

Maximum strains experienced by white matter substructures are listed in Table 4.3. The cerebellum has consistent maximum strains with respect to loading direction using both LPS and ϵ_{Axon}, it experiences higher strains when loaded in the coronal direction followed by the sagittal and then the axial directions. If we look to the cerebrum and the brainstem, we find that the axial direction strains predicted using

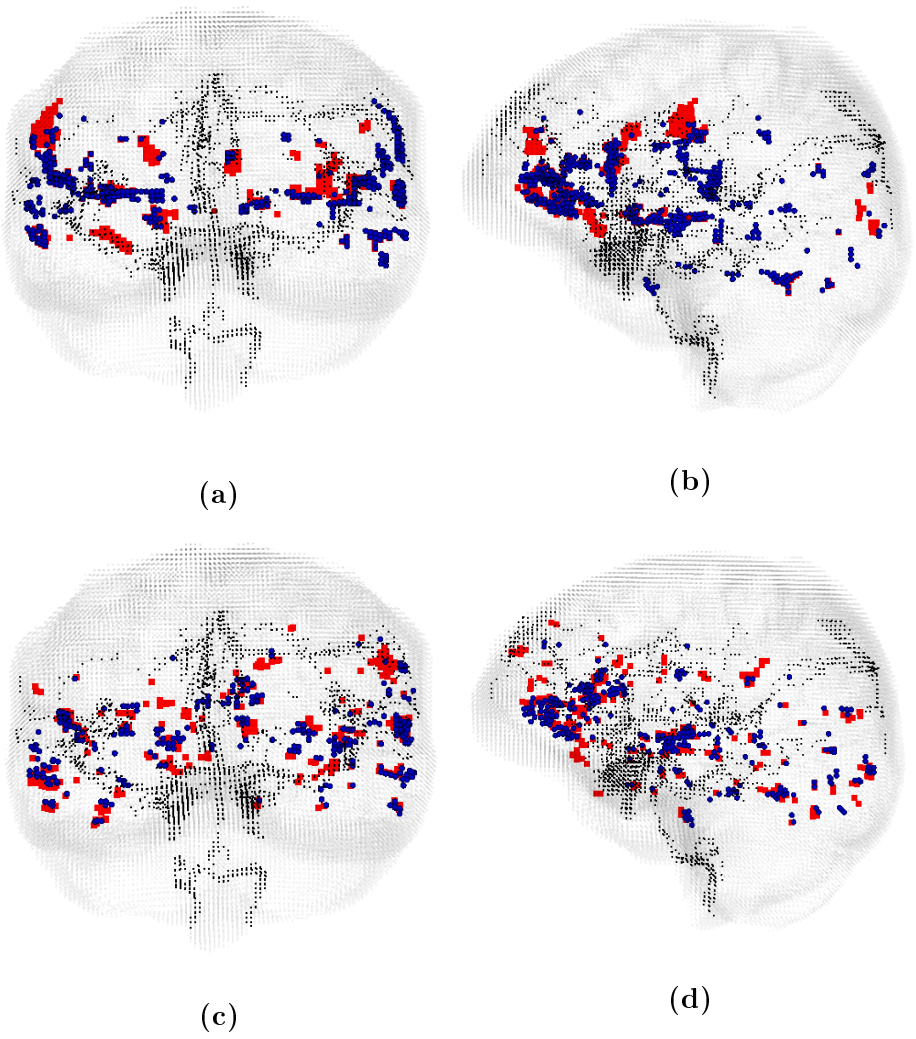

Figure 4.3: Location of damaged material points for the largest principal strain criterion (showing (a) front and (b)side views) and the axonal strain criterion (showing (c) front and (d)side views) for both models with (red squares) and without (blue circles) vasculature (Black points represent the blood vessels). Significant differences exist between the two models since there are many isolated locations predicted by one of the models but not the other. We should also note that locations of damage differ from one injury criterion to another.

Table 4.2: Extracted white matter tracts using TRACULA method (Yendiki et al. [197]).

Tract #	Abbreviation	Full Name
1	ATRL	Anterior Thalamic Radiation Left
2	ATRR	Anterior Thalamic Radiation Right
3	CABL	Cingulum - Angular (infracallosal) Bundle Left
4	CABR	Cingulum - Angular (infracallosal) Bundle Right
5	CCGL	Cingulum - Cingulate Gyrus (supracallosal) bundle Left
6	CCGR	Cingulum - Cingulate Gyrus (supracallosal) bundle Right
7	CSTL	Cortico-Spinal Tract Left
8	CSTR	Cortico-Spinal Tract Right
9	FMAJ	Corpus callosum - Forceps Major
10	FMIN	Corpus callosum - Forceps Minor
11	ILFL	Inferior Longitudinal Fasciculus Left
12	ILFR	Inferior Longitudinal Fasciculus Right
13	SLFPL	Superior Longitudinal Fasciculus - Parietal bundle Left
14	SLFPR	Superior Longitudinal Fasciculus - Parietal bundle Right
15	SLFTL	Superior Longitudinal Fasciculus - Temporal bundle Left
16	SLFTR	Superior Longitudinal Fasciculus - Temporal bundle Right
17	UNCL	Uncinate fasciculus Left
18	UNCR	Uncinate fasciculus Right

LPS and ϵ_{Axon} are consistent in the following sense: highest strains are predicted in the cerebrum and lowest in the brainstem using both measures. Further, maximum LPS is the same for the cerebrum when loaded coronally versus sagittally but maximum axonal strain is higher in the cerebrum under sagittal rotation. Hence, the cerebrum is more likely injured when loaded in the axial direction followed by the sagittal direction and then the coronal direction.

The brainstem maximum LPS is experienced when loaded in the coronal direction followed by the sagittal direction while maximum axonal strain is the opposite. However, the brainstem experienced low strains when loaded in the axial direction. Therefore, susceptibility to injury in the brainstem is very low when loaded axially since the maximum LPS strain is only 12% (about one third of the injury threshold) and the maximum axonal strain is only 10% (about half the injury threshold).

The cerebellum experienced the highest LPS and axonal strains when loaded in the coronal direction followed by the sagittal and then the axial direction making it more susceptible to injury during coronal loadings. The geometry of each white matter substructure possibly affected the vulnerability to injury in the three loading directions which we will explain further in the discussion.

Clinical (McKee et al. [198]) and computational (Ghajari et al. [199]) efforts in the literature focused on the location of injury and maximum strains with respect to the gyri (the folds) and sulci (the grooves) of the cerebral cortex. Both studies (McKee et al. [198], Ghajari et al. [199]) have shown that more injured cites (clinical

observations and high strains in the simulation) are found in the depths of the cerebral sulci. Figure 4.4, shows the LPS map for a coronal cut through the cerebrum for the coronal rotation simulation (the darker the color, the higher the strain). By examining LPS in the white matter, high values are located at the "gyri" of white matter. Furthermore, higher LPS values in the gray matter exist closer to the sulci and at the lower surfaces of the gyri, forming a band as shown in Figure 4.4. Hence, if the whole brain (white and gray matter combined) is examined, high LPS clusters in the shape of a band that starts at the lower surface of the gyri and extends into the depths of the sulci. A similar observation of the high LPS clusters is found for the axial and sagittal rotations.

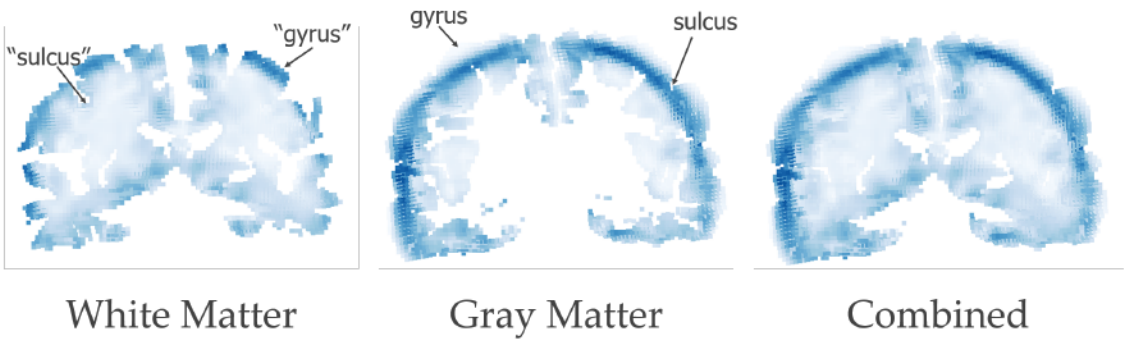

Figure 4.4: Largest principal strain map for a coronal slice of the coronal rotation simulation. Locations of high (dark blue) LPS are concentrated at the white matter "gyri", the lower surface of the cerebral cortex gyri and into the depths of the sulci. These locations agree to some degree with observations in the literature.

Table 4.3: Maximum Largest Principal Strain (LPS) and axonal strain (ϵ_{Axon}) experienced by the white matter substructures: cerebrum, cerebellum and brainstem.

		Cerebrum	Cerebellum	Brainstem
Max LPS	Axial	0.47	0.21	0.12
	Coronal	0.35	0.45	0.59
	Sagittal	0.35	0.32	0.39
Max ϵ_{Axon}	Axial	0.3	0.16	0.1
	Coronal	0.225	0.315	0.23
	Sagittal	0.26	0.235	0.255

Figure 4.5 shows maximum axonal strain, ϵ_{Axon}, experienced by the white matter tracts for each loading direction. Most of the tracts experienced higher axonal strains when loaded in the axial direction except tracts 4, 8, 12 and 15 (CABR, CSTR, ILFR and SLFL) which have higher strains in the sagittal loading direction and tracts 7 and 13 (CSTL and SLFPR) with higher strains in the coronal loading case. High axonal strains in each tract could possibly indicate higher vulnerability to injury for a specific loading direction. To have a more solid conclusion, we will investigate the predicted injury in the next section. Note, no correlation is found between locations of maximum axonal strains with respect to the gyri and sulci of the cerebral cortex.

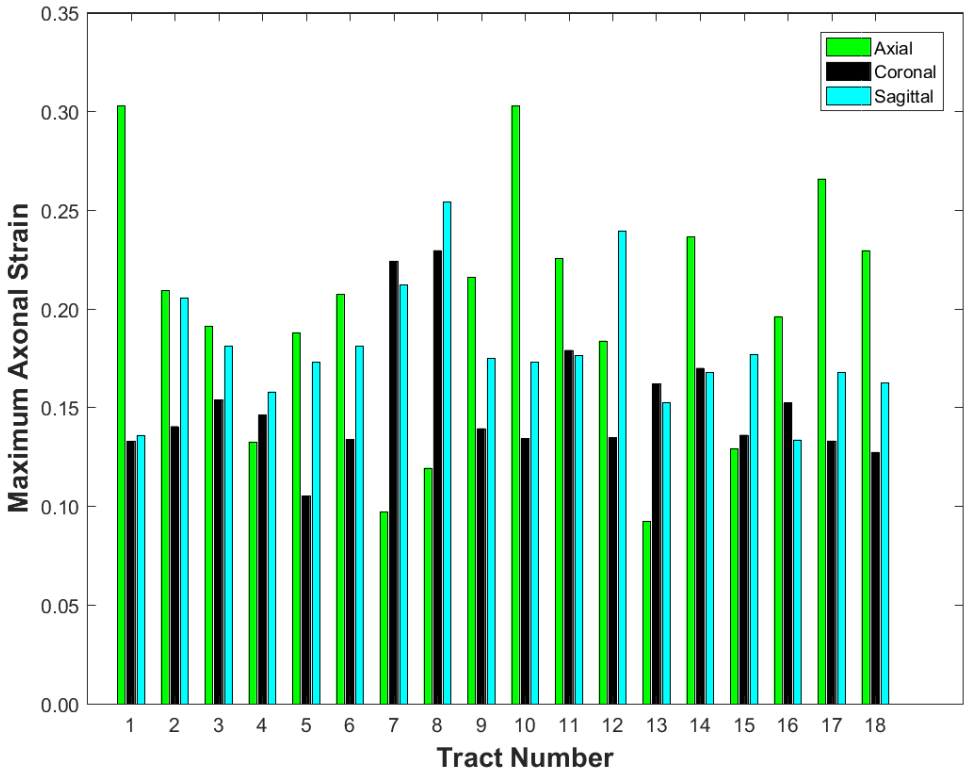

Figure 4.5: Maximum axonal strain (ϵ_{Axon}) for each tract in Table 4.2 experienced in each loading direction scenario.

4.3.2.2 Injury Predictions

Table 4.4 shows volume fractions of white matter substructures with injurious strains (LPS≥31% and ϵ_{Axon} ≥18%) as a measure of the extent of injury. The volume fractions are calculated using Equation 4.1. Coronal loading affected both the cerebellum and the brainstem the most, while axial loading caused higher degree of injury (higher V_f) in the cerebrum.

Table 4.4: Injured volume fractions for each white matter structure. Injury thresholds are 31% and 18% for LPS and ϵ_{Axon}, respectively.

		Cerebrum	Cerebellum	Brainstem
V_f of LPS≥31%	Axial	5×10^{-3}	0	0
	Coronal	0.1×10^{-3}	0.068	0.0223
	Sagittal	0.5×10^{-3}	0	0.015
V_f of ϵ_{Axon} ≥18%	Axial	3.25×10^{-3}	0	0
	Coronal	0.3×10^{-3}	0.035	0.0035
	Sagittal	2.25×10^{-3}	0	0.015

Injury levels of white matter tracts based on the volume fraction are shown in Figure 4.6. Like white matter substructure V_f calculations, injured volume fractions of white matter tracts are calculated based on the ratio between material points exceeding injury threshold to total material points of each white matter tract. No injury is observed in tracts 4, 13 and 15 (CABR, SLFPR and SLFL). The sagittal loading was most injurious for tracts 2, 7, 8 and 12 (ATRR, CSTL, CSTR and ILFR) while the axial loading caused higher injury (in terms of V_f) in all other tracts. By comparing these results with the maximum axonal strains in each tract, we can see that the extent of injury in white matter tracts is not necessarily correlated with the maximum strains (e.g.: tract #7, CSTL, maximum axonal strain resulted from coronal loading while injury level is higher in the same tract under sagittal loading).

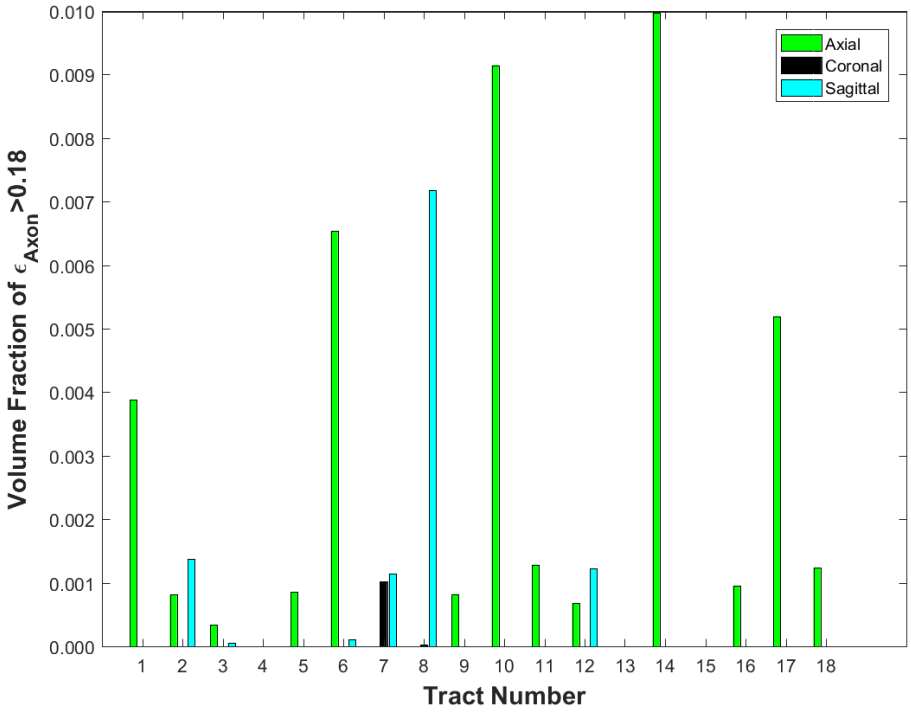

Figure 4.6: Maximum axonal strain (ϵ_{Axon}) for each tract in Table 4.2 experienced in each loading direction scenario.

4.4 Discussion

In the first case study we evaluated the predicted injury in terms of extent and location for the two models: with and without blood vessels. The injured volume fractions of white matter in the model without blood vessels are higher using both injury thresholds (axonal strain ϵ_{Axon} >18% and Largest Principal Strain LPS>31%). This result agrees with the findings in Chapter 3, in which maximum and average strains are also observed in the simulation with blood vessels. The added stiffness

from the vasculature network increases the overall stiffness of the brain tissue and hence decrease the strains and predicted damage.

When comparing locations of predicted injury, the two models (with and without vasculature) show differences in the locations of injured material points. Several regions of predicted damage in the model with blood vessels were not injured using the model without blood vessels and vice-versa. This observation leads to the conclusion that adding the vasculature network is important for mTBI injury predictions, which is not carefully compared in the previous literature of vasculature effects in mTBI (Omori et al. [162], Parnaik et al. [163], Zhang et al. [164], Ho and Kleiven [165])). Also, the two injury criteria (LPS and ϵ_{Axon}) show different regions within the brain being injured. This result raises a question about which injury criterion should be used for injury predictions. Since there are no direct links between actual observations of mTBI and specific injury locations, the choice of injury criterion is not obvious.

The second case study focused on the effect of loading direction on the brain response using the model with blood vessels. The highest overall white matter strains and injured volume fractions are associated with the coronal loading (Tables 4.3 and 4.4). Hence, white matter susceptibility to injury overall is highest for coronal loading. However, injury in the segmented white matter tracts is induced the most when axial loading is applied. To resolve this contradiction in the extent of predicted injury between overall white matter results (coronal loading is the most injurious) and the results of individual tracts (axial loading is more injurious), we focus our attention on

the results of individual white matter structures: cerebral-WM, cerebellar-WM and brainstem. The cerebrum is most vulnerable to injury under axial loading while the cerebellum is more vulnerable to injury under coronal loading and the brainstem is more vulnerable to injury under coronal and sagittal loadings (Based on volume fractions using both thresholds, axonal strain ϵ_{Axon} >18% and Largest Principal Strain LPS>31%). The cerebrum higher volume fractions under axial loading agrees with the tracts vulnerability to injury since most of the resolved tracts using TRACULA method lie in the cerebrum.

Additionally, extent of injury results also agree with the geometry of each structure with respect to axis of rotation (Figure 4.7). The cross-sectional area perpendicular to the axis of rotation is a measure of original/reference length, which can be used to estimated the local moments experiences by each structure (The longer the moment arm (wider cross-sectional area perpendicular to the axis of rotation in our case), the higher the induced moment). The cerebrum has its widest cross-sectional area perpendicular to the axial axis of rotation increasing the amount of shearing, and consequently strains, in the white matter tissue. Similarly, the cerebellum has its widest cross-sectional area perpendicular to the coronal axis of rotation. The brainstem, on the other hand, have its widest cross-sectional area perpendicular to both the coronal and sagittal axes, which explains why it experienced higher levels of injury under the coronal loading using LPS as an injury threshold and under sagittal loading using axonal strain as an injury predictor.

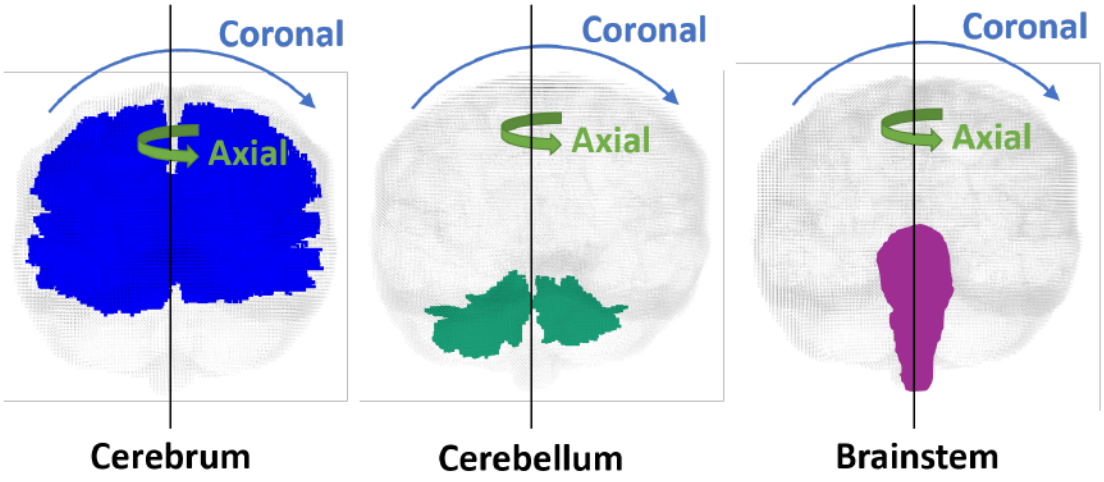

Figure 4.7: A frontal view of the white matter substructures cross-sections showing the axial and coronal rotations. The widest cross-section of the cerebrum is perpendicular to the axial axis of rotation while the widest cross-sections of the cerebellum and the brainstem are perpendicular to the coronal axis of rotation. By rotating the wider planes, more shear deformation (and consequnetly higher strains) is allowed in the structure which explains the higher vulnerability to injury in the cerebrum for axial loading and in the cerebellum and brainstem for coronal loadings.

The vulnerability of these structures to injury under the different loading directions has been highlighted using other loading scenarios in the computational mTBI literature. Zhang et al. [77] performed 3D finite element studies of the effect of impact direction on the brain response. The study concluded that lateral (coronal) impacts induced higher shear stresses and strains in both the corpus callosum (cerebrum) and brainstem compared to frontal (sagittal) impacts. Another study by Kleiven [200] used finite element modeling to study the effect of impacts and rotations. Higher

values of largest principal strain were associated with loading in the coronal direction compared to the sagittal loading. Furthermore, Takhounts et al. [201] reconstructed collegiate football games and used finite element modelling to study the severity of injury based on the impact/loading direction. Their study concluded that coronal impacts resulted in a higher degree of injury compared to the sagittal loading direction. Altogether, our findings about the coronal loading being the most injurious compared to the sagittal loading agrees with the aforementioned studies in the literature.

Moreover, multiple groups of researchers have performed experiments in different loading directions using human primates and non-primate animals (Smith et al. [13], Krave et al. [17], Gutierrez et al. [202], Runnerstam et al. [203], Browne et al. [204], Gennarelli et al. [205]). Sagittal and coronal rotational effects were compared in an experiment on monkeys by Gennarelli et al. [205]. The head of the animal is fixed to a device which induced a sixty degrees rotation in each direction. Coronal rotations produced brain lesions (scar tissue) in the corpus callosum and the cerebellum in addition to prolonged disabilities. These outcomes generally agree with our results which predicted overall white matter higher injuries and injury in the cerebellum only after coronal rotations. Smith et al. [13] performed axial and coronal rotational experiments on pigs and compared axonal damage and coma severity. Axial rotations produced substantial damage to the brainstem which is correlated with persistent coma whereas coronal rotations produced more extensive damage to the frontal and parietal lobes of the cerebrum. While these results seems to contradict ours, the

observation can be explained if we examine the anatomy of the brainstem in pigs compared to humans. Axial rotations of the pig heads are perpendicular to the long axis of the brainstem and the opposite is true for coronal rotations. Hence, pig axial rotations are similar to human coronal rotations and vice versa (pigs coronal rotations are similar, anatomically, to human axial rotations), as shown in Figure 4.8. By this analogy, our results are consistent with Smith et al. [13] in the following sense: rotations perpendicular to the brainstem's long axis produce more damage to the axons of the brainstem, while rotations around the axis of the brainstem produce more damage to the cerebral white matter. Another coronal to axial comparison using pig experiments is performed by Browne et al. [204]. Axial rotations induced loss of concussion and more diffuse axonal injury in cerebral white matter and in the brainstem. Using the same analogy we just explained about the long axis of the brainstem, our results confirms the same vulnerabilities to injury for human coronal rotations (which are equivalent to pigs axial rotations).

Of course any computational study has some limitations. Our study using a 3D head model of a single subject and one specific loading condition revealed differences between the results of the model with and the model without vasculature. The extent of the difference between the two model could change using a different subject or a loading condition. Hence, further investigation using multiple models built based on different subjects will provide a better global conclusions about the effects of vasculature in mTBI. Moreover, there are no clear connections, yet, between

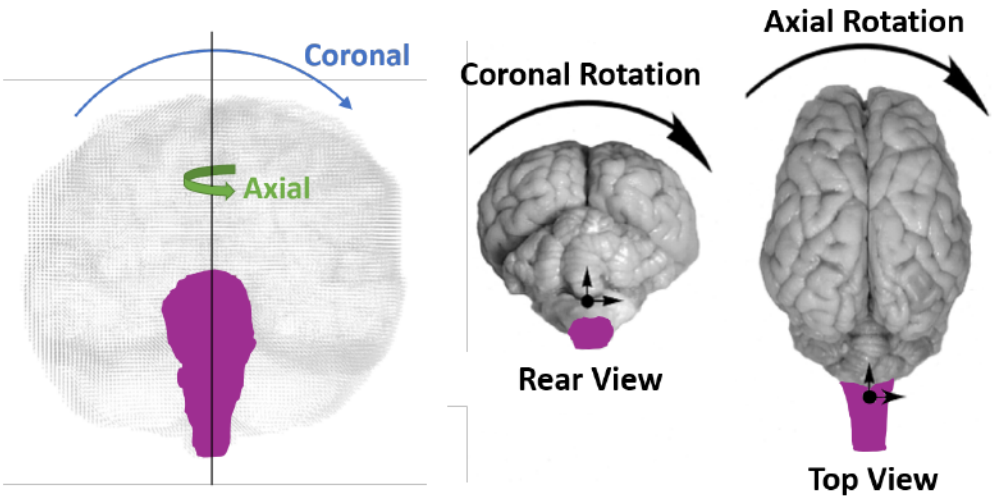

Figure 4.8: A comparison of the loading direction compared to the geometry of the brainstem between (a) human and (b) pig brains (The dark pink color represents the brainstem). The axial rotation of the pig head is perpendicular to the long axis of the brainstem which is similar to the coronal rotation in human brain. The opposite, coronal rotation of the pig head is anatomically equivalent to axial rotations of the human head, is also true. Pig brain illustration (b) is adapted from Smith et al. [13].

actual observations of mTBI and exact locations of predicted injury in the computational models (which is affected by the values of the thresholds and other factors like anatomical details and chosen material models and parameters). Hence, changing the injury threshold might also result in different vulnerabilities of the white matter regions.

4.5 Summary of This Chapter

Two studies were executed in this chapter. the first study focused on the effects of vasculature network in mTBI. Extent of injury based on injured volume fractions are higher in the model without blood vessels. The overall stiffness of the brain tissue increases after the addition of the stiff vasculature network and hence decrease the amount of deformation in the tissue. Moreover, the two models, with and without vasculature, predicted different injury locations which is key established early diagnosis of mTBI. However, since well documented cases of mTBI patients including loading condition, acute symptoms and long-term complications do not exist yet, it is not obvious which injury predictor (largest principal strain or axonal strain) is better than the other.

The same loading profile used in the first study (a rotational loading with maximum acceleration of about 6000 rad/s^2) applied once to each direction: axial, coronal and sagittal. The level of injury is calculated based on two commonly used thresholds in literature which are the largest principal and axonal strains. Overall coronal rotation is the most injury inducing among the three directions. This observation agrees with accident reconstruction studies and animal experiments of mTBI in the literature.

In the next chapter, the effect of gray matter heterogeneity in mTBI is going to be examined. The largest principal strain results of two models, with homogeneous

and heterogeneous gray matter, will provide insights on the importance of modelling gray matter substructures in head models for mTBI.

Chapter 5

Gray Matter Heterogeneity in mTBI*

5.1 Introduction

The last component of brain heterogeneity in our study is gray matter. Gray matter consists of neuronal cell bodies surrounded by glial cells such as oligodendrocytes, microglia and astrocytes. The morphology of the cells in gray matter lacks a dominant orientation, and hence the gray matter is usually treated as an isotropic material. There are several gray matter regions within the brain, including cortical gray matter, thalamus, putamen, hippocampus, basal ganglia, caudate and hypothalamus. Recent studies have shown that there are differences in mechanical properties of the several gray matter substructures (Lawson et al. [206], Elkin et al. [207], Finan et al. [208]).

*The work of this chapter was done in collaboration with Jeffrey Glaister and Prof. Jerry Prince from the Image Analysis and Communications Lab. Segmentation of gray matter substructures was executed by Jeffrey Glaister.

Moreover, specific gray matter substructures have been linked to mTBI cognitive impairments (Grossman et al. [209], Hicks et al. [210], Gosselin et al. [211]) which suggests that they may play an important role in injury prediction and identification.

In this chapter we will explore the consequences of the heterogeneity of gray matter through computational modelling. Two models, with homogeneous and heterogeneous gray matters, will be simulated using an injurious loading from the previous chapter. Strains within each gray matter substructure will be compared and injury will be estimated using a gray matter injury threshold published in the literature.

5.2 Methods

In order to study how the heterogeneity of gray matter affects the deformation under injurious loading, we will first identify regions of interest (i.e.: gray matter substructures), then build two models, one with the identified regions of interest and one with homogeneous gray matter. An injurious loading will then be selected and applied to each model.

5.2.1 Gray Matter Substructures

Although numerous experiments in the literature focused on characterizing the brain tissue, very few have targeted localized characterization, using rats (Lee et al. [190], Elkin et al. [212]), pigs (Elkin et al. [213], Chen et al. [214]) and more recently

human brains (Finan et al. [208]) . Based on these experiments, which constitute the only available tissue properties in the literature, we choose to focus our study on the following four gray matter substructures: caudate, hippocampus, putamen and thalamus.

Following the same methods of section 3.4.1, the four gray matter substructures are segmented as shown in Figure 5.1. The final segmentation of the whole head has the following structures: skull, CSF, falx, tentorium, white matter (cerebral, cerebellar and barinstem), caudate, hippocampus, putamen, thalamus, other gray matter (cerebral and cerebellar), ventricles and arteries.

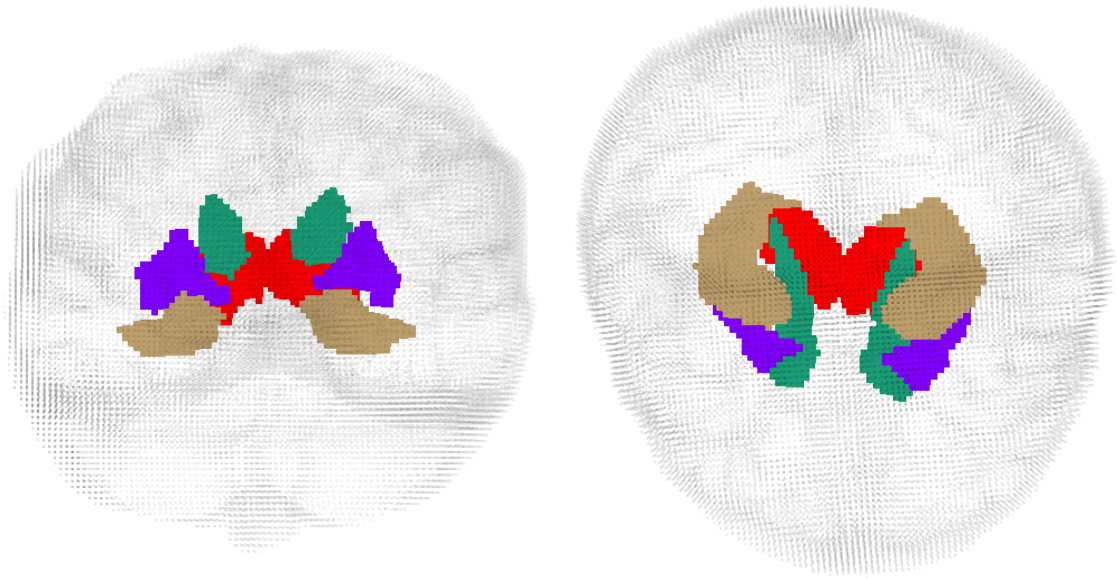

(a) **(b)**

Figure 5.1: (a) Front and (b) top views showing the four segmented gray matter substructures: caudate (green), hippocampus (sand), putamen (purple) and thalamus (red).

5.2.1.1 Material Models & Properties

Gray matter has been modeled as an isotropic material due to the randomly oriented cells forming the gray matter structure. Accordingly, linear-viscoelastic or hyper-viscoelastic constitutive laws were used in published computational studies of mTBI to represent gray matter (e.g. Kleiven [120], Taylor and Ford [136], Ganpule et al. [184]). Since we used a hyper-viscoelastic representation for gray matter in Chapter 3 (section 3.3), we continue using the same formulation, and assign material properties for each substructure. The hyper-viscoelastic model (Neo-Hookean with shear modulus represented by a Prony series) requires assigning the long-term shear modulus, relaxation times and Prony series constants (G_∞, τ_i and G_i or $g_i = \frac{G_i}{G_0}$, respectively where G_0 is the instantaneous shear modulus).

Elkin et al. [213] performed micro-indentation experiments on fresh porcine brain samples to extract the viscoelastic parameters required for a Prony series shear modulus representation. Regions tested were: hippocampus, dentate gyrus, cortex, thalamus, corona radiata, corpus callosum, brainstem and cerebellar gray and white matters. For our application, we used the thalamus and the average hippocampus material properties from Elkin et al. [213]; the parameters for the Prony series are shown in Table 5.1 (Note: in the study by Finan et al. [208] on human brains, only the hippocampus properties were presented and they are within the confidence interval drawn by both studies Finan et al. [208] and Elkin et al. [213]). For the remaining two substructures, caudate and putament, the parameters are adapted from the

work of Lee et al. [190]. Cortex, hippocampus and caudate/putamen of rat brains were characterized using micro-indentation tracked by Optical Coherence Tomography. Experimental indentation curves were used in a finite element model to estimate the material parameters for each region using different Poisson's ratios (ν= 0.35, 0.4, 0.45 and 0.49). Since the brain tissue is typically considered to be nearly incompressible (Pervin and Chen [51], Miller and Chinzei [69], Rashid et al. [74]), we used the material properties of the putamen and caudate obtained using Poisson's ratio of ν=0.49 (Table 5.1).

Note that, based on the available gray matter substructures characterization in literature, we have had to use material properties of multiple species (rats/murine and pigs/porcine). Nevertheless, the experimental work of Atay et al. [62] reported no difference between human and murine brains and Nicolle et al. [46] and Nicolle et al. [61] revealed no difference between human and porcine brain tissues.

The rest of the materials in the model (skull, CSF, other gray matter volumes, vasculature, falx, tentorium and white matter) are modeled exactly as in section 3.4.4 with the same material descriptions (constitutive laws and material parameters). Note for the homogeneous model, all gray matter regions (including the four segmented substructures) are assigned the gray matter material properties of section 3.4.4.

Table 5.1: Prony series shear modulus properties assigned to gray matter substructures which are adapted from published experimental studies.

	Properties	Reference
Hippocampus	G_∞=216 Pa, G_1=973.5 Pa, G_2=285 Pa, G_3=238.5 Pa, τ_1= 0.013 s, τ_2= 0.22 s and τ_3= 4.5 s	Elkin et al. [213]
Thalamus	G_∞=179 Pa, G_1=750 Pa, G_2=362 Pa, τ_1= 0.02 s and τ_2= 1.34 s	Elkin et al. [213]
Caudate/Putamen	G_∞=110 Pa, G_0=700 Pa, g_1= 0.61, g_2=0.135 , g_3=0.103 , τ_1=1.45 s, τ_2=10 s and τ_3=110 s	Lee et al. [190]

5.2.2 MPM Implementation

As in the previous two chapters, the segmented resolution of 0.8 mm (isotropic) is reduced down to 1.6 mm isotropic resolution with a cubic grid cell-size of 3.2 mm to cut down computational costs. Each cell typically has two particles in each direction. The two models (homogeneous vs heterogeneous gray matter) are simulated for the time of the loading profile using the same implementation as in section 3.4.3 (Uintah framework for MPM implementation).

5.2.3 Loading conditions

Results of the previous chapter (section 4.3.2.1) revealed that the cerebrum is affected (higher strains and injury predictions) the most when loaded in the axial direction. For this reason, we use the same loading condition of section 4.2.3 applied to the axial direction. The maximum acceleration of this loading curve is about 6000 rad/s^2 and the resultant rotation is about 3.4 degrees around the axial axis.

5.3 Results

The maximum value of Largest Principal Strain (LPS) for each structure is extracted at every 5 ms for the homogeneous and heterogeneous gray matter models (Figure 5.2). No differences are observed between the results from the two simulations.

However, there are differences between the substructures: Higher values of LPS are observed in the caudate followed by the hippocampus then the putamen and finally the thalamus. This ranking (of high strains between the four substructures) could be dependent on the applied loading direction.

We also investigate the differences between the two simulations in terms of maximum shear strains (Figure 5.3). Similar to LPS, results are nearly identical when comparing the maximum shear strains for all four structures in the two simulations (homogeneous and heterogeneous gray matter).

To our knowledge, the only gray matter injury threshold in the literature is that reported by Kleiven [120]. Based on National Football League reconstructed accidents, a value of 26% maximum principal strain was set as an injury predictor for gray matter. Using this threshold for our analysis, injury is only predicted in the caudate (of course, identically in both models). The same analogy of injury volume fraction in equation 4.1 is applied, and the predicted injured volume fraction of the caudate is about 1.2% in the two models. Figure 5.4 shows locations of injured material points in the caudate (red squares) (Injury locations are also identical in both models, homogeneous and heterogeneous gray matter). White matter injured material points are overlaid on the same volume (green triangles), and we observe that there is a cluster of injured white matter near the predicted injury in the caudate.

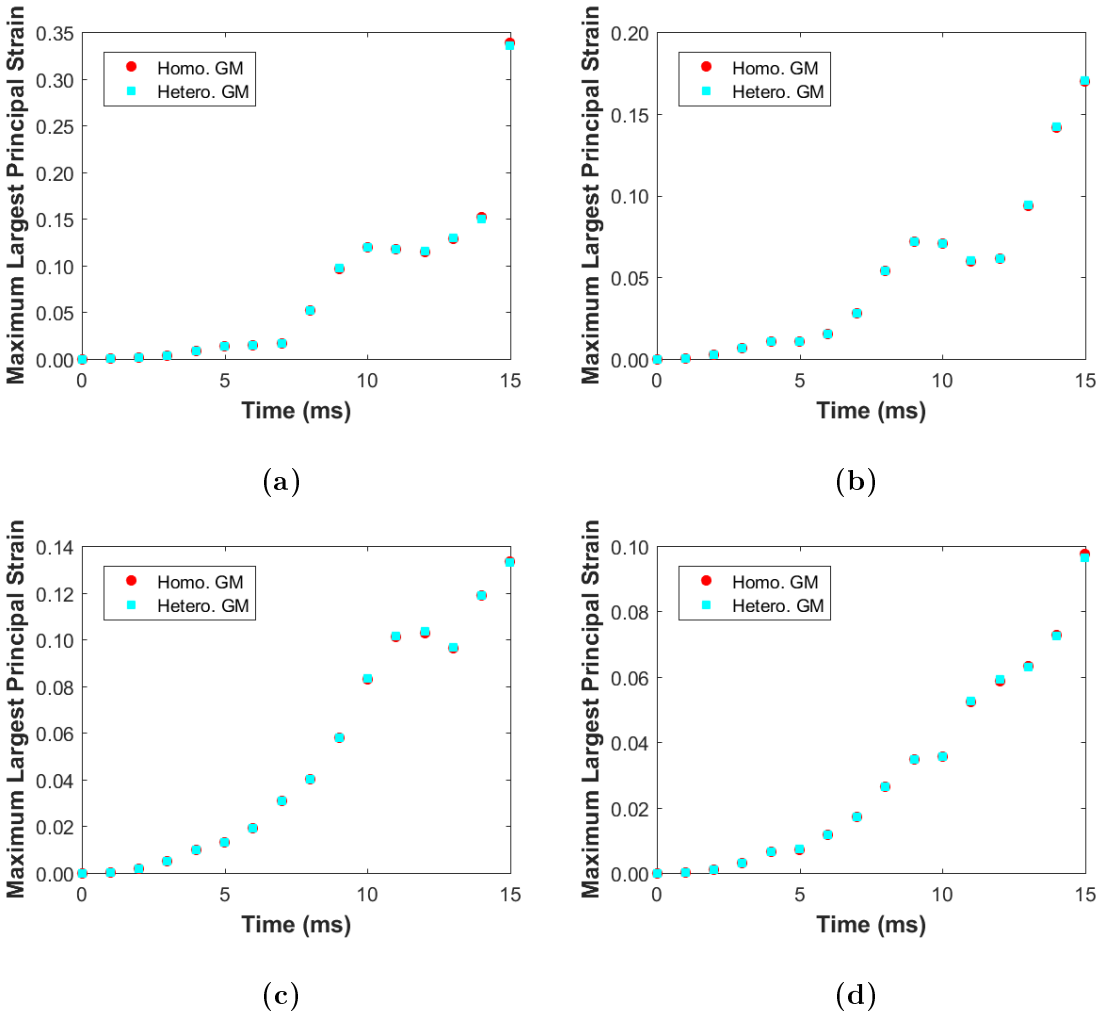

Figure 5.2: Maximum largest principal strain history for the (a) caudate (b) hippocampus (c) putamen and (d) thalamus extracted at every 5 ms for the two simulations (homogeneous vs heterogeneous gray matter). Clearly, there are no significant differences between the two models.

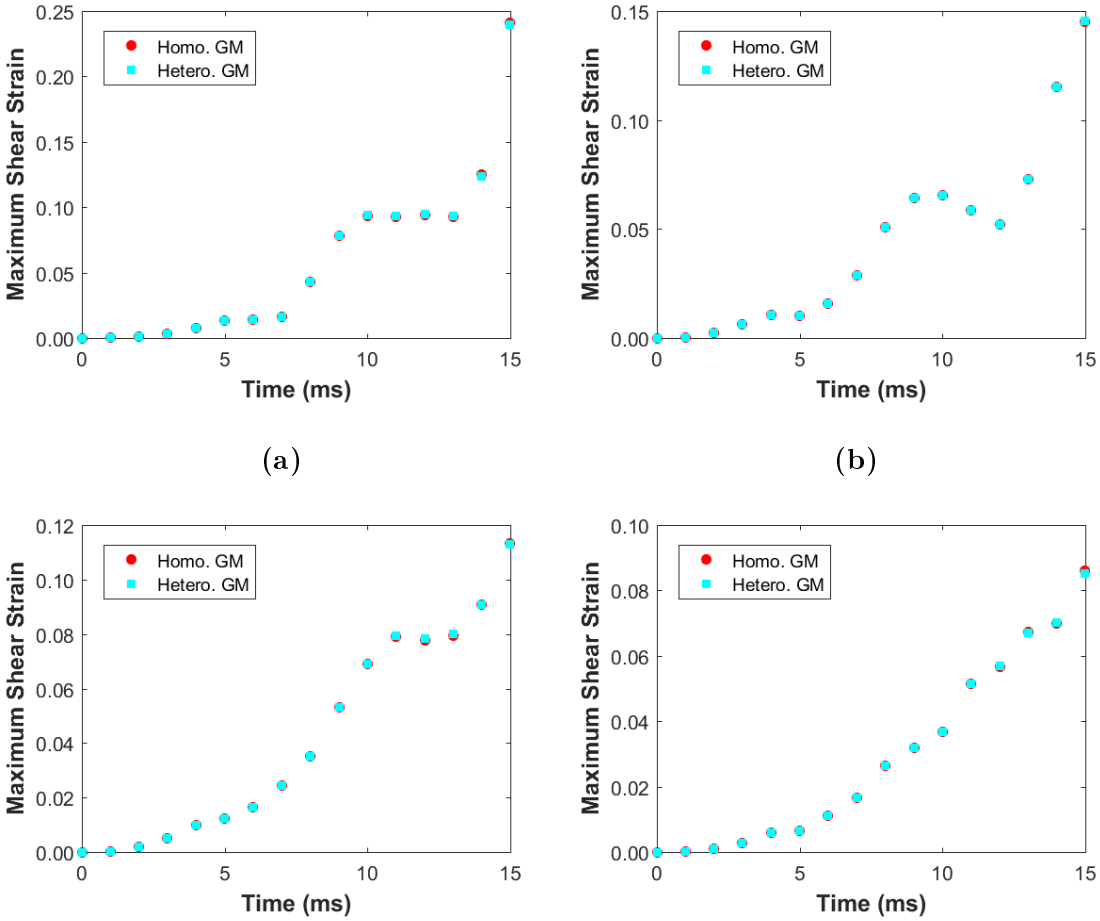

Figure 5.3: Maximum shear strain history for the (a) caudate (b) hippocampus (c) putamen and (d) thalamus extracted at every 5 ms for the two simulations (homogeneous vs heterogeneous gray matter). Results of the two models are identical.

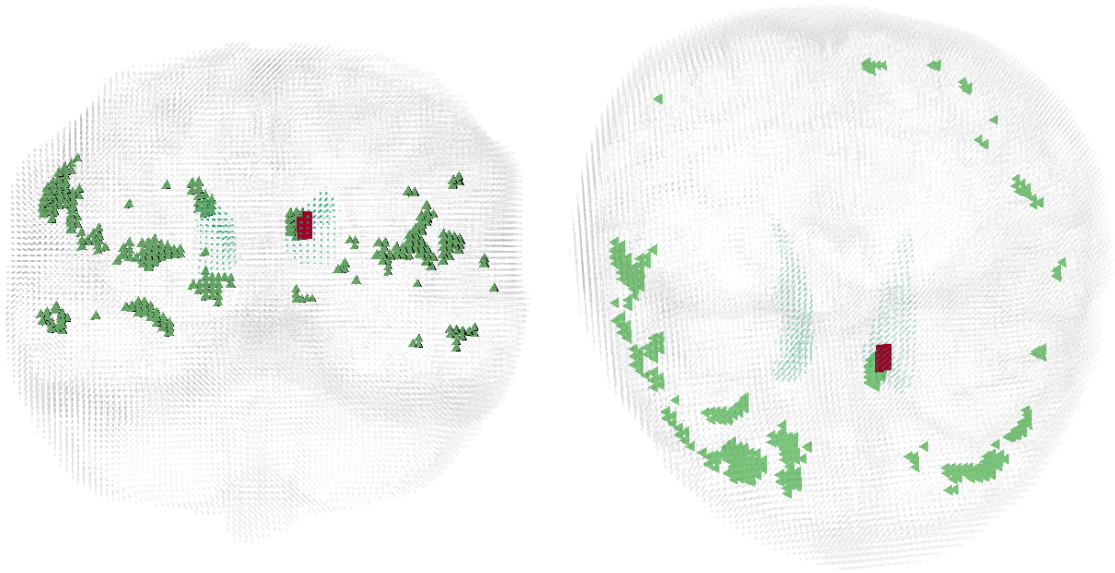

(a) **(b)**

Figure 5.4: Injury locations in the caudate (red squares) along with injury in cerebral white matter (green triangles) using largest principal strain as a predictor shown in two views: (a) front and (b) top. Notice that injury in the caudate neighbors white matter injury. The light green clouds represent the caudate material points.

5.4 Discussion

Both strain measures (largest principal strain and maximum shear strain) revealed the insignificance of accounting for gray matter heterogeneity in the predictions of strains, and eventually injury, in gray matter. Even the locations of maximum LPS are identical in the two models.

A possible reason for the observed identical response is that the shear modulus of gray matter substructures does not change greatly from one region to another (all values are of the same order of magnitude), which are confined by white matter (Long-term and short-term shear moduli for white matter are 286 and 1520 Pa, respectively). The minimum long-term shear modulus is in the caudate and putamen which has a value of G_∞=110 Pa while the maximum is in the cortical gray matter, G_∞=385 Pa (Hippocampus and thalamus have long-term shear moduli of 216 and 179 Pa, respectively). On the other hand, the instantaneous shear modulus is an order of magnitude higher for cortical gray matter, hippocampus and thalamus compared to the caudate and putamen (2750 Pa for cortical gray matter, 1291 Pa for hippocampus and thalamus compared to 700 Pa for caudate and putamen). Based on the low instantaneous shear modulus in the caudate and putamen, injury is expected in both. However, LPS exceeded the threshold of 26% in the caudate only (red squares in Figure 5.4). This obersvation might be related to overall high strains in the vicinity of the caudate as shown in Figure 5.4. Neighboring white matter (green triangles) exceeded the injury threshold of LPS$\geq$31% near the caudate predicted injury location. White matter injury predictions using LPS as a threshold could be an indicator of injury in neighboring gray matter. Note that more injurious cases must be studied to further investigate this hypothesis.

5.5 Summary & Conclusions

We developed two models one with homogeneous gray matter and another with five different regions of gray matter (heterogeneous): cortical and other sub-cortical gray matter (same properties as the homogeneous model), caudate, hippocampus, thalamus and putamen. The choice for the resolved gray matter substructures was based on available tissue characterization in literature. An injurious loading is applied to both models and injury is considered using a Largest Principal Strain (LPS) threshold of 26% from the work by Kleiven [120]. From the results of the simulations we conclude the following:

- Assigning experimental material properties for different gray matter substructures did not affect the deformation or injury predictions within these regions.
- For the currently available gray matter properties and thresholds in literature, heterogeneous modelling of gray matter is not necessary in mTBI predictions.

Chapter 6

Summary & Future Directions

The role of anisotropy and multiple aspects of brain heterogeneity was investigated throughout this work. The computational modelling approach allowed studying the effects of each source of heterogeneity separately. Major remarks will be concluded in the next section with a summary of the covered brain heterogeneity effects in mTBI in this work. Suggestions for future directions will follow in a separate section.

6.1 Concluding Remarks

In this work we used computational tools to examine the effects of the following:*

- White matter shear anisotropy.
- The addition of arterial network to head models of mTBI.

*For data archives, please refer to Appendix C

- Applied loading direction.
- Gray matter heterogeneity.

Except for gray matter heterogeneity, all of the other aspects have been shown to be significant in terms of injury predictions. Further, common injury locations at the borders of white and gray matter are captured in all of our models (2D model, 3D model with vasculature and 3D model without vasculature).

The length scales we currently incorporated in the full 3D head model are shown in Figure 6.1. Resolved anatomy is highlighted with the red box, while the green box identifies length scales incorporated in the material model. The influence of arterioles and capillaries is essentially incorporated in the homogenized white and gray matter properties.

Our model is highly sophisticated in terms of anatomical details. Structures resolved in the current 3D head model are: skull, CSF, ventricles, falx, tentorium, cerebral white and gray matters, cerebellar white and gray matters, brainstem and arteries. The resolution of the model is 1.6 mm in all directions which can be increased once computational capabilities advance in the next few years. The tractography information in Chapter 4 adds another level of anatomical sophistication. Not only overall white matter injury can be predicted, but also injury in each tract, which provides a more anatomically related location of injury (providing the ability to predict possible cognitive impairment related to each tract).

Injury vulnerability of white matter based on the loading direction is investigated in Chapter 4. Two injury criteria are used, Largest Principal Strain (LPS) and axonal strain. Each resulted in different locations of predicted injury which raises the question of which threshold we should use in mTBI predictions. Mainly, the choice of the LPS was due to the need for results comparisons with other models in the literature which modeled white matter as an isotropic material. On the other hand, the axonal strain couples the cellular mechanisms of injury with the tissue strains.

Ultimately, mTBI events should be captured and reconstructed to provide loading conditions for computational analysis and an acute diagnosis and symptoms of the injured persons must be documented. Based on these two components, simulations can be performed and injury criteria that result in predictions closer to reality (corresponds better with the symptoms experienced by the injured subject) can be identified. Although we can argue that axonal injury is related to the cellular function of the material, we can not conclude yet which injury criteria is the best or should be used in future mTBI computations due to the lack of such well documented injurious cases.

6.1.1 Summary of brain heterogeneity effects in mTBI

In chapter 2, we developed a material model for white matter that captures tension and shear anisotropy. Such a model has not been used before for mTBI predictions. We used the axonal injury criterion to predict white matter injury which is an indi-

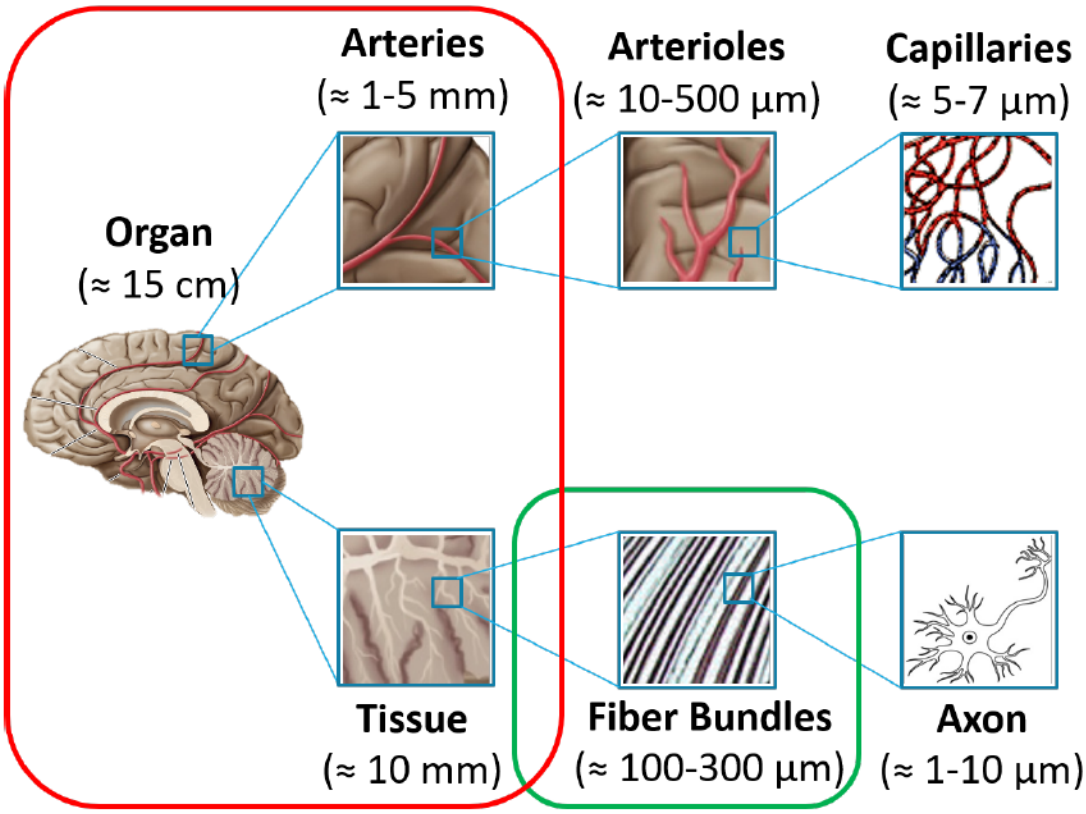

Figure 6.1: An ellustration for the incorporated length scales in our model. The red box encloses the actual anatomy resolved in the model, while the green box enclosed the fiber bundles which are incorporated in the material model and the injury criterion. Organ schematic is adapted from Huettel et al. [5].

cator of Diffuse Axonal Injury (DAI) in three 2D representative slides of the head. Comparing the results of our shear anisotropic model with another model that does not account for shear anisotropy, we observed higher levels of injury in the shear anisotropic model. Therefore, shear anisotropy of white matter has a significant impact on the predicted injury of mTBI.

Chapters 3 and 4 explored the effects of adding the vasculature network to 3D head models. Maximum principal strain and radial circumferential strain distributions showed statistically significant differences (p-value$<$0.00001) between the two models, with and without vasculature. Moreover, locations of maxima for both measures differed between the two models. The existence of the stiff vasculature network shifted the locations of maximum strains (and predicted injury) and resulted in new locations of injury and/or high strains. Therefore, including the vasculature network in computational models of mTBI is important. Further, in Chapter 4 we showed how the degree of injury changes when the loading direction is changed. The morphology of each white matter structure and the axis of rotation are the two factors affecting the predicted injury level with respect to loading direction (Axial rotation resulted in higher degree of injury in the cerebrum while coronal rotation induced higher levels of injury in the cerebellum and the brainstem). Using the TRACULA method, some white matter tracts are segmented and the degree of injury in each tract is calculated for each loading direction. Injury levels in white matter tracts per loading direction agreed with the results obtained for the whole white matter volume. The results of white matter vulnerability to injury based on the applied loading direction can be used in the diagnosis of mTBI at the acute stage of injury or to further enhance safety designs (e.g: helmets or automobile designing).

The effects of gray matter heterogeneity is investigated in Chapter 5. No significant differences are observed in the predicted injury (neither in the degree of injury

nor in the predicted locations of injury).

We conclude from this work that the addition of white matter shear anisotropy and the structure of arterial network play an important role in injury predictions. Consequently, both must be incorporated in safety designs, either in the automotive industry (car, seatbelt or airbag design), sports (helmet designing or game rules) or army applications (helmets). Similarly, our results on white matter susceptibility to injury based on the loading direction may be useful in some sports by adding new rules to eliminate, or at least decrease, occurrences of the most injurious loading scenarios. Locations of predicted injury can also be used clinically as an initial prediction of cognitive deficits and a starting point for targeted drug delivery (pharmaceutical treatment) or localized brain stimulation.

6.2 Future Directions

Our methods can be further enhanced to better represent the mechanics and deformations of soft tissues or further improve the ability of mTBI injury predictions as follows:

- The shear anisotropic model introduced in Chapter 2 can be incorporated in a 3D study to further explore the extent of shear anisotropy effects on injury predictions. The 3D modelling will showcase a more realistic fiber network and brain deformation which can be directly related to mTBI observations in the

whole head instead of selected slices.

- The shear anisotropic model can be extended to account for fiber dispersion and/or more than one family of fibers. In reality, the fiber network in the brain have many crossing fibers. The addition of fiber dispersion will provide better information about how anisotropic the white matter is at each material point. This information is directly related to the fractional anisotropy in DTI and hence can be extracted along with the primary fiber direction. Adding another family of fibers is harder than introducing fiber dispersion. The addition of a second family of fibers requires the information of the families to be readily available from medical imaging and the appropriate experiments to extract the material parameters needed for the model. To date, there are no reports in the literature that characterize brain tissue with crossing fibers.

- The 3D full head model with vasculature can be further enhanced in terms of anatomical details. The addition of the venous network, for example, will provide an extra level of sophistication. The reason behind leaving out the venous network in our model is the difficulty in segmenting the venous system separately. The Time Of Flight (TOF) technique we used to segment arteries in our work is a non-invasive method that captures the fast moving flow inside the arteries using MRI. The use of other techniques like X-ray based Angiograms could help in segmenting the venous system, however it requires the administration of an iodine-based dye to track blood flow.

- The material model we used for the arteries in Chapters 3, 4 and 5 is an isotropic hyperelastic model fitted to the experimental work by Monson et al. [11]. The material parameters obtained based on those tensile experiments are technically representative of the tissue response in that direction only (tensile loading along the length of artery » axial response). More experiments were performed by the same group a few years later to incorporate source and size effects (Monson et al. [215]) and the biaxial response of arteries (Monson et al. [216]). These three factors can also be incorporated in the constitutive model for arteries in the future.

- A well controlled animal study can provide a higher level of confidence in the solution method and predicted locations of injury. This can be achieved by comparing the experimental results from the animal study to a corresponding computational model. If the predictions of the computational model match the experimental observation, the length scale associated with the resolution can be used as an input for human studies. Also, if the injury hot spots are captured in the model including single material point injuries, we will provide prove that these single material point injury predictions are not due to numerical locking.

- Last but not least, the 3D head model developed in this work to predict damage in white and gray matters can further be extended to account for blood flow changes. The extension requires a model for the brain tissue that couples the brain deformation with the blood flow in the brain. One possibility is to use

the biphasic theory to couple brain deformation (solid phase) with the blood flow (liquid phase), which has been applied before to model soft tissue in the literature (e.g.: Mow et al. [217], Spilker and Suh [218] and Cohen et al. [219]). We developed a theoretical framework for the biphasic theory application to couple brain deformation and blood flow, details of which are presented in Appendix B.

Appendix A

MPM Implementation Using The Uintah Computational Framework

In this appendix, we will develope a simple guide to use the Uintah computational framework for the MPM implementation used in our work. First, the steps required to build/install Uintah* will be described. Then, the process of submitting an input file will be explained. Finally, post-processing the output of Uintah using VisIt and MATLAB softwares will be briefly discussed. For further details about Uintah, the reader is referred to the original documentation at:

https://www.sci.utah.edu/publications/SCITechReports/UUSCI-2009-007.pdf.

*http://uintah.utah.edu/

A.1 Building Uintah

The source file of Uintah can be downloaded from the University of Utah Uintah web-page: http://uintah.utah.edu/. The size of our simulations is relatively large (we used 24 nodes, each is Intel Haswell dual socket with 12-core processors, 2.5GHz, 30MB cache and 128GB RAM). Move (e.g.: using WinSCP software) the downloaded source file to the computational cluster (we used the Maryland Advanced Research Computing Center (MARCC)), and follow these steps:

- Unzip the source code using: tar xvf code.tar
- Move inside the unzipped folder (the name might be different than what we show here): cd JHUUintah_SVN_brain
- Move to the "build" directory (if it does not exist, create it): cd build
- Load the following module to use it for installing Uintah (if it does not exist, request it from your computing cluster admin team): module load cmake
- Load VisIt module to configure VisIt for post-processing (if it does not exist, request it from your computing cluster admin team). Note you should use the version number available on your computing cluster, the number here is an example): module load visit/2.9.1
- Load intel (use the version available on your computing cluster, the number shown here is an example): module load intel/18.0

- Configure VisIt and Intel (change the paths for openmpi and VisIt based on your computing cluster paths): ../JHUUintah_SVN_brain/src/configure -enable-64bit –without-fortran –enable-optimize=-O3

  -with-mpi=pathTo/openmpi/intel/18.0 CC=icc CXX=icpc

  –no-create –no-recursion –with-visit=pathTo/visit/2.9.1

- Build Uinath using the command: make all -j 4

If no errors appeared (e.g: due to wrong module version number and/or folder or file paths), Uintah is built and ready to be used.

A.2 Uintah Simulations: Basics

Once Uintah is installed, jobs can be submitted. For our application, the material points have specific locations in space (as extracted from the Magnetic Resonance Imaging (MRI) volume). Each structure should have a separate file with three columns representing the structure's xyz coordinates (based on it's unique intensity value in the segmented MRI). The points files must have the extension "pts" (e.g.: CSF.pts). Assigning points in space requires a pre-processing step to divide all material points in space into smaller subsets assigned to each processor using the following command (pfs) executed in the same directory where your input file is located on the cluster (Note: change paths to openmpi and StandAlone/tools/pfs/pfs based on their location on your cluster):

```
/software/apps/mpi/openmpi/3.1/intel/18.0/bin/mpirun /scratch/groups/
    kramesh1/Fatma/UintahNew/JHUUintah_SVN_brain/build/StandAlone/tools/
    pfs/pfs Input.ups
```

Listing A.1: Preprocessing an input file using pfs command

Then, you can submit the input file using the sus executable located in the "StandAlone" directory inside the "build" directory created in the previous section (i.e.: build/StandAlone/sus) as follows (Note: change paths to openmpi and StandAlone/-sus based on their location on your cluster):

```
/software/apps/mpi/openmpi/3.1/intel/18.0/bin/mpirun /scratch/groups/
    kramesh1/Fatma/UintahNew/JHUUintah_SVN_brain/build/StandAlone/sus
    Input.ups
```

Listing A.2: Submitting an input file using sus command

A simple script to run the above two steps (preprocessing using pfs and submitting the job using sus commands) have the following form:

```
#!/bin/bash -l
#SBATCH
#SBATCH --job-name=NameIt
#SBATCH --time=28:00:00
#SBATCH --nodes=5
#SBATCH --ntasks-per-node=24
```

```
#SBATCH --partition=parallel
#SBATCH --mail-type=end
#SBATCH --mail-user=email@jhu.edu
module load intel/18.0
/software/apps/mpi/openmpi/3.1/intel/18.0/bin/mpirun /scratch/groups/
    kramesh1/Fatma/UintahNew/JHUUintah_SVN_brain/build/StandAlone/tools/
    pfs/pfs Input.ups
/software/apps/mpi/openmpi/3.1/intel/18.0/bin/mpirun /scratch/groups/
    kramesh1/Fatma/UintahNew/JHUUintah_SVN_brain/build/StandAlone/sus
    Input.ups
```

Listing A.3: A simple script combining preprocessing and submitting an input file

In the above code, five nodes with twenty four processors each (totaling 120 processors) are requested for twenty eight hours to run the two steps: preprocessing and submitting the input file. Specifications of the input file are defined in the Uintah documentation mentioned at the beginning of this section.

A.3 Post-processing Uintah Output Using VisIt and MATLAB

Uintah outputs the database in a folder commonly referred to as the "uda" directory, which contains the original input file, points files, check points folder (if any), requested time-steps folders and other outputs depending on the specifications in the

original input file. Download the whole "uda" directory from the computing cluster into your machine and open the *index.xml* file in VisIt (which is an open source software provided by the Lawrence Livermore National Laboratory[†]). We will explain how to perform three main tasks in VisIt: Plot the structure, write expressions and export the database and how to further post-process VisIt output database using MATLAB.

A.3.1 How to Plot the Structure

Open the *index.xml* file in VisIt (File > Open File OR Under "Sources" section click on: Open) and follow these steps:

1. Under the "Plots" section, Click on: Add > Pseudocolor > p.color

2. Select * to plot the whole structure using a single color or pick the structure/-material number you want to plot.

3. Under the "Plots" section, Click on: Draw. Your selected structure should appear in the active window and a corresponding item appears in the plot lists (e.g.: if you plot structure/material # 1, in the plot list you will see an item named Pseudocolor-p.color/1).

4. To change the color of the plotted structure, double click on the structure's

[†]VisIt can be downloaded here: https://wci.llnl.gov/simulation/computer-codes/visit/downloads

item under the "Plot" list. The "Pseudocolor Plot Attributes" window should appear. Under the Data tab, choose a color from the color table and click Apply. You can also change Opacity in the same tab. Make sure to click Apply after you change any attribute and click Dismiss when you are done.

5. To change the the size of the material points, double click on the structure's item under the "Plot" list. The "Pseudocolor Plot Attributes" window should appear.Under the Geometry tab, change "Point size (pixels)" to the desired size and click Apply then Dismiss.

6. You can add as much items as you like and you can use the "Hide/Show" button under the "Plots" section to hide or show any item in the list.

A.3.2 How to Write Expressions

Uintah has a limited number of variables you can extract at each time step. Principal strain vector, for example, is not available. However, you can use VisIt to write the equations (VisIt refers to them as expressions) needed to calculate the desired output. Here is an example of how to calculate the principal strain vector assuming you requested the deformation gradient of the particle in your input file:

1. From the top bar menu, click on: Controls > Expressions. The Expressions window should open. All the steps below are performed in this window.

2. Click on: New. First, we must calculate the Lagrangian strain. On the right

side under the Definition list in the "Name" field write: E (or any name you prefer). In the "Type" field, choose "Tensor Mesh Variable" from the drop-down menu. We know that Lagrangian strain $E = \frac{1}{2}(F^T F - I)$ where I is the identity tensor. Hence, under the Standard Editor Definition, write 0.5*(. Then to add the transpose function click on: Insert Function > Tensor > transpose. Your Definition now will look like: 0.5*(transpose(). To add the deformation gradient click on: Insert Variable > Tensors > p.deformationMeasure > *. The Definition will now be: 0.5*(transpose(<p.deformationMeasure/*>). Now multiply by the deformation gradient: 0.5* (transpose(<p.deformationMeasure/*>) *<p.deformationMeasure/*>. To create the identity tensor, You can use $F^{-1}F$. To get the inverse function, click on: Insert Function > Tensor > inverse. Follow the same steps to add the deformation gradient. Your final definition should look like: 0.5*(transpose(<p.deformationMeasure/*>) * <p.deformationMeasure/*> - inverse(<p.deformationMeasure/*>) *<p.deformationMeasure/*>).

3. To calculate the principal strains vector, click on: New. In the "Name" field, write: E_Principal (or any name you like). In the "Type" field, choose "Vector Mesh Variable" from the drop-down menu. Now click on: Insert Function > Tensor > principal_tensor. Under the Standard Editor Definition, principal_tensor() should appear. Put the cursor inside the bracket and then click: Insert Variable > Tensors > E (or the name you chose for the Lagrangian Strain Tensor created in the previous step).

4. To save the components of the principal strain vector separately, click: New. In the "Name" field, write: E_Principal_1 (or any name you like). In the "Type" field, choose "Scalar Mesh Variable" from the drop-down menu. Click on: Insert Variable > Vectors > E_Principal (or the name you choose for the principal strain vector in the previous step). Under the Standard Editor Definition, E_Principal should appear and write [0] next to it (Now it should read E_Principal[0]). Note: to save the second and third components follow the same steps but use [1] and [2] for the second and third components, respectively.

The expressions feature is very helpful in creating all the variables you want to extract for further post-processing.

A.3.3 How to Export Database

First you need to draw the variable you wish to extract. Follow the steps in section A.3.1 but instead of plotting p.color plot E_Principal_1, for example, created in the previous section. Then you can export the result by following these steps:

1. Click on: File > Export database. The Export Database window should open.

2. In the field "Directory name", write the full path to the folder you want to save the database in. If you do not recall the full path, click on the three dots button to choose a folder.

3. In the field "File name", write a name for the database you are extracting.

4. From the drop-down menu "Export to", choose XYZ. This format will export the current XYZ location of each material point in addition to the plotted variable.

5. You can add extra variables to the output database. Since we have multiple materials/structures in our model, it is useful to extract the color (which indicates the material number based on the order of the materials in your input file). To add the color, Click on: Add Variable > Scalars > p.color > *. Then Click Apply.

6. You can add as many variables as you like but make sure that the variables are all scalars (or vectors) but do not mix scalars and vectors, it will not output correctly. (Note: You can always use the expressions feature to convert vectors into scalars like what we did for the principal strain vector in the previous subsection). When you are done adding extra variables, click: Export. The generated file will have the extension ".xyz". The number of columns in this file is equal to the number of added variables plus four. The first three columns will be current XYZ locations, followed by the added variables in the same order you added them and then the plotted variable. There will be a column of question marks and some random text lines which we will remove in the next section using a MATLAB script.

A.3.4 MATLAB Post-processing

Further post-processing is probably needed after VisIt, and MATLAB is one of the most commonly used post-processing softwares, or languages, in the engineering field. The first step is to clean-up the xyz database file from text lines and question marks. The following code can be used for this purpose:

```
%Clean Up Visit Files from text lines and unwanted digits

clc
clear

%This line defines the suffix used for the timesteps you want to process
%You can change it to match your files
%You can automate the generation of this line too
time={'00','05','10','15','20','25','30','35','40'};

%Initial and end parts of the file name (change them accordingly)
fileinitial='E1_0';
fileend='.xyz';

for i=1:length(time)
filename=strcat(fileinitial,time{i},fileend);

S = fileread(filename);    %read as string
```

```
19 %remove question marks, "chunk" line and the line before "chunk" all
       together
20 newS = regexprep(S, {'[^\n]+\n[^\n]*chunk[^\n]*\n', '^\?'}, {'', ''}, '
       lineanchors');
21 %Save the cleaned file
22 fid = fopen(strcat('Clean/',fileinitial,time{i},'Clean',fileend), 'w');
23 fwrite(fid, newS);
24 fclose(fid);
25 end
```

Listing A.4: MATLAB script to clean-up VisIt XYZ files.

You can use this script to clean-up a single file by removing the "for" loop and directly write your file name inside the function fopen (line 16 in the script) and change the new (cleaned) file name (line 21 in the script) such that it reads: fid = fopen (yourNewFileName, 'w').

Another possible post-processing step is to extract Largest Principal Strain (LPS) (E_Principal_1 of section A.3.2), for example, for a specific structure and save the locations of LPS>0.31 (Injury threshold in our model). Also, let's plot the LPS distribution at time 15 ms. To do that you can use the following script:

```
1 clear
2 clc
3
4 %Suffix of XYZ files, in this case it is similar to the time vector t
5 time={'00','01','02','03','04','05','06','07','08','09','10',...
```

```
'11','12','13','14','15',};
t=0:15;

%Structure under investigation
% 8 Cerebrum, 9 Cerebellum, 20 Brainstem
structure=8;
if structure==8
name='Cbrm';
else if structure==9
name='Cblm';
else if structure==20
name='Bstem';
end
end
end

%Axial wBV
fileinitial='Axial/E1Clean/Eprinc1_0';
fileend='Clean.xyz';

%initialization
E1max31Axial=zeros(1,length(t));

for i=2:length(time)
filename=strcat(fileinitial,time{i},fileend);
```

```
data=load(filename);
%This file has eight columns, the first 3 are current XYZ
% Columns 4-6 are displacement in X, Y and Z, column 7
% is the material/structure number and column 8 is E_Principal_1
data(:,1)=data(:,1)+0.1228; %Un-Shift X if needed
data(:,2)=data(:,2)+0.0988; %Un-Shift Y if needed
data(:,3)=data(:,3)+0.0916; %Un-Shift Z if needed
%Restore reference position (X=x-dx)
data(:,1:3)=data(:,1:3)-data(:,5:7);
%Delete displacement data (dx)
data(:,5:7)=[];

%Extract data

indexAxial=find(data(:,4)==structure);
dataAxial=data(indexAxial,[1:3,5]);

%Percentage (Volume Fraction) and locations for E1>31%
indexPos=find(dataAxial(:,4)>0.31);
E1max31Axial(i)=length(indexPos)/length(indexAxial);
      if length(indexPos)>0
          AxialPosMax31X10=dataAxial(indexPos,1);
          AxialPosMax31Y10=dataAxial(indexPos,2);
          AxialPosMax31Z10=dataAxial(indexPos,3);
          filenameLoc=strcat('Axial/E1Clean/E1Locs/E1max31',name,time{i},
```

```
    '.txt');
56          All=[AxialPosMax31X10 AxialPosMax31Y10 AxialPosMax31Z10];
57          save(filenameLoc,'All','-ascii')
58      end
59
60 %Distribution at time 15
61 if (t(i)==15)
62 CbrmWMPosX15=dataAxial(indexPos,1);
63 CbrmWMPosY15=dataAxial(indexPos,2);
64 CbrmWMPosZ15=dataAxial(indexPos,3);
65 %save histogram data
66 [CbrmWMHistN15,CbrmWMEdges15]=histcounts(dataAxial(:,4));
67 end
68 end
69
70 figure(1)
71 centers=(CbrmWMEdges15(1:end-1)+CbrmWMEdges15(2:end))/2;
72 b=bar(centers,CbrmWMHistN15);
```

Listing A.5: MATLAB script to extract Largest Principal Strain (LPS) for a specific structure and save locations of LPS>0.31 in addition to plotting the LPS distribution at time 15 ms.

Of course there are plenty of ways to post-process VisIt databases. We introduced two examples here and you can apply the concept for other post-processing needs.

Appendix B

A Biphasic Theoretical Framework to Couple Brain Deformation with Cerebral Blood Flow in mTBI

Changes in Cerebral Blood Flow (CBF) have been observed and characterized in severe TBI (Martin et al. [220], Bouma et al. [221]). Martin et al. [220] closely monitored patients with severe closed head injury from day 0 (day of injury) to day 15 post injury in multiple University of California at Los Angeles Medical Centers. Right after injury, a decrease in CBF during day 0 followed by hyperemia (increase in blood supply to the brain) during days 1-3 post injury was observed. The following days (4-15) post injury, cerebral vasospasm (increase in blood velocity inside arteries with overall decreased blood supply to the brain) was recorded. Animal studies

reported a decrease in CBF during the first twenty four hours post injury (Clevenger et al. [222], Immonen et al. [223]). A similar scenario, but at a lower level, may occur after mTBI. However, to date, none of the efforts in literature established a framework to theoretically couple the blood flow with the brain deformation.

Recall from section 1.4.2.1, the biphasic theory has been used to model the Cerebro-Spinal Fluid (CSF) diffusion in the brain tissue during deformation (Cheng and Bilston [99], Basser [100]). Also, it has been used for modelling drug delivery into the nervous tissue (Chen and Sarntinoranont [224]). In this appendix, we introduce, for the first time in the literature, a biphasic theoretical framework to predict CBF changes by coupling CBF and brain deformation.

B.1 Derivation of the Constitutive Equations: The Biphasic Theory

The biphasic theory for soft tissues was first introduced by Mow et al. [217] to model the human articular cartilage by utilizing the mixture theory of Craine et al. [225] and Green and Naghdi [226]. In this section, we utilize the work of Mow et al. [217] to derive the coupling between the brain tissue and CBF. Subscripts s and f will be used for the solid (brain tissue) and fluid (blood) phases, respectively. We begin with the following assumptions:

- Both phases exist at each material point $\Rightarrow$ iso strain case ($\varepsilon = \varepsilon_s = \varepsilon_f$ and

$\sigma = \sigma_s + \sigma_f$).

- For simplicity, we assume that the solid phase is a linear elastic solid which has the following constitutive relation:

$$\sigma_{\mathbf{s}} = \lambda_s \mathrm{tr}(\varepsilon)\mathbf{I} + 2\mu_s \varepsilon \tag{B.1}$$

where λ_s and μ_s are the lamé constant and shear modulus of the solid phase, respectively.

- The fluid phase is assumed to be an incompressible, isotropic, Newtonian fluid which has the following constitutive relation:

$$\sigma_{\mathbf{f}} = -p\mathbf{I} + 2\mu_f \dot{\varepsilon} \tag{B.2}$$

where p and μ_f are the hydrostatic pressure and viscosity of the fluid phase, respectively.

The volume is preserved ($V = V_f + V_s$) and the bulk densities, ρ_i of both phases are defined as

$$\rho_s = \frac{m_s}{V} \text{ and } \rho_f = \frac{m_f}{V} \tag{B.3}$$

where m_i is the mass of each constituent. The density of the mixture is given by

$$\rho = \rho_s + \rho_f. \tag{B.4}$$

Further, we define the body force per unit mass for the mixture ($\mathbf{F^b}$) as

$$\rho \mathbf{F^b} = \rho_s \mathbf{F_s^b} + \rho_f \mathbf{F_f^b} \tag{B.5}$$

and the velocity of the mixture ($\mathbf{v}$) as

$$\rho\mathbf{v} = \rho_s\mathbf{v_s} + \rho_f\mathbf{v_f}. \tag{B.6}$$

To calculate the local equations of motion for each constituent, we use the balance of linear momentum

$$\rho_s\frac{\partial\mathbf{v_s}}{\partial t} = \nabla.\sigma_\mathbf{s} + \rho_s\mathbf{F_s^b} + \mathbf{F_i} \tag{B.7}$$

and

$$\rho_f\frac{\partial\mathbf{v_f}}{\partial t} = \nabla.\sigma_\mathbf{f} + \rho_f\mathbf{F_f^b} + \mathbf{F_i} \tag{B.8}$$

where $\mathbf{F_i}$ is the interaction force between the solid and fluid phases and the mixture's linear momentum is the sum of equations B.7 and B.8 as

$$\rho\frac{\partial\mathbf{v}}{\partial t} = \nabla.\sigma + \rho\mathbf{F^b}. \tag{B.9}$$

Since velocities between constituents differ, the interaction force can be assumed to be a drag force which is defined as

$$\mathbf{F_i} = \frac{1}{k}(\mathbf{v_f} - \mathbf{v_s}) \tag{B.10}$$

where k is the coefficient of permeability. In geo-materials literature(e.g.: Srivastava et al. [227], Bogdanov et al. [228], Selvadurai and Głowacki [229]), the permeability coefficient is related to the change in pressure and the volumetric flow rate by Darcy's law (Whitaker [230])

$$Q = -\frac{k}{\mu}\nabla P \tag{B.11}$$

where Q is the volumetric flow rate and ∇P is the change in pressure per unit length. The blood flow in the arteries has been modeled in the literature using Poiseuille's Law (Sumpio [231], Ku and Zhu [232]) which is of the form

$$\Delta P = \frac{8\mu L Q}{\pi r^4} \tag{B.12}$$

where ΔP is the change in pressure, Q is the volumetric flow, μ is the dynamic viscosity, L is the length of the blood vessel and r is the radius of the blood vessel. This model assumes that the blood flow is laminar and the blood vessel size is constant. Rearranging equation B.12 to

$$\nabla P = \frac{\Delta P}{L} = \frac{8\mu}{\pi r^4} Q \tag{B.13}$$

results in a form similar to equation B.11. Hence, by comparing equations B.11 and B.13, the permeability, k, can be calculated as

$$k = \frac{\pi r^4}{8\mu}. \tag{B.14}$$

Substituting the strain-displacement ($\varepsilon_s = \frac{1}{2}(\nabla \mathbf{u_s} + \nabla^T \mathbf{u_s})$), strain rate-velocity ($\dot{\varepsilon_f} = \frac{1}{2}(\nabla \mathbf{v_f} + \nabla^T \mathbf{v_f})$) and displacement-velocity ($\mathbf{v} = \frac{\partial \mathbf{u_s}}{\partial t}$) relationships into equations B.1 and B.2 and then substitute the stresses into the linear momentum (equations B.7 and B.8)

$$\rho_s \frac{\partial^2 \mathbf{u_s}}{\partial t^2} = (\lambda + \mu_s)\nabla(\nabla . \mathbf{u_s}) + \mu_s \nabla^2 \mathbf{u_s} + \rho_s \mathbf{F_s^b} + \frac{1}{k}\big(\mathbf{v_f} - \frac{\partial \mathbf{u_s}}{\partial t}\big) \tag{B.15}$$

$$\rho_f \frac{\partial \mathbf{v_f}}{\partial t} = -\nabla p + \mu_f \nabla(\nabla . \mathbf{v_f}) + \mu_f \nabla^2 \mathbf{v_f} + \rho_f \mathbf{F_f^b} - \frac{1}{k}\big(\mathbf{v_f} - \frac{\partial \mathbf{u_s}}{\partial t}\big) \tag{B.16}$$

which is equivalent to the Navier-Stoke's equation derived for each constituent. Since we assumed that the fluid phase is incompressible,

$$\nabla.\mathbf{v_f} = 0 \tag{B.17}$$

which reduces equation B.16 to

$$\rho_f \frac{\partial \mathbf{v_f}}{\partial t} = -\nabla p + \mu_f \nabla^2 \mathbf{v_f} + \rho_f \mathbf{F_f^b} - \frac{1}{k}\left(\mathbf{v_f} - \frac{\partial \mathbf{u_s}}{\partial t}\right) \tag{B.18}$$

Furthermore, to simplify the coupling between the linear momentum equation, we assume that the fluid velocity is much larger than the solid velocity ($\mathbf{v_f} >> \mathbf{v_s} = \frac{\partial \mathbf{u_s}}{\partial t} \Rightarrow \left(\mathbf{v_f} - \frac{\partial \mathbf{u_s}}{\partial t}\right) \approx \mathbf{v_f}$) and that the body forces can be neglected. Equations B.15 and B.18 further reduced to

$$\rho_s \frac{\partial^2 \mathbf{u_s}}{\partial t^2} = (\lambda + \mu_s)\nabla(\nabla.\mathbf{u_s}) + \mu_s \nabla^2 \mathbf{u_s} + \frac{1}{k}\mathbf{v_f} \tag{B.19}$$

$$\rho_f \frac{\partial \mathbf{v_f}}{\partial t} = -\nabla p + \mu_f \nabla^2 \mathbf{v_f} - \frac{1}{k}\mathbf{v_f} \tag{B.20}$$

Hence, equations B.14 and B.20 can be used to solve for the fluid phase velocity which is then substituted into equation B.19 to solve for the solid phase displacement (we will talk about the radius r of equation B.14 in the next section).

B.2 Application Challenges

There are several challenges in the biphasic theory application for the Cerebral Blood Flow (CBF) alteration predictions. First, to calculate the permeability (equation

B.14) the radius of the blood vessel should be defined. Under the assumption that both phases exist at each material point, there is no clear definition for the radius r. Therefore, an "equivalent radius" ($r_{equiv.}$) for the arterial network must be defined for the calculation of the permeability.

The second challenge arises from the requirement of an initial condition to solve for the fluid phase velocity in equation B.20. The normal blood supply to the human brain is approximately 750 milliliter per minute (or $12.5\times10^{-}6$ cubic meter per second) which represents the volume flow rate (Q_{rest}) at rest (Lassen [233], Kety and Schmidt [234]). If the equivalent radius is defined, the initial velocity magnitude (at rest) can be derived from Q_{rest} as follows

$$Q_{rest} = A||\mathbf{v_{f0}}|| \text{ where } A = \pi r_{equiv.}^2 \Rightarrow ||\mathbf{v_{f0}}|| = \frac{Q_{rest}}{\pi r_{equiv.}^2} \tag{B.21}$$

Nevertheless, traumatic injuries rarely occur when the person is at rest. Estimation of CBF for other than rest status is not trivial. Multiple factors contribute to the CBF during exercise, for example, which are either chemical, cardiovascular, metabolic or neural innervation factors (Querido and Sheel [235]). Moreover, determining the direction of the velocity is not trivial either.

Although the application of biphasic theory to predict changes in CBF is very challenging, future advances in medical research and CBF monitoring might open new doors for this application.

Appendix C

Data Archives

Data in this work is located in the Ramesh Lab Craedl* account under the brain injury biomechanics project as follows:

- Shear Anisotropy Study (including validation, Chapter 2): https://ramesh-lab.craedl.org/directory/3312/.
- Vasculature Effect Study: Validation (Chapter 3): https://ramesh-lab.craedl.org/directory/3335/.
- Vascualture Effect Study: Non-Injurious Study (Chapter 3): https://ramesh-lab.craedl.org/directory/3322/.
- Vascualture Effect Study: Injurious Study (Chapter 4): https://ramesh-lab.craedl.org/directory/3323/.

*https://ramesh-lab.craedl.org/.

- Loading Direction Study (Chapter 4): https://ramesh-lab.craedl.org/directory/3328/.
- Gray Matter Heterogeneity Study (Chapter 5): https://ramesh-lab.craedl.org/directory/3332/.

Bibliography

[1] F. Velardi, F. Fraternali, and M. Angelillo. Anisotropic constitutive equations and experimental tensile behavior of brain tissue. *Biomechanics and Modeling in Mechanobiology*, 5(1):53–61, 2006. ISSN 1617-7959. doi: 10.1007/s10237-005-0009-9.

[2] X. Jin, F. Zhu, H. J. Mao, M. Shen, and K. H. Yang. A comprehensive experimental study on material properties of human brain tissue. *Journal of Biomechanics*, 46(16):2795–2801, 2013. ISSN 0021-9290. doi: 10.1016/j.jbiomech.2013.09.001.

[3] R. M. Wright, A. Post, B. Hoshizaki, and K. T. Ramesh. A multiscale computational approach to estimating axonal damage under inertial loading of the head. *Journal of Neurotrauma*, 30(2):102–118, 2013. ISSN 0897-7151. doi: 10.1089/neu.2012.2418.

[4] Andrew K Knutsen, Elizabeth Magrath, Julie E McEntee, Fangxu Xing, Jerry L Prince, Philip V Bayly, John A Butman, and Dzung L Pham. Improved mea-

surement of brain deformation during mild head acceleration using a novel tagged mri sequence. *Journal of biomechanics*, 47(14):3475–3481, 2014. ISSN 0021-9290.

[5] Scott A Huettel, Allen W Song, and Gregory McCarthy. *Functional magnetic resonance imaging*, volume 1. Sinauer Associates Sunderland, MA, 2004.

[6] D. F. Meaney, B. Morrison, and C. D. Bass. The mechanics of traumatic brain injury: A review of what we know and what we need to know for reducing its societal burden. *Journal of Biomechanical Engineering-Transactions of the Asme*, 136(2):14, 2014. ISSN 0148-0731. doi: 10.1115/1.4026364. URL <GotoISI>://WOS:000332483700008.

[7] Simon Chatelin, Andre Constantinesco, and Remy Willinger. Fifty years of brain tissue mechanical testing: From in vitro to in vivo investigations. *Biorheology*, 47(5-6):255–276, 2010. ISSN 0006-355X. doi: 10.3233/bir-2010-0576. URL <GotoISI>://WOS:000288321700001.

[8] Elisha S Gurdjian, VL Roberts, and L Murray Thomas. Tolerance curves of acceleration and intracranial pressure and protective index in experimental head injury. *Journal of Trauma and Acute Care Surgery*, 6(5):600–604, 1966. ISSN 2163-0755.

[9] Richard M Greenwald, Joseph T Gwin, Jeffrey J Chu, and Joseph J Crisco.

Head impact severity measures for evaluating mild traumatic brain injury risk exposure. *Neurosurgery*, 62(4):789–798, 2008. ISSN 0148-396X.

[10] Deva Chan, Andrew K. Knutsen, Yuan-Chiao Lu, Sarah H. Yang, Elizabeth Magrath, Wen-Tung Wang, Philip V. Bayly, John A. Butman, and Dzung L. Pham. Statistical characterization of human brain deformation during mild angular acceleration measured in vivo by tagged MRI. *Journal of Biomechanical Engineering*, 2018. ISSN 0148-0731. doi: 10.1115/1.4040230. URL http://dx.doi.org/10.1115/1.4040230.

[11] K. L. Monson, W. Goldsmith, N. M. Barbaro, and G. T. Manley. Axial mechanical properties of fresh human cerebral blood vessels. *Journal of Biomechanical Engineering-Transactions of the Asme*, 125(2):288–294, 2003. ISSN 0148-0731. doi: 10.1115/1.1554412. URL <GotoISI>://WOS:000182725900016.

[12] Jiwon Ryu, Iren Horkayne-Szakaly, Leyan Xu, Olga Pletnikova, Francesco Leri, Charles Eberhart, Juan C Troncoso, and Vassilis E Koliatsos. The problem of axonal injury in the brains of veterans with histories of blast exposure. *Acta neuropathologica communications*, 2(1):153, 2014. ISSN 2051-5960.

[13] D. H. Smith, M. Nonaka, R. Miller, M. Leoni, X. H. Chen, D. Alsop, and D. F. Meaney. Immediate coma following inertial brain injury dependent on axonal damage in the brainstem. *Journal of Neurosurgery*, 93(2):315–322, 2000. ISSN 0022-3085. URL <GotoISI>://000088414500020.

BIBLIOGRAPHY

[14] DVBIC. Defense and veterans brain injury center: Dod worldwide numbers for tbi. *http://dvbic.dcoe.mil/dod-worldwide-numbers-tbi*, 2018.

[15] JL Gerbeding and S Binder. Report to congress on mild traumatic brain injury in the united states: steps to preventing a serious public health problem. *Atlanta (GA): Centers for Disease Control and Prevention*, 2003.

[16] Dhananjay R Namjoshi, Craig Good, Wai Hang Cheng, William Panenka, Darrin Richards, Peter A Cripton, and Cheryl L Wellington. Towards clinical management of traumatic brain injury: a review of models and mechanisms from a biomechanical perspective. *Disease models & mechanisms*, 6(6):1325–1338, 2013. ISSN 1754-8403.

[17] Ulrika Krave, Mohamed Al-Olama, and Hans-Arne Hansson. Rotational acceleration closed head flexion trauma generates more extensive diffuse brain injury than extension trauma. *Journal of neurotrauma*, 28(1):57–70, 2011. ISSN 0897-7151.

[18] Hamish A Kerr, Christine M Curtis, Lyle J Micheli, Mininder S Kocher, David Zurakowski, John HM Brooks, and Simon PT Kemp. Collegiate rugby union injury patterns in new england: a prospective cohort study. *British journal of sports medicine*, 2008. ISSN 0306-3674.

[19] S. J. Hollis, M. R. Stevenson, A. S. McIntosh, E. A. Shores, M. W. Collins, and C. B. Taylor. Incidence, risk, and protective factors of mild traumatic brain

injury in a cohort of australian nonprofessional male rugby players. *American Journal of Sports Medicine*, 37(12):2328–2333, 2009. ISSN 0363-5465. doi: Doi10.1177/0363546509341032. URL <GotoISI>://000272180500005.

[20] Parisa Saboori and Ali Sadegh. Brain subarachnoid space architecture: histological approach. In *ASME 2011 International Mechanical Engineering Congress and Exposition*, pages 89–94. American Society of Mechanical Engineers.

[21] Mohamad Zoghi-Moghadam and Ali M Sadegh. Global/local head models to analyse cerebral blood vessel rupture leading to asdh and sah. *Computer Methods in Biomechanics and Biomedical Engineering*, 12(1):1–12, 2009. ISSN 1025-5842.

[22] S. A. Kruse, G. H. Rose, K. J. Glaser, A. Manduca, J. P. Felmlee, C. R. Jack, and R. L. Ehman. Magnetic resonance elastography of the brain. *Neuroimage*, 39(1):231–237, 2008. ISSN 1053-8119. doi: 10.1016/j.neuroimage.2007.08.030. URL <GotoISI>://WOS:000251406000021.

[23] Graham Teasdale and Bryan Jennett. Assessment of coma and impaired consciousness: a practical scale. *The Lancet*, 304(7872):81–84, 1974. ISSN 0140-6736.

[24] James P Kelly, John S Nichols, Christopher M Filley, Kevin O Lillehei, David Rubinstein, and BK Kleinschmidt-DeMasters. Concussion in sports: guidelines

for the prevention of catastrophic outcome. *Jama*, 266(20):2867–2869, 1991. ISSN 0098-7484.

[25] Quality Standards Subcommittee of the American Academy of Neurology. Practice parameter: The management of concussion in sports (summary statement). *Neurology*, 48:581–585, 1997.

[26] T. Kay, D.E. Harrington, R. Adams, T. Anderson, S. Berrol, K. Cicerone, C. Dahlberg, D. Gerber, R. Goka, and P. et al. Harley. Definition of mild traumatic brain injury. *J Head Trauma Rehabilitation*, 8:74–85, 1993.

[27] Andrew R Mayer, Davin K Quinn, and Christina L Master. The spectrum of mild traumatic brain injury a review. *Neurology*, 89(6):623–632, 2017. ISSN 0028-3878.

[28] Mark Aubry, Robert Cantu, Jiri Dvorak, Toni Graf-Baumann, Karen Johnston, James Kelly, Mark Lovell, Paul McCrory, Willem Meeuwisse, and Patrick Schamasch. Summary and agreement statement of the first international conference on concussion in sport, vienna 2001. *The Physician and sportsmedicine*, 30(2):57–63, 2002. ISSN 0091-3847.

[29] Paul McCrory, Willem H Meeuwisse, Mark Aubry, Bob Cantu, Jiří Dvořák, Ruben J Echemendia, Lars Engebretsen, Karen Johnston, Jeffrey S Kutcher, and Martin Raftery. Consensus statement on concussion in sport: the 4th

international conference on concussion in sport held in zurich, november 2012. *Br J Sports Med*, 47(5):250–258, 2013. ISSN 0306-3674.

[30] Shawn Marshall, Mark Bayley, Scott McCullagh, Diana Velikonja, and Lindsay Berrigan. Clinical practice guidelines for mild traumatic brain injury and persistent symptoms. *Canadian Family Physician*, 58(3):257–267, 2012. ISSN 0008-350X.

[31] Kimberly G Harmon, Jonathan A Drezner, Matthew Gammons, Kevin M Guskiewicz, Mark Halstead, Stanley A Herring, Jeffrey S Kutcher, Andrea Pana, Margot Putukian, and William O Roberts. American medical society for sports medicine position statement: concussion in sport. *Br J Sports Med*, 47(1):15–26, 2013. ISSN 0306-3674.

[32] Kristen Dams-O'Connor, Lisa Spielman, Ayushi Singh, Wayne A Gordon, Hester F Lingsma, Andrew IR Maas, Geoffrey T Manley, Pratik Mukherjee, David O Okonkwo, and Ava M Puccio. The impact of previous traumatic brain injury on health and functioning: a track-tbi study. *Journal of neurotrauma*, 30(24):2014–2020, 2013. ISSN 0897-7151.

[33] Raquel C Gardner and Kristine Yaffe. Epidemiology of mild traumatic brain injury and neurodegenerative disease. *Molecular and Cellular Neuroscience*, 66: 75–80, 2015. ISSN 1044-7431.

[34] Walter F Stewart, Namhee Kim, Chloe S Ifrah, Richard B Lipton, Tamar A

Bachrach, Molly E Zimmerman, Mimi Kim, and Michael L Lipton. Symptoms from repeated intentional and unintentional head impact in soccer players. *Neurology*, pages 901–908, 2017. ISSN 0028-3878.

[35] L. Z. Shuck and S. H. Advani. Rheological response of human brain tissue in shear. *ASME J Basic Eng*, 94:905–911, 1972.

[36] G. T. Fallenstein, V. D. Hulce, and J. W. Melvin. Dynamic mechanical properties of human brain tissue. *J. Biomechanics*, 2(3):217–226, 1969.

[37] Lynne E Bilston, Zizhen Liu, and Nhan Phan-Thien. Linear viscoelastic properties of bovine brain tissue in shear. *Biorheology*, 34(6):377–385, 1997. ISSN 0006-355X.

[38] Kristy B Arbogast and Susan S Margulies. Regional differences in mechanical properties of the porcine central nervous system. Report 0148-7191, SAE Technical Paper, 1997.

[39] GWM Peters, JH Meulman, and AAHJ Sauren. The applicability of the time/temperature superposition principle to brain tissue. *Biorheology*, 34(2): 127–138, 1997. ISSN 0006-355X.

[40] K. B. Arbogast and S. S. Margulies. Material characterization of the brainstem from oscillatory shear tests. *Journal of Biomechanics*, 31(9):801–807, 1998. ISSN 0021-9290.

[41] Kirk L Thibault and Susan S Margulies. Age-dependent material properties of the porcine cerebrum: effect on pediatric inertial head injury criteria. *Journal of biomechanics*, 31(12):1119–1126, 1998. ISSN 0021-9290.

[42] DW A Brands. The large shear strain dynamic behavior of in-vitro porcine brain tissue and a silicone gel model material. Report, SAE Technical Paper, 2000.

[43] L. E. Bilston, Z. Z. Liu, and N. Phan-Thien. Large strain behaviour of brain tissue in shear: Some experimental data and differential constitutive model. *Biorheology*, 38(4):335–345, 2001. ISSN 0006-355X. URL <GotoISI>://000172484600004http://content.iospress.com/download/biorheology/bir113?id=biorheology%2Fbir113.

[44] KK Darvish and JR Crandall. Nonlinear viscoelastic effects in oscillatory shear deformation of brain tissue. *Medical engineering & physics*, 23(9):633–645, 2001. ISSN 1350-4533.

[45] Samuel A Lippert, Elizabeth M Rang, and Michele J Grimm. The high frequency properties of brain tissue. *Biorheology*, 41(6):681–691, 2004. ISSN 0006-355X.

[46] Stéphane Nicolle, Mourad Lounis, and Rémy Willinger. Shear properties of brain tissue over a frequency range relevant for automotive impact situations: new experimental results. *Stapp Car Crash Journal*, 48:239–258, 2004.

[47] M. Hrapko, J. A. W. van Dommelen, G. W. M. Peters, and J. S. H. M. Wismans. The mechanical behaviour of brain tissue: Large strain response and constitutive modelling. *Biorheology*, 43(5):623–636, 2006. ISSN 0006-355X. URL <GotoISI>://000241646500002.

[48] F. Shen, T. E. Tay, J. Z. Li, S. Nigen, P. V. S. Lee, and H. K. Chan. Modified bilston nonlinear viscoelastic model for finite element head injury studies. *Journal of Biomechanical Engineering-Transactions of the Asme*, 128:797–801, 2006.

[49] A Garo, M Hrapko, JAW Van Dommelen, and GWM Peters. Towards a reliable characterisation of the mechanical behaviour of brain tissue: the effects of post-mortem time and sample preparation. *Biorheology*, 44(1):51–58, 2007. ISSN 0006-355X.

[50] Amit Gefen and Susan S Margulies. Are in vivo and in situ brain tissues mechanically similar? *Journal of biomechanics*, 37(9):1339–1352, 2004. ISSN 0021-9290.

[51] Farhana Pervin and Weinong W Chen. Dynamic mechanical response of bovine gray matter and white matter brain tissues under compression. *Journal of biomechanics*, 42(6):731–735, 2009. ISSN 0021-9290.

[52] Amit Gefen, Nurit Gefen, Qiliang Zhu, Ramesh Raghupathi, and Susan S Mar-

gulies. Age-dependent changes in material properties of the brain and braincase of the rat. *Journal of neurotrauma*, 20(11):1163–1177, 2003. ISSN 0897-7151.

[53] MCH Dodgson. Colloidal structure of brain. *Biorheology*, 1(1):21–30, 1962. ISSN 0006-355X.

[54] J. E. Galford and J. H. McElhaney. A viscoelastic study of scalp, brain, and dura. *J. Biomechanics*, 3(2):211–221, 1970.

[55] James B Koeneman. *Viscoelastic properties of brain tissue*. Thesis, 1966.

[56] G. Franceschini, D. Bigoni, P. Regitnig, and Gerhard A. Holzapfel. Brain tissue deforms similarly to filled elastomers and follows consolidation theory. *Journal of the Mechanics and Physics of Solids*, 54(12):2592–2620, 2006.

[57] M. T. Prange and S. S. Margulies. Regional, directional, and age-dependent properties of the brain undergoing large deformation. *Journal of Biomechanical Engineering-Transactions of the Asme*, 124(2):244–252, 2002. ISSN 0148-0731. doi: Doi10.1115/1.1449907. URL <GotoISI>://000175343800013.

[58] Michael A Green, Lynne E Bilston, and Ralph Sinkus. In vivo brain viscoelastic properties measured by magnetic resonance elastography. *NMR in Biomedicine: An International Journal Devoted to the Development and Application of Magnetic Resonance In vivo*, 21(7):755–764, 2008. ISSN 0952-3480.

[59] EH Clayton, JR Garbow, and PV Bayly. Frequency-dependent viscoelastic

parameters of mouse brain tissue estimated by mr elastography. *Physics in Medicine & Biology*, 56(8):2391, 2011. ISSN 0031-9155.

[60] Y Feng, EH Clayton, Y Chang, RJ Okamoto, and PV Bayly. Viscoelastic properties of the ferret brain measured in vivo at multiple frequencies by magnetic resonance elastography. *Journal of biomechanics*, 46(5):863–870, 2013. ISSN 0021-9290.

[61] S. Nicolle, M. Lounis, R. Willinger, and J. F. Palierne. Shear linear behavior of brain tissue over a large frequency range. *Biorheology*, 42(3):209–223, 2005. ISSN 0006-355X. URL <GotoISI>://WOS:000229750300002.

[62] Stefan M Atay, Christopher D Kroenke, Arash Sabet, and Philip V Bayly. Measurement of the dynamic shear modulus of mouse brain tissue in vivo by magnetic resonance elastography. *Journal of biomechanical engineering*, 130(2): 021013, 2008. ISSN 0148-0731.

[63] Jonathan Vappou, Elodie Breton, Philippe Choquet, Rémy Willinger, and André Constantinesco. Assessment of in vivo and post-mortem mechanical behavior of brain tissue using magnetic resonance elastography. *Journal of biomechanics*, 41(14):2954–2959, 2008. ISSN 0021-9290.

[64] Benjamin S Elkin, Ashok Ilankovan, and Barclay Morrison. Age-dependent regional mechanical properties of the rat hippocampus and cortex. *Journal of biomechanical engineering*, 132(1):011010, 2010. ISSN 0148-0731.

[65] Ingolf Sack, Bernd Beierbach, Jens Wuerfel, Dieter Klatt, Uwe Hamhaber, Sebastian Papazoglou, Peter Martus, and JÃ$\frac{1}{4}$rgen Braun. The impact of aging and gender on brain viscoelasticity. *Neuroimage*, 46(3):652–657, 2009. ISSN 1053-8119.

[66] M. Hrapko, J. A. W. van Dommelen, G. W. M. Peters, and J. S. H. M. Wismans. The influence of test conditions on characterization of the mechanical properties of brain tissue. *Journal of Biomechanical Engineering-Transactions of the Asme*, 130(3):663–676, 2008. ISSN 0148-0731. doi: 10.1115/1.2907746. URL <GotoISI>://000255880700003.

[67] M. S. Estes and J. H. McElhaney. Response of brain tissue of compressive loading. In *The Fourth ASME Biomechanics Conference*, 1970.

[68] BR Donnelly and J Medige. Shear properties of human brain tissue. *Journal of biomechanical engineering*, 119(4):423, 1997. ISSN 0148-0731.

[69] K. Miller and K. Chinzei. Constitutive modelling of brain tissue: experiment and theory. *J. Biomechanics*, 30:1115–1121, 1997.

[70] K. Miller and K. Chinzei. Mechanical properties of brain tissue in tension. *Journal of Biomechanics*, 35:483–490, 2002.

[71] Atsutaka TAMURA, Sadayuki HAYASHI, Isao WATANABE, Kazuaki NAGAYAMA, and Takeo MATSUMOTO. Mechanical characterization of brain

tissue in high-rate compression. *Journal of Biomechanical Science and Engineering*, 2(3):115–126, 2007. ISSN 1880-9863.

[72] Atsutaka TAMURA, Sadayuki HAYASHI, Kazuaki NAGAYAMA, and Takeo MATSUMOTO. Mechanical characterization of brain tissue in high-rate extension. *Journal of Biomechanical Science and Engineering*, 3(2):263–274, 2008. ISSN 1880-9863.

[73] MT Begonia, R Prabhu, J Liao, MF Horstemeyer, and LN Williams. The influence of strain rate dependency on the structure-property relations of porcine brain. *Annals of biomedical engineering*, 38(10):3043–3057, 2010. ISSN 0090-6964.

[74] Badar Rashid, Michel Destrade, and Michael D Gilchrist. Mechanical characterization of brain tissue in compression at dynamic strain rates. *Journal of the Mechanical Behavior of Biomedical Materials*, (10):23–38, 2012. ISSN 1751-6161.

[75] Jiangyue Zhang, Narayan Yoganandan, Frank A Pintar, Yabo Guan, Barry Shender, Glenn Paskoff, and Purushottam Laud. Effects of tissue preservation temperature on high strain-rate material properties of brain. *Journal of Biomechanics*, 44(3):391–396, 2011. ISSN 0021-9290.

[76] Hideyuki Kimpara and Masami Iwamoto. Mild traumatic brain injury pre-

dictors based on angular accelerations during impacts. *Annals of biomedical engineering*, 40(1):114–126, 2012. ISSN 0090-6964.

[77] L. Y. Zhang, K. H. Yang, and A. I. King. Comparison of brain responses between frontal and lateral impacts by finite element modeling. *Journal of Neurotrauma*, 18(1):21–30, 2001. ISSN 0897-7151.

[78] J. C. Roberts, T. P. Harrigan, E. E. Ward, T. M. Taylor, M. S. Annett, and A. C. Merkle. Human head-neck computational model for assessing blast injury. *Journal of Biomechanics*, 45(16):2899–2906, 2012. ISSN 0021-9290. doi: 10.1016/j.jbiomech.2012.07.027.

[79] S. Chatelin, C. Deck, F. Renard, S. Kremer, C. Heinrich, J. P. Armspach, and R. Willinger. Computation of axonal elongation in head trauma finite element simulation. *Journal of the Mechanical Behavior of Biomedical Materials*, 4(8):1905–1919, 2011. ISSN 1751-6161. doi: 10.1016/j.jmbbm.2011.06.007.

[80] Stelios K Kyriacou, Christos Davatzikos, S James Zinreich, and R Nick Bryan. Nonlinear elastic registration of brain images with tumor pathology using a biomechanical model [mri]. *IEEE transactions on medical imaging*, 18(7):580–592, 1999. ISSN 0278-0062.

[81] Badar Rashid, Michel Destrade, and Michael D Gilchrist. Mechanical characterization of brain tissue in simple shear at dynamic strain rates. *Journal of the mechanical behavior of biomedical materials*, 28:71–85, 2013. ISSN 1751-6161.

[82] L Angela Mihai, LiKang Chin, Paul A Janmey, and Alain Goriely. A comparison of hyperelastic constitutive models applicable to brain and fat tissues. *Journal of The Royal Society Interface*, 12(110):20150486, 2015. ISSN 1742-5689.

[83] Kaveh Laksari, Mehdi Shafieian, and Kurosh Darvish. Constitutive model for brain tissue under finite compression. *Journal of biomechanics*, 45(4):642–646, 2012. ISSN 0021-9290.

[84] S. Budday, G. Sommer, C. Birkl, C. Langkammer, J. Haybaeck, J. Kohnert, M. Bauer, F. Paulsen, P. Steinmann, E. Kuhl, and G. A. Holzapfel. Mechanical characterization of human brain tissue. *Acta Biomaterialia*, 48:319–340, 2017. ISSN 1742-7061. doi: 10.1016/j.actbio.2016.10.036. URL <GotoISI>://WOS:000393247000027.

[85] Y. Feng, R. J. Okamoto, R. Namani, G. M. Genin, and P. V. Bayly. Measurements of mechanical anisotropy in brain tissue and implications for transversely isotropic material models of white matter. *Journal of the Mechanical Behavior of Biomedical Materials*, 23:117–132, 2013. ISSN 1751-6161. doi: 10.1016/j.jmbbm.2013.04.007.

[86] E Diguet, E Van Houten, M Green, and R Sinkus. High resolution mr-elastography mouse brain study: towards a mechanical atlas. In *Proc Intl Soc Mag reson Med*, volume 17.

[87] Silvia Budday, Charles Raybaud, and Ellen Kuhl. A mechanical model predicts

morphological abnormalities in the developing human brain. *Scientific reports*, 4:5644, 2014. ISSN 2045-2322.

[88] David B MacManus, Baptiste Pierrat, Jeremiah G Murphy, and Michael D Gilchrist. Mechanical characterization of the p56 mouse brain under large-deformation dynamic indentation. *Scientific reports*, 6:srep21569, 2016. ISSN 2045-2322.

[89] KK Mendis, RL Stalnaker, and SH Advani. A constitutive relationship for large deformation finite element modeling of brain tissue. *Journal of Biomechanical Engineering*, 117(3):279–285, 1995. ISSN 0148-0731.

[90] Badar Rashid, Michel Destrade, and Michael D Gilchrist. Mechanical characterization of brain tissue in tension at dynamic strain rates. *Journal of the mechanical behavior of biomedical materials*, 33:43–54, 2014. ISSN 1751-6161.

[91] T Kaster, I Sack, and A Samani. Measurement of the hyperelastic properties of ex vivo brain tissue slices. *Journal of biomechanics*, 44(6):1158–1163, 2011. ISSN 0021-9290.

[92] R. M. Wright and K. T. Ramesh. An axonal strain injury criterion for traumatic brain injury. *Biomechanics and Modeling in Mechanobiology*, 11(1-2):245–260, 2012. ISSN 1617-7959. doi: 10.1007/s10237-011-0307-1.

[93] X. Ning, Q. Zhu, Y. Lanir, and S.S. Margulies. A transversely isotropic viscoelastic constitutive equation for brainstem undergoing finite deformation.

Journal of Biomechanical Engineering-Transactions of the Asme, 128:925–933, 2006.

[94] Chiara Giordano and Svein Kleiven. Evaluation of axonal strain as a predictor for mild traumatic brain injuries using finite element modeling. *Stapp car crash journal*, 58:29, 2014. ISSN 1532-8546.

[95] Chiara Giordano and Svein Kleiven. Connecting fractional anisotropy from medical images with mechanical anisotropy of a hyperviscoelastic fibre-reinforced constitutive model for brain tissue. *Journal of The Royal Society Interface*, 11(91):20130914, 2014. ISSN 1742-5689.

[96] N. C. Colgan, M. D. Gilchrist, and K. M. Curran. Applying dti white matter orientations to finite element head models to examine diffuse tbi under high rotational accelerations. *Progress in Biophysics & Molecular Biology*, 103(2-3): 304–309, 2010. ISSN 0079-6107. doi: 10.1016/j.pbiomolbio.2010.09.008.

[97] Kristy B Arbogast and Susan S Margulies. A fiber-reinforced composite model of the viscoelastic behavior of the brainstem in shear. *Journal of biomechanics*, 32(8):865–870, 1999. ISSN 0021-9290.

[98] D. F. Meaney. Relationship between structural modeling and hypelastic material behavior: application to cns white matter. *Biomech Model Mechanobiol*, 1: 279–293, 2003.

[99] Shaokoon Cheng and Lynne E Bilston. Unconfined compression of white matter. *Journal of biomechanics*, 40(1):117–124, 2007. ISSN 0021-9290.

[100] Peter J Basser. Interstitial pressure, volume, and flow during infusion into brain tissue. *Microvascular research*, 44(2):143–165, 1992. ISSN 0026-2862.

[101] Martin G Tauber, Hassan Khayam-Bashi, and Merle A Sande. Effects of ampicillin and corticosteroids on brain water content, cerebrospinal fluid pressure, and cerebrospinal fluid lactate levels in experimental pneumococcal meningitis. *Journal of Infectious Diseases*, 151(3):528–534, 1985. ISSN 1537-6613.

[102] H.R. Lissner, M. Lebow, and F.G. Evans. Experimental studies on the relation between acceleration and intracranial pressure changes in man. *Surg Gynecol Obstet*, 111:329–38, 1960.

[103] Charles W Gadd. Use of a weighted-impulse criterion for estimating injury hazard. Report 0148-7191, SAE Technical Paper, 1966.

[104] D. Marjoux, D. Baumgartner, C. Deck, and R. Willinger. Head injury prediction capability of the hic, hip, simon and ulp criteria. *Accident Analysis and Prevention*, 40(3):1135–1148, 2008. ISSN 0001-4575. doi: Doi10.1016/J.Aap.2007.12.006. URL <GotoISI>://000256782000033.

[105] J. Versace. A review of the severity index. *15th Stapp Car Crash Conference Proceedings*, SAE 710881, 1971.

[106] James A Newman. A generalized acceleration model for brain injury threshold (gambit). In *Proceedings of International IRCOBI Conference, 1986.*

[107] F Kramer and H Appel. Evaluation of protection criteria on the basis of statistical biomechanics. In *International IRCOBI Conference on the Biomechanics of Impacts, 1990, Bron, France.*

[108] F. Feist, J. Gugler, C. Arregui-Dalmases, E. del Pozo de Dios, F. Lopez-Valdes, D. Deck, and R. Willinger. Pedestrian collisions with flat-fronted vehicles: injury patterns and importance of rotational accelerators as a predictor for traumatic brain injury (tbi). In *21st International Conference on the Enhanced Safety of Vehicles (ESV)*, volume 09-0264, pages 1–19.

[109] James Newman, Cameron Barr, Marc C Beusenberg, Ed Fournier, Nicholas Shewchenko, Eric Welbourne, and C Withnall. A new biomechanical assessment of mild traumatic brain injury. part 2: results and conclusions. In *Proceedings of the International Research Council on the Biomechanics of Injury conference*, volume 28. International Research Council on Biomechanics of Injury, .

[110] JA Newman, Marc Beusenberg, Edmund Fournier, Nicholas Shewchenko, Christopher Withnall, Albert King, King Yang, Liying Zhang, James McElhaney, and Lawrence Thibault. A new biomechanical assessment of mild traumatic brain injury: Part 1 - methodology. In *Proceedings of the International*

Research Conference on the Biomechanics of Impacts (IRCOBI), pages 17–36, .

[111] Erik G Takhounts, Matthew J Craig, Kevin Moorhouse, Joe McFadden, and Vikas Hasija. Development of brain injury criteria (bric). Report, SAE Technical Paper, 2013.

[112] Robert WG Anderson, CJ Brown, PC Blumbergs, G Scott, JW Finney, NR Jones, and AJ McLean. Mechanisms of axonal injury: an experimental and numerical study of a sheep model of head impact. In *Proceedings, International Conference on the Biomechanics of Impact IRCOBI, Sitges, Spain*, pages 107–120.

[113] J. F. Yao, J. K. Yang, and D. Otte. Investigation of head injuries by reconstructions of real-world vehicle-versus-adult-pedestrian accidents. *Safety Science*, 46 (7):1103–1114, 2008. ISSN 0925-7535. doi: Doi10.1016/J.Ssci.2007.06.021. URL <GotoISI>://000257971600007.

[114] C. Ward, M. Chang, and A. Nahum. Intracranial pressure - a brain injury criterion. *26th Stapp Car Crash Conference Proceedings*, SAE 801304, 1980.

[115] C. Deck and R. Willinger. Improved head injury criteria based on head fe model. *International Journal of Crashworthiness*, 13(6):667–678, 2008. ISSN 1358-8265. doi: Doi10.1080/13588260802411523. URL <GotoISI>://000261414900008.

[116] E.G. Takhounts, R.H. Eppinger, J.Q. Campbell, R.E. Tannous, E.D. Power, and L.S. Shook. On the development of the simon finite element head model. *Stapp Car Crash Journal*, 47:107–133, 2003.

[117] Albert I King, King H Yang, Liying Zhang, Warren Hardy, Bioengineering Center, and David C Viano. Is head injury caused by linear or angular acceleration? *IRCOBI Conference - Lisbon (Portugal)*, 2003.

[118] David C Viano and PER Lovsund. Biomechanics of brain and spinal-cord injury: analysis of neuropathologic and neurophysiology experiments. *Traffic Injury Prevention*, 1(1):35–43, 1999. ISSN 1028-6586.

[119] L. Y. Zhang, K. H. Yang, and A. I. King. A proposed injury threshold for introduction mild traumatic brain injury. *Journal of Biomechanical Engineering-Transactions of the Asme*, 126(2):226–236, 2004. ISSN 0148-0731. doi: 10.1115/1.1691446. URL <GotoISI>://WOS:000221349700012.

[120] S. Kleiven. Predictors for traumatic brain injuries evaluated through accident reconstructions. *51st Stapp Car Crash Journal*, pages 81–114, 2007.

[121] Xavier Trosseille, C Tarriere, F Lavaste, F Guillon, and A Domont. Development of a fem of the human head according to a specific test protocol. Report 0148-7191, SAE Technical Paper, 1992.

[122] David I Shreiber, Allison C Bain, Douglas T Ross, Douglas H Smith, TA Gennarelli, Tracy K McIntosh, and David F Meaney. Experimental in-

vestigation of cerebral contusion: Histopathological and immunohistochemicc evaluation of dynamic cortical deformation. *Journal of Neuropathology & Experimental Neurology*, 58(2):153–164, 1999. ISSN 1554-6578.

[123] S. S. Margulies and L. E. Thibault. A proposed tolerance criterion for diffuse axonal injury in man. *Journal of Biomechanics*, 25(8):917–923, 1992. ISSN 0021-9290. URL <GotoISI>://A1992JD39100010.

[124] John Thomas Weber, BA Rzigalinski, KA Willoughby, SF Moore, and EF Ellis. Alterations in calcium-mediated signal transduction after traumatic injury of cortical neurons. *Cell calcium*, 26(6):289–299, 1999. ISSN 0143-4160.

[125] D. M. Geddes and R. S. Cargill. An in vitro model of neural trauma: Device characterization and calcium response to mechanical stretch. *Journal of Biomechanical Engineering-Transactions of the Asme*, 123(3):247–255, 2001. ISSN 0148-0731. URL <GotoISI>://000169878700007.

[126] B.S. Elkin and B. Morrison III. Region-specific tolerance criteria for the living brain. *Stapp Car Crash Journal*, 51:127–38, 2007.

[127] B. Morrison III, H.L. Cater, C.C.-B. Wang, F.C. Thomas, C.T. Hung, G.A. Ateshian, and L.E. Sundstrom. A tissue level tolerance criterion for living brain developed with an in vitro model of traumatic mechanical loading. *Stapp Car Crash Journal*, 47:93–105, 2003.

[128] A. C. Bain and D. F. Meaney. Tissue-level thresholds for axonal damage in an experimental model of central nervous system white matter injury. *Journal of Biomechanical Engineering-Transactions of the Asme*, 122:615–622, 2000.

[129] J. A. B. Gray and J. M. Ritchie. Effects of stretch on single myelinated nerve fibres. *Journal of Physiology-London*, 124(1):84–99, 1954. ISSN 0022-3751. URL <GotoISI>://A1954UH83500008.

[130] K.E. Saatman. *An isolated single myelinated nerve fiber model for the mechanics of axonal injury*. Thesis, 1993.

[131] Atsutaka Tamura, Kazuaki Nagayama, Takeo Matsumoto, and Sadayuki Hayashi. Variation in nerve fiber strain in brain tissue subjected to uniaxial stretch. Report, SAE Technical Paper, 2007.

[132] D. K. Cullen and M. C. LaPlaca. Neuronal response to high rate shear deformation depends on heterogeneity of the local strain field. *Journal of Neurotrauma*, 23(9):1304–1319, 2006. ISSN 0897-7151. doi: 10.1089/neu.2006.23.1304. URL <GotoISI>://WOS:000240605900003.

[133] C. Zhou, T.B. Khalil, and A. I. King. Shear stress distribution in the porcine brain due to rotational impact. *38th Stapp Car Crash Conference Proceedings*, SAE 942314(1697-1707), 1994.

[134] Svein Kleiven and Hans von Holst. Consequences of head size following trauma

to the human head. *Journal of Biomechanics*, 35(2):153–160, 2002. ISSN 0021-9290.

[135] T. El Sayed, A. Mota, F. Fraternali, and M. Ortiz. Biomechanics of traumatic brain injury. *Comput. Methods Appl. Mech. Engrg.*, 197:4692–4701, 2008.

[136] P. A. Taylor and C. C. Ford. Simulation of blast-induced early-time intracranial wave physics leading to traumatic brain injury. *Journal of Biomechanical Engineering-Transactions of the Asme*, 131(6):–, 2009. ISSN 0148-0731. doi: Doi10.1115/1.3118765.

[137] Y. Lanir. Constitutive-equations for fibrous connective tissues. *Journal of Biomechanics*, 16(1):1–12, 1983. ISSN 0021-9290.

[138] T. A. Shugar and M. G. Katona. Development of finite-element head-injury model. *Journal of the Engineering Mechanics Division-Asce*, 101(3):223–239, 1975. ISSN 0044-7951.

[139] Carley Conrad Ward and Robert B Thompson. The development of a detailed finite element brain model. Report 0148-7191, SAE Technical Paper, 1975.

[140] Jesse S Ruan, Tawfik B Khalil, and Albert I King. Finite element modeling of direct head impact. Report 0148-7191, SAE Technical Paper, 1993.

[141] A. J. M. Spencer. *Deformations of fibre-reinforced materials*. Clarendon Press, Oxford, 1972.

[142] Gerhard A. Holzapfel. *Nonlinear solid mechanics : a continuum approach for engineering*. Wiley, Chichester ; New York, 2000. ISBN 047182304X (acid-free paper) 0471823198 (acid-free paper).

[143] JG Murphy. Transversely isotropic biological, soft tissue must be modelled using both anisotropic invariants. *European Journal of Mechanics-A/Solids*, 42:90–96, 2013. ISSN 0997-7538.

[144] M Destrade, B Mac Donald, JG Murphy, and G Saccomandi. At least three invariants are necessary to model the mechanical response of incompressible, transversely isotropic materials. *Computational Mechanics*, 52(4):959–969, 2013. ISSN 0178-7675.

[145] RJH Cloots, JAW Van Dommelen, Tobias Nyberg, Svein Kleiven, and MGD Geers. Micromechanics of diffuse axonal injury: influence of axonal orientation and anisotropy. *Biomechanics and modeling in mechanobiology*, 10(3):413–422, 2011. ISSN 1617-7959.

[146] S. Ganpule, N. P. Daphalapurkar, K. T. Ramesh, A. K. Knutsen, D. L. Pham, P. V. Bayly, and J. L. Prince. A three-dimensional computational human head model that captures live human brain dynamics. *Journal of Neurotrauma*, 34 (13):2154–2166, 2017. ISSN 0897-7151. doi: 10.1089/neu.2016.4744.

[147] S. Doll and K. Schweizerhof. On the development of volumetric strain energy functions. *Journal of Applied Mechanics-Transactions of the Asme*, 67(1):17–

21, 2000. ISSN 0021-8936. doi: 10.1115/1.321146. URL <GotoISI>://WOS:000087541900003.

[148] D. Watanabe, K. Yuge, T. Nishimoto, S. Murakami, and H. Takao. Development of a human head fe model and impact simulation on the focal brain injury. *Journal of Computational Science and Technology*, 3(1):252–263, 2009.

[149] Silvia Budday, Richard Nay, Rijk de Rooij, Paul Steinmann, Thomas Wyrobek, Timothy C Ovaert, and Ellen Kuhl. Mechanical properties of gray and white matter brain tissue by indentation. *Journal of the mechanical behavior of biomedical materials*, 46:318–330, 2015. ISSN 1751-6161.

[150] Cort J Willmott, Scott M Robeson, and Kenji Matsuura. A refined index of model performance. *International Journal of Climatology*, 32(13):2088–2094, 2012. ISSN 1097-0088.

[151] David R Legates and Gregory J McCabe. Evaluating the use of "goodness-of-fit" measures in hydrologic and hydroclimatic model validation. *Water resources research*, 35(1):233–241, 1999. ISSN 1944-7973.

[152] Daniel N Moriasi, Jeffrey G Arnold, Michael W Van Liew, Ronald L Bingner, R Daren Harmel, and Tamie L Veith. Model evaluation guidelines for systematic quantification of accuracy in watershed simulations. *Transactions of the ASABE*, 50(3):885–900, 2007.

[153] H. Kimpara, Y. Nakahira, M. Iwamoto, K. Miki, K. Ichihara, S. Kawano, and T. Taguchi. Investigation of anteroposterior head-neck responses during severe frontal impacts using a brain-spinal cord complex fe model. *Stapp Car Crash Journal*, 50:509–544, 2006.

[154] D. H. Smith and D. F. Meaney. Axonal damage in traumatic brain injury. *Neuroscientist*, 6(6):483–495, 2000. ISSN 1073-8584.

[155] E. A. Montgomery, G. W. Fenton, R. J. McClelland, G. Macflynn, and W. H. Rutherford. The psychobiology of minor head-injury. *Psychological Medicine*, 21(2):375–384, 1991. ISSN 0033-2917. doi: 10.1017/s0033291700020481. URL <GotoISI>://WOS:A1991FR87300013.

[156] L. Delano-Wood, K. J. Bangen, S. F. Sorg, A. L. Clark, D. M. Schiehser, N. Luc, M. W. Bondi, M. Werhane, R. T. Kim, and E. D. Bigler. Brainstem white matter integrity is related to loss of consciousness and postconcussive symptomatology in veterans with chronic mild to moderate traumatic brain injury. *Brain Imaging and Behavior*, 9(3):500–512, 2015. ISSN 1931-7557. doi: 10.1007/s11682-015-9432-2. URL <GotoISI>://WOS:000361604300011.

[157] Ronald Richard Hosey. *A HOMEOMORPHIC FINITE-ELEMENT MODEL OF IMPACT HEAD INJURY*. Dissertation, 1982.

[158] F. Dimasi, J. Marcus, and Rolf H. Eppinger. 3-d (three-dimensional) anatomic brain model for relating cortical strains to automobile crash loading. *Proceed-*

ings: International Technical Conference on the Enhanced Safety of Vehicles, 1993:916–924, 1993. URL http://dx.doi.org/.

[159] Ho-Sung Kang, Rémy Willinger, Baye M Diaw, and Bryan Chinn. Validation of a 3d anatomic human head model and replication of head impact in motorcycle accident by finite element modeling. Report 0148-7191, SAE Technical Paper, 1997.

[160] Erik G Takhounts, Rolf H Eppinger, J Quinn Campbell, and Rabih E Tannous. On the development of the simon finite element head model. *Stapp car crash journal*, 47:107, 2003. ISSN 1532-8546.

[161] Liying Zhang, King H Yang, Ramesh Dwarampudi, Kiyoshi Omori, Tieliang Li, Kun Chang, Warren N Hardy, Tom B Khalil, and Albert I King. Recent advances in brain injury research: a new human head model development and validation. *Stapp Car Crash J*, 45(11):369–394, 2001.

[162] Kiyoshi Omori, Liying Zhang, King H Yang, and Albert I King. Effect of cerebral vasculatures on the mechanical response of brain tissue: a preliminary study. *ASME APPLIED MECHANICS DIVISION-PUBLICATIONS-AMD*, 246:167–174, 2000.

[163] Yednesh Parnaik, Philippe Beillas, Constantine K. Demetropoulos, Warren N. Hardy, King H. Yang, and Albert I. King. The influence of surrogate blood vessels on the impact response of a physical model of the brain. *Stapp car*

crash journal, 48:259–77, 2004. ISSN 1532-8546. URL <GotoISI>://MEDLINE:17230270.

[164] Liying Zhang, Jinho Bae, Warren N. Hardy, Kenneth L. Monson, Geoffrey T. Manley, Werner Goldsmith, King H. Yang, and Albert I. King. Computational study of the contribution of the vasculature on the dynamic response of the brain. *Stapp car crash journal*, 46:145–64, 2002. ISSN 1532-8546. URL <GotoISI>://MEDLINE:17096223.

[165] Johnson Ho and Svein Kleiven. Dynamic response of the brain with vasculature: A three-dimensional computational study. *Journal of Biomechanics*, 40(13): 3006–3012, 2007. ISSN 0021-9290. doi: 10.1016/j.jbiomech.2007.02.011. URL <GotoISI>://WOS:000250277800023.

[166] Svein Kleiven. Evaluation of head injury criteria using a finite element model validated against experiments on localized brain motion, intracerebral acceleration, and intracranial pressure. *International Journal of Crashworthiness*, 11 (1):65–79, 2006. ISSN 1358-8265.

[167] N. J. Tustison, B. B. Avants, P. A. Cook, Y. Zheng, A. Egan, P. A. Yushkevich, and J. C. Gee. N4itk: Improved n3 bias correction. *IEEE Transactions on Medical Imaging*, 29(6):1310–1320, June 2010.

[168] Snehashis Roy, John A. Butman, and Dzung L. Pham. Robust skull stripping

using multiple MR image contrasts insensitive to pathology. *NeuroImage*, 146: 132 – 147, 2017.

[169] Brian B. Avants, Nicholas J. Tustison, Gang Song, Philip A. Cook, Arno Klein, and James C. Gee. A reproducible evaluation of ANTs similarity metric performance in brain image registration. *NeuroImage*, 54(3):2033 – 2044, 2011.

[170] H. Wang, J. W. Suh, S. R. Das, J. B. Pluta, C. Craige, and P. A. Yushkevich. Multi-atlas segmentation with joint label fusion. *IEEE Transactions on Pattern Analysis and Machine Intelligence*, 35(3):611–623, March 2013.

[171] Yuankai Huo, Andrew J. Plassard, Aaron Carass, Susan M. Resnick, Dzung L. Pham, Jerry L. Prince, and Bennett A. Landman. Consistent cortical reconstruction and multi-atlas brain segmentation. *NeuroImage*, 138:197 – 210, 2016.

[172] Jeffrey Glaister, Aaron Carass, Dzung L. Pham, John A. Butman, and Jerry L. Prince. Falx cerebri segmentation via multi-atlas boundary fusion. In Maxime Descoteaux, Lena Maier-Hein, Alfred Franz, Pierre Jannin, D. Louis Collins, and Simon Duchesne, editors, *Medical Image Computing and Computer Assisted Intervention - MICCAI 2017*, pages 92–99, 2017.

[173] Jeffrey Glaister, Aaron Carass, Dzung L. Pham, John A Butman, and Jerry L. Prince. Automatic falx cerebri and tentorium cerebelli segmentation from magnetic resonance images. volume 10137, pages 10137 – 10137 – 7, 2017.

[174] O. Commowick and S. K. Warfield. A continuous STAPLE for scalar, vector, and tensor images: An application to DTI analysis. *IEEE Transactions on Medical Imaging*, 28(6):838–846, June 2009.

[175] M. Sabry Hassouna, A.A. Farag, Stephen Hushek, and Thomas Moriarty. Cerebrovascular segmentation from TOF using stochastic models. *Medical Image Analysis*, 10(1):2 – 18, 2006.

[176] Francis H Harlow. The particle-in-cell computing method for fluid dynamics. *Methods Comput. Phys.*, 3:319–343, 1964.

[177] Deborah Sulsky, Shi-Jian Zhou, and Howard L Schreyer. Application of a particle-in-cell method to solid mechanics. *Computer physics communications*, 87(1-2):236–252, 1995. ISSN 0010-4655.

[178] D Sulsky and HL Schreyer. Axisymmetric form of the material point method with applications to upsetting and taylor impact problems. *Computer methods in applied mechanics and engineering*, 139(1-4):409–429, 1996. ISSN 0045-7825.

[179] Deborah Sulsky, Zhen Chen, and Howard L Schreyer. A particle method for history-dependent materials. *Computer methods in applied mechanics and engineering*, 118(1-2):179–196, 1994. ISSN 0045-7825.

[180] SG Bardenhagen and EM Kober. The generalized interpolation material point method. *Computer Modeling in Engineering and Sciences*, 5(6):477–496, 2004. ISSN 1526-1492.

[181] A. Sadeghirad, R. M. Brannon, and J. Burghardt. A convected particle domain interpolation technique to extend applicability of the material point method for problems involving massive deformations. *International Journal for Numerical Methods in Engineering*, 86(12):1435–1456, 2011. ISSN 0029-5981. doi: 10.1002/nme.3110. URL <GotoISI>://WOS:000290582500004.

[182] S. Ganpule, N. Daphalapurkar, and K.T. Ramesh. Shear wave propagation in soft materials with application to modeling traumatic brain injury. In *Proceedings of the 17th U.S. National Congress on Theoretical and Applied Mechanics*, 2014.

[183] Irina Ionescu, James E Guilkey, Martin Berzins, Robert M Kirby, and Jeffrey A Weiss. Simulation of soft tissue failure using the material point method. *Journal of Biomechanical Engineering*, 128(6):917–924, 2006. ISSN 0148-0731.

[184] S. Ganpule, N. P. Daphalapurkar, K. T. Ramesh, A. K. Knutsen, D. L. Pham, P. V. Bayly, and J. L. Prince. A three-dimensional computational human head model that captures live human brain dynamics. *Journal of Neurotrauma*, 34 (13):2154–2166, 2017. ISSN 0897-7151. doi: 10.1089/neu.2016.4744. URL <GotoISI>://WOS:000404530400454.

[185] K. Hayashi, H. Handa, S. Nagasawa, A. Okumura, and K. Moritake. Stiffness and elastic behavior of human intra-cranical and extra-cranial arter-

ies. *Journal of Biomechanics*, 13(2):175–179, 1980. ISSN 0021-9290. doi: 10.1016/0021-9290(80)90191-8. URL <GotoISI>://WOS:A1980JK74600012.

[186] Ying Chen and Martin Ostoja-Starzewski. MRI-based finite element modeling of head trauma: spherically focusing shear waves. *Acta Mechanica*, 213(1-2): 155–167, 2010. ISSN 0001-5970.

[187] R. Willinger, H. S. Kang, and B. Diaw. Three-dimensional human head finite-element model validation against two experimental impacts. *Annals of Biomedical Engineering*, 27:403–410, 1999.

[188] Logan E Miller, Jillian E Urban, and Joel D Stitzel. Development and validation of an atlas-based finite element brain model. *Biomechanics and modeling in mechanobiology*, 15(5):1201–1214, 2016. ISSN 1617-7959.

[189] Robert H Cole and Royal Weller. Underwater explosions. *Physics Today*, 1:35, 1948. ISSN 0031-9228.

[190] SJ Lee, MA King, J Sun, HK Xie, G Subhash, and M Sarntinoranont. Measurement of viscoelastic properties in multiple anatomical regions of acute rat brain tissue slices. *Journal of the mechanical behavior of biomedical materials*, 29:213–224, 2014. ISSN 1751-6161.

[191] Leon Axel and Lawrence Dougherty. Mr imaging of motion with spatial modulation of magnetization. *Radiology*, 171(3):841–845, 1989. ISSN 0033-8419.

[192] PV Bayly, TS Cohen, EP Leister, D Ajo, EC Leuthardt, and GM Genin. Deformation of the human brain induced by mild acceleration. *Journal of neurotrauma*, 22(8):845–856, 2005. ISSN 0897-7151.

[193] Nael F Osman, Elliot R McVeigh, and Jerry L Prince. Imaging heart motion using harmonic phase mri. *IEEE transactions on medical imaging*, 19(3):186–202, 2000. ISSN 0278-0062.

[194] Songbai Ji, Wei Zhao, James C Ford, Jonathan G Beckwith, Richard P Bolander, Richard M Greenwald, Laura A Flashman, Keith D Paulsen, and Thomas W McAllister. Group-wise evaluation and comparison of white matter fiber strain and maximum principal strain in sports-related concussion. *Journal of Neurotrauma*, 32(7):441, 2015.

[195] W Zhao, JC Ford, LA Flashman, TW McAllister, and S Ji. White matter injury susceptibility via fiber strain evaluation using whole-brain tractography. *Journal of neurotrauma*, 33(20):1834, 2016. ISSN 1557-9042.

[196] Sarah Sullivan, Stephanie A Eucker, David Gabrieli, Connor Bradfield, Brittany Coats, Matthew R Maltese, Jongho Lee, Colin Smith, and Susan S Margulies. White matter tract-oriented deformation predicts traumatic axonal brain injury and reveals rotational direction-specific vulnerabilities. *Biomechanics and modeling in mechanobiology*, 14(4):877–896, 2015. ISSN 1617-7959.

[197] Anastasia Yendiki, Patricia Panneck, Priti Srinivasan, Allison Stevens, Lilla

Zöllei, Jean Augustinack, Ruopeng Wang, David Salat, Stefan Ehrlich, and Tim Behrens. Automated probabilistic reconstruction of white-matter pathways in health and disease using an atlas of the underlying anatomy. *Frontiers in neuroinformatics*, 5:23, 2011. ISSN 1662-5196.

[198] Ann C McKee, Thor D Stein, Patrick T Kiernan, and Victor E Alvarez. The neuropathology of chronic traumatic encephalopathy. *Brain pathology*, 25(3): 350–364, 2015. ISSN 1015-6305.

[199] Mazdak Ghajari, Peter J Hellyer, and David J Sharp. Computational modelling of traumatic brain injury predicts the location of chronic traumatic encephalopathy pathology. *Brain*, 140(2):333–343, 2017. ISSN 0006-8950.

[200] Svein Kleiven. Influence of impact direction on the human head in prediction of subdural hematoma. *Journal of neurotrauma*, 20(4):365–379, 2003. ISSN 0897-7151.

[201] Erik G Takhounts, Stephen A Ridella, Vikas Hasija, Rabih E Tannous, J Quinn Campbell, Dan Malone, Kerry Danelson, Joel Stitzel, Steve Rowson, and Stefan Duma. Investigation of traumatic brain injuries using the next generation of simulated injury monitor (simon) finite element head model. Report, SAE Technical Paper, 2008.

[202] Elena Gutierrez, Yinglai Huang, Kenneth Haglid, Feng Bao, Hans-Arne Hansson, Anders Hamberger, and David Viano. A new model for diffuse brain injury

by rotational acceleration: I. model, gross appearance, and astrocytosis. *Journal of neurotrauma*, 18(3):247–257, 2001. ISSN 0897-7151.

[203] M. Runnerstam, F. Bao, Y. L. Huang, J. S. Shi, E. Gutierrez, A. Hamberger, H. A. Hansson, D. Viano, and K. Haglid. A new model for diffuse brain injury by rotational acceleration: Ii. effects on extracellular glutamate, intracranial pressure, and neuronal apoptosis. *Journal of Neurotrauma*, 18(3):259–273, 2001. ISSN 0897-7151. doi: 10.1089/08977150151070892. URL <GotoISI>://WOS:000167653000004.

[204] Kevin D Browne, Xiao-Han Chen, David F Meaney, and Douglas H Smith. Mild traumatic brain injury and diffuse axonal injury in swine. *Journal of neurotrauma*, 28(9):1747–1755, 2011. ISSN 0897-7151.

[205] Thomas A Gennarelli, Lawrence E Thibault, J Hume Adams, David I Graham, Carson J Thompson, and Robert P Marcincin. Diffuse axonal injury and traumatic coma in the primate. *Annals of Neurology: Official Journal of the American Neurological Association and the Child Neurology Society*, 12(6): 564–574, 1982. ISSN 0364-5134.

[206] LJ Lawson, VH Perry, P Dri, and S Gordon. Heterogeneity in the distribution and morphology of microglia in the normal adult mouse brain. *Neuroscience*, 39(1):151–170, 1990. ISSN 0306-4522.

[207] BS Elkin, EU Azeloglu, KD Costa, and B Morrison 3rd. Mechanical heterogene-

ity of the rat hippocampus measured by atomic force microscope indentation. *Journal of neurotrauma*, 24(5):812, 2007. ISSN 0897-7151.

[208] J. D. Finan, S. N. Sundaresh, B. S. Elkin, G. M. McKhann, and B. Morrison. Regional mechanical properties of human brain tissue for computational models of traumatic brain injury. *Acta Biomaterialia*, 55:333–339, 2017. ISSN 1742-7061. doi: 10.1016/j.actbio.2017.03.037. URL <GotoISI>://WOS:000403414500025.

[209] EJ Grossman, Y Ge, JH Jensen, JS Babb, L Miles, J Reaume, JM Silver, RI Grossman, and M Inglese. Thalamus and cognitive impairment in mild traumatic brain injury: a diffusional kurtosis imaging study. *Journal of neurotrauma*, 29(13):2318–2327, 2012. ISSN 0897-7151.

[210] RR Hicks, DH Smith, DH Lowenstein, R SAINT MARIE, and TK McIntosh. Mild experimental brain injury in the rat induces cognitive deficits associated with regional neuronal loss in the hippocampus. *Journal of neurotrauma*, 10 (4):405–414, 1993. ISSN 0897-7151.

[211] Nadia Gosselin, Carolina Bottari, Jen-Kai Chen, Michael Petrides, Simon Tinawi, Elaine de Guise, and Alain Ptito. Electrophysiology and functional mri in post-acute mild traumatic brain injury. *Journal of neurotrauma*, 28(3): 329–341, 2011. ISSN 0897-7151.

[212] Benjamin S Elkin, Ashok I Ilankovan, and Barclay Morrison III. A detailed

viscoelastic characterization of the p17 and adult rat brain. *Journal of neurotrauma*, 28(11):2235–2244, 2011. ISSN 0897-7151.

[213] Benjamin S Elkin, Ashok Ilankova, and Barclay Morrison. Dynamic, regional mechanical properties of the porcine brain: indentation in the coronal plane. *Journal of biomechanical engineering*, 133(7):071009, 2011. ISSN 0148-0731.

[214] Fuqian Chen, Jun Zhou, Yan Li, Yongbo Wang, Lihong Li, and Hongzhi Yue. Mechanical properties of porcine brain tissue in the coronal plane: interregional variations of the corona radiata. *Annals of biomedical engineering*, 43(12):2903–2910, 2015. ISSN 0090-6964.

[215] K. L. Monson, W. Goldsmith, N. M. Barbaro, and G. T. Manley. Significance of source and size in the mechanical response of human cerebral blood vessels. *Journal of Biomechanics*, 38(4):737–744, 2005. ISSN 0021-9290. doi: 10.1016/j.jbiomech.2004.05.004. URL <GotoISI>://WOS:000227590400011.

[216] K. L. Monson, N. M. Barbaro, and G. T. Manley. Biaxial response of passive human cerebral arteries. *Annals of Biomedical Engineering*, 36(12):2028–2041, 2008. ISSN 0090-6964. doi: 10.1007/s10439-008-9578-9. URL <GotoISI>://WOS:000260937200009.

[217] V. C. Mow, S. C. Kuei, W. M. Lai, and C. G. Armstrong. Biphasic creep and stress-relaxation of articular-cartilage in compression - theory and experiments.

Journal of Biomechanical Engineering-Transactions of the Asme, 102(1):73–84, 1980. ISSN 0148-0731. URL <GotoISI>://WOS:A1980JE19600011.

[218] R. L. Spilker and J. K. Suh. Formulation and evaluation of a finite-element model for the biphasic model of hydrated soft-tissues. *Computers & Structures*, 35(4):425–439, 1990. ISSN 0045-7949. doi: 10.1016/0045-7949(90)90067-c. URL <GotoISI>://WOS:A1990DE77600015.

[219] B. Cohen, W. M. Lai, and V. C. Mow. A transversely isotropic biphasic model for unconfined compression of growth plate and chondroepiphysis. *Journal of Biomechanical Engineering-Transactions of the Asme*, 120(4):491–496, 1998. ISSN 0148-0731. doi: 10.1115/1.2798019. URL <GotoISI>://WOS:000075756700008.

[220] Neil A Martin, Ravish V Patwardhan, Michael J Alexander, Cynthia Zane Africk, Jae Hong Lee, Ehud Shalmon, David A Hovda, and Donald P Becker. Characterization of cerebral hemodynamic phases following severe head trauma: hypoperfusion, hyperemia, and vasospasm. *Journal of neurosurgery*, 87(1):9–19, 1997. ISSN 0022-3085.

[221] Gerrit J Bouma, J Paul Muizelaar, Sung C Choi, Pauline G Newlon, and Harold F Young. Cerebral circulation and metabolism after severe traumatic brain injury: the elusive role of ischemia. *Journal of neurosurgery*, 75(5):685–693, 1991. ISSN 0022-3085.

[222] AC Clevenger, T Kilbaugh, and SS Margulies. Carotid artery blood flow decreases after rapid head rotation in piglets. *Journal of neurotrauma*, 32(2): 120–126, 2015. ISSN 0897-7151.

[223] Riikka Immonen, Taneli Heikkinen, Leena Tähtivaara, Antti Nurmi, Taina-Kaisa Stenius, Jukka Puoliväli, Tinka Tuinstra, Amie L Phinney, Bernard Van Vliet, and Juha Yrjänheikki. Cerebral blood volume alterations in the perilesional areas in the rat brain after traumatic brain injury - comparison with behavioral outcome. *Journal of Cerebral Blood Flow & Metabolism*, 30(7): 1318–1328, 2010. ISSN 0271-678X.

[224] X. M. Chen and M. Sarntinoranont. Biphasic finite element model of solute transport for direct infusion into nervous tissue. *Annals of Biomedical Engineering*, 35(12):2145–2158, 2007. ISSN 0090-6964. doi: 10.1007/s10439-007-9371-1. URL <GotoISI>://WOS:000250976000012.

[225] RE Craine, Albert Edward Green, and Paul Mansour Naghdi. A mixture of viscous elastic materials with different constituent temperatures. Report, CALIFORNIA UNIV BERKELEY DIV OF APPLIED MECHANICS, 1969.

[226] A. E. Green and P. M. Naghdi. The flow of fluid through an elastic solid. *Acta Mechanica*, 9(3):329–340, 1970. ISSN 1619-6937. doi: 10.1007/bf01179830. URL http://dx.doi.org/10.1007/BF01179830.

[227] Amit Srivastava, GL Sivakumar Babu, and Sumanta Haldar. Influence of spa-

tial variability of permeability property on steady state seepage flow and slope stability analysis. *Engineering Geology*, 110(3-4):93–101, 2010. ISSN 0013-7952.

[228] I. I. Bogdanov, V. V. Mourzenko, J. F. Thovert, and PM Adler. Effective permeability of fractured porous media in steady state flow. *Water Resources Research*, 39(1), 2003. ISSN 0043-1397.

[229] AP Selvadurai and A Głowacki. Permeability hysterisis of limestone during isotropic compression. *Ground water*, 46(1):113–119, 2008. ISSN 0017-467X.

[230] Stephen Whitaker. Flow in porous media i: A theoretical derivation of darcy's law. *Transport in porous media*, 1(1):3–25, 1986. ISSN 0169-3913.

[231] Bauer E Sumpio. *Hemodynamic forces and vascular cell biology*. RG Landes, 1993. ISBN 1879702452.

[232] DN Ku and C Zhu. The mechanical environment of the artery. *Hemodynamic forces and vascular cell biology*, pages 1–23, 1993.

[233] Niels A Lassen. Cerebral blood flow and oxygen consumption in man. *Physiological reviews*, 39(2):183–238, 1959. ISSN 0031-9333.

[234] Seymour S Kety and Carl F Schmidt. The effects of altered arterial tensions of carbon dioxide and oxygen on cerebral blood flow and cerebral oxygen consumption of normal young men. *The Journal of clinical investigation*, 27(4): 484–492, 1948. ISSN 0021-9738.

[235] Jordan S Querido and A William Sheel. Regulation of cerebral blood flow during exercise. *Sports medicine*, 37(9):765–782, 2007. ISSN 0112-1642.

Vita

Fatma Madouh was born in Kuwait on December 11^{th}, 1984 to her father Abdullatif Madouh and her mother Eqbal Al-Haidar. In January 2007, she received the degree of Bachelor of Science in Mechanical Engineering from Kuwait University. She then worked as a material engineer in Kuwait Oil Company from May 2007 till August 2011 when she received a scholarship from Kuwait University to continue her graduate studies. She directly enrolled in the Johns Hopkins University Master's Program in the mechanical engineering department and continued her PhD studies in the same school. Her research focuses on understanding the effects of brain heterogeneities on the outcome of mild traumatic brain injury that can not be tested experimentally on humans.